PEOPLE'S DEMOCRATIC REPUBLIC OF ALGERIA

MINISTRY OF HIGHER EDUCATION

AND SCIENTIFIC RESEARCH

University of Echahid Hamma Lakhdar - El Oued

FACULTY OF TECHNOLOGY

DEPARTMENT OF PROCESS ENGINEERING AND PETROCHEMISTRY

Thesis submitted in fulfilment of the requirement for the degree of

Doctorate of Science

in Process Engineering

Specialty: Chemical Engineering

Green synthesis and characterization of iron oxide nanoparticles: evaluation of the reactivity of their surfaces

Presented by

AHMOUDA Kaouthar

Before the jury composed of

REBIAI Abdelkrim	MCA	University of El-Oued	President
SEKIRIFA Mohamed Lamine	Professor	University of Ouargla	Examiner
BELKHALFA Hakim	MRA	CRAPC, Ouargla	Examiner
BEN MYA Omar	Professor	University of El-Oued	Examiner
BENHAOUA Boubaker	Professor	University of El-Oued	Supervisor

2021-2022

PEOPLE'S DEMOCRATIC REPUBLIC OF ALGERIA
MINISTRY OF HIGHER EDUCATION
AND SCIENTIFIC RESEARCH
University of Echahid Hamma Lakhdar - El Oued

FACULTY OF TECHNOLOGY
DEPARTMENT OF PROCESS ENGINEERING AND PETROCHEMISTRY

Thesis submitted in fulfilment of the requirement for the degree of

Doctorate of Science

in Process Engineering

Specialty: Chemical Engineering

Green synthesis and characterization of iron oxide nanoparticles: evaluation of the reactivity of their surfaces

Presented by

AHMOUDA Kaouthar

Before the jury composed of

REBIAI Abdelkrim	MCA	University of El-Oued	President
SEKIRIFA Mohamed Lamine	Professor	University of Ouargla	Examiner
BELKHALFA Hakim	MRA	CRAPC, Ouargla	Examiner
BEN MYA Omar	Professor	University of El-Oued	Examiner
BENHAOUA Boubaker	Professor	University of El-Oued	Supervisor

2021-2022

ABSTRACT

In this thesis, two novel studies are presented, the first one investigated how the Ferrous Reducing Antioxidant Potential (FRAP) of aqueous plant extracts affects Fe^{2+} vacancies (defects) formation within greenly synthesized wüstite (Fe_xO) nanoparticles. In the second study, after the complete oxidation of Fe_xO NPs into Fe_3O_4 NPs under ambient conditions, the influence of mediating plant extract's acidity on magnetite surface reactivity has been studied in the preferential and enhanced adsorption of methyl green (MG) on the different greenly synthesized Fe_3O_4 surfaces by coupling three processes: MG adsorption in ambient dark conditions at the first process, at the second process, the thermocatalysis of MG/Fe_3O_4 residual solution, and finally the photocatalysis by UV irradiation of MG/Fe_3O_4 residual solution after applying thermocatalysis. This study used four aqueous plant extracts as reducing agents with $FeCl_3$ as a precursor to synthesize Fe_xO NPs. The plants dealt with in this study are Rosemarinus Officinalis.(L), Juniperus Phoenicia.(L), Matricaria Pubescens.(L), and Artemisia Herba-alba.(L), and their acidic extracts pH are respectively; 5.25, 5.05, 4.63, and 3.69. All synthesized samples are characterized by XRD, SEM, ATR-FTIR, and UV-Vis. For Fe_xO, lattice parameters are calculated through XRD data, and then wüstite compositions are calculated using the McCammon equation. Results of the first study showed that the FRAP has a clear effect on Fe^{2+} vacancies formation within wüstite NPs. Indeed, The increase in the FRAP leads to a decrease in Fe^{2+} defects within wüstite NPs and consequently an increase in the grain size. Furthermore, studying iron vacancies' effect on wüstite formation thermodynamic showed that free energy of wüstite formation $\Delta G^0_{fF_eO}(x)$ is impacted by cation vacancies and hence by FRAP. The novelty of the second study lies in highlighting the influence of the mediating plant extract on magnetite physicochemical characteristics which impact the preferential and enhanced MG adsorption. Studied characteristics are: hydroxyl groups functionality on magnetite surfaces, grain size, and band gap energy. It was found that plant extract acidity has a clear effect on studied physicochemical characteristics of magnetite samples. The analysis of FTIR spectra showed that hydroxyl groups densities differ on the four magnetite samples. Furthermore, the calculated grain sizes of magnetite samples based on XRD spectra data vary from 29.27 to 41.49 nm. The analysis of UV-Vis spectra of the four magnetite samples showed that estimated direct band gap energies vary from 2.87 to 2.97 eV. Found results showed that the decrease of mediating plant extract's acidity leads to an increase in functional hydroxyl groups density on magnetite surfaces which conducted to an increase in MG adsorption capacity and yield in the first process. Thus MG adsorption was more preferred on magnetite surfaces mediated by low acidic plant extracts. Furthermore, the increase of plant extract acidity leads to a decrease in particle size and an increase in band gap energy and therefore to the slowness of electron/hole pairs recombination lifetime upon electrons excitation. So, magnetite greenly synthesized from more acidic mediating plant extract showed more thermo- and photocatalytic activities in MG adsorption. MG adsorption under thermo- and photocatalysis processes were more enhanced on magnetite NPs exhibiting slower electron/hole pairs recombination lifetime.

RÉSUMÉ

L'effet des extraits des plantes sur la stoechiométrie du fer et la réactivité de surface des nanoparticules d'oxydes de fer synthétisées par la méthode verte font l'objet de deux contributions présentées dans la présente thèse. La première contribution consiste à étudier l'effet du FRAP (Ferrous Reducing Antioxidant Potential) de l'extrait aqueux de plante sur la formation des défauts cationiques de Fe^{2+} dedans les nanoparticules du wustite (Fe_xO). Alors que dans la deuxième contribution investigue l'influence de l'acidité de l'extrait de plante utilisé dans la synthèse verte sur la réactivité de surface de la magnétite dans l'adsorption préférentielle et améliorée du vert de méthyle (VM) sur les différentes surfaces de magnétites dans trois phases d'adsorption : l'adsorption de VM dans les conditions ambiantes et sombres dans la première phase. En deuxième phase, la thermocatalyse de la solution résiduelle après la première phase (VM/Fe_3O_4), et enfin la photocatalyse par l'irradiation UV de la solution résiduelle (VM/Fe_3O_4) après l'application de la thermocatalyse. Dans cette étude quatre extraits aqueux de plantes ont été utilisés comme agents réducteurs avec $FeCl_3$ comme précurseur pour synthétiser les nanoparticules de Fe_xO. Les quatre plantes utilisées sont Rosemarinus Officinalis.(L), Juniperus Phoenicia.(L), Matricaria Pubescens.(L), et Artemisia Herba-alba.(L), et les pH de leurs extraits sont acidiques ayant respectivement les valeurs: 5.25, 5.05, 4.63 et 3.69. Les quatre échantillons de magnétite (Fe_3O_4) de la deuxième étude résultent de l'oxydation complète de Fe_xO en Fe_3O_4 dans les conditions ambiantes. Tous les échantillons des nanoparticules des oxydes de fer synthétisés sont caractérisés par DRX, MEB, RTA-IRTF et UV-Vis. Pour les nanoparticules de FexO, les paramètres de réseau ont été calculés à partir des données DRX. La stœchiométrie de fer dans les nanoparticules du FexO a été ensuite calculée par l'équation de McCammon. Les résultats de la première étude ont montré que le FRAP a un effet clair sur la formation de défauts de Fe^{2+} dans le wustite. En effet, l'augmentation du FRAP mène à la diminution des défauts de Fe^{2+} et par conséquent à une augmentation de la taille des grains des nanoparticules. En outre, l'étude de l'effet des défauts de Fe^{2+} sur la thermodynamique de la formation du wustite a montré que l'énergie libre de la formation du wustite ($\Delta G^0_{fF_eO}(x)$) est impactée par les défauts cationiques de Fe^{2+} et par conséquent par le FRAP. La nouveauté de la deuxième étude réside dans l'investigation de l'influence de l'acidité de l'extrait de plante utilisé dans la synthèse verte de nanoparticules de la magnétite sur ses caractéristiques physico-chimiques qui impactent l'adsorption préférentielle et améliorée du VM. Les caractéristiques étudiées sont : la densité du groupe fonctionnel de l'hydroxyle sur la surface de magnétite, la taille des grains, et l'énergie de la bande interdite. Les résultats montrent que l'acidité des extraits des plantes a un effet clair sur les caractéristiques physico-chimiques étudiées de quatre échantillons de magnétite. L'analyse des spectres RTA-IRTF a montré que les densités de groupes hydroxyle diffèrent sur les surfaces de quatre échantillons de magnétite. En plus, les tailles des grains des échantillons de magnétites calculées à partir des données DRX varient de 29,27 à 41,49 nm. L'analyse de spectres UV-Vis des quatre échantillons de magnétite a montré que la bande interdite directe estimée varie de 2,87 à 2,97 eV. Les résultats obtenus ont montré que la diminution de l'acidité de l'extrait mène à une augmentation de la densité des groupes fonctionnels de l'hydroxyle sur les surfaces de magnétite, ce qui a conduit à une augmentation de la capacité d'adsorption de VM et du rendement dans la première phase d'adsorption. De plus, l'adsorption du VM était plus préférée sur les surfaces de magnétite synthétisées à partir des extraits de plantes peu acidiques. En outre, l'augmentation de l'acidité des extraits des plantes mène à une diminution de la taille des nanoparticules et à une augmentation de l'énergie de la bande interdite directe et par conséquent au ralentissement de la durée de vie de la recombinaison des paires électron/trou pendant l'excitation des électrons. Par ailleurs, les nanoparticules de magnétite synthétisées en utilisant des extraits des plantes plus acidiques ont montré plus des activités thermo- et photocatalytiques dans l'adsorption de VM. L'adsorption de VM sous thermo- et photocatalyse était plus améliorée sur les nanoparticules de magnétite présentant des durées de vie de recombinaison des paires électron/trou plus lente. Cependant, sous photocatalyse, l'amélioration de l'adsorption de VM est encore plus importante par rapport à la thermocatalyse.

مُلخّص

في هاته الاطروحة تمّ تقديم دراستين جديدتين، الأولى بحثت في كيفية تأثير قوة مضادّات الأكسدة في إرجاع كاتيونات الحديد الثلاثية على الفراغات الكاتيونّية Fe^{2+} (العيوب) المتشكّلة داخل جزيئات الوستيت النّانوية (Fe_xO) المصنّعة بطريقة التوليف الأخضر. في الدراسة الثانية، بعد أكسدة الوستيت كليا وتحوّله إلى جزيئات الماغنيتيت (Fe_3O_4) النّانوية في الشروط الطبيعية، تمّت دراسة تأثير حمضيّة المستخلص النباتي المائي المستخدم في التوليف الأخضر لجزيئات الماغنيتيت على فاعلية سطوح عيّنات الماغنيتيت في الامتزاز التفضيلي والمُحسّن للمُلّون أخضر المثيل خلال ثلاثة أطوار متتالية: في الطور الأوّل امتزاز أخضر المثيل في الشروط الطبيعية في الظلام، في الطور الثاني، التحفيز الحراري في الظلام لمحلول أخضر المثيل/Fe_3O_4 المتبقّي، وأخيرا في الطور الثالث، التحفيز الضوئي بواسطة الأشعة فوق البنفسجية لمحلول أخضر المثيل/Fe_3O_4 المتبقّي بعد التحفيز بالحرارة. أُستخدم في هاته الدراسة أربعة مستخلصات نباتية مائية وملح كلور الحديد الثلاثي في التوليف الأخضر لجزيئات الوستيت. النباتات التي تمّ استخدامها في هاته الدراسة هي: العرعر، القريطفة، الإكليل، والشيح، قوة حمضية (pH) هاته المستخلصات النباتية هي على التوالي؛ 3.69، 4.63، 5.05، و5.25. تم توصيف جميع العيّنات المصنّعة بـ انعراج الأشعة السنية (XRD)، المجهر الإلكتروني الماسح، الأشعة تحت الحمراء، والأشعة فوق البنفسجية. بالنسبة إلى عيّنات Fe_xO، تمّ حساب الثوابت الشبكية من خلال معطيات أطياف الأشعة السينية، ثم تمّ حساب ستوكيومترية كاتيونات الحديد الثنائي في تركيبة الوستيت باستخدام معادلةMcCammon . أظهرت نتائج الدراسة الأولى أن ال FRAP له تأثير واضح على تشكل العيوب والفراغات داخل جزيئات الوستيت النانوية. حيث، تؤدّي الزيادة في ال FRAP إلى انخفاض عيوب الحديد الثنائي داخل جزئيات الوستيت وبالتالي زيادة قطر الحبيبات. علاوة على ذلك، أظهرت دراسة تأثير العيوب على الديناميكا الحرارية لتشكّل الوستيت أن الطاقة الحرّة $\Delta G^0_{fF_eO}(x)$ لتشكل الوستيت تأثّرت بهذه العيوب ومن ثم بـ FRAP. تكمن حداثة الدراسة الثانية في تسليط الضوء على تأثير المستخلصات النباتية الوسيطة في التوليف الأخضر لمختلف عيّنات الماغنيتيت على خصائصه الفيزيائية والكيميائية التي تؤثّر على الامتزاز التفضيلي والمُحسّن لأخضر المثيل. الخصائص المدروسة هي: وظائف مجموعات الهيدروكسيل على أسطح الماغنيتيت، قطر الحبيبات النّانوية، وطاقة فجوة النطاق .وُجد أنّ حموضة المستخلصات النباتية لها تأثير واضح على الخصائص الفيزيائية والكيميائية المدروسة لعيّنات الماغنيتيت .أظهر تحليل أطياف الاشعة تحت الحمراء أن كثافة مجموعات الهيدروكسيل تختلف في عيّنات الماغنيتيت الأربع. علاوة على ذلك، يختلف قطر حبيبات عيّنات الماغنيتيت المحسوبة بناءً على معطيات أطياف الاشعة السينية من 29.27 إلى 41.49 نانومتر. أظهر تحليل أطياف الاشعة فوق البنفسجية لعيّنات الماغنيتيت الأربع أنّ طاقات فجوة النطاق المباشر المقدرة تتراوح من 2.87 إلى 2.97 إلكترون فولت. أظهرت النتائج التي تمّ الوصول إليها أنّ انخفاض حموضة المستخلصات النباتية الوسيطة في التوليف الأخضر يُؤدّي إلى زيادة كثافة مجموعات الهيدروكسيل الوظيفية على أسطح الماغنيتيت مما أدّى إلى زيادة سعة امتزاز ومردود أخضر المثيل في الطور الأوّل. وبالتالي كان امتزاز أخضر المثيل أكثر تفضّيلاً على أسطح الماغنيتيت المصنّع بوساطة مستخلصات نباتية ضعيفة الحمضية. علاوة على ذلك، تؤدّي زيادة حموضة المستخلصات النباتية إلى انخفاض قطر الحبيبات النّانوية وزيادة طاقة فجوة النطاق وبالتّالي إلى بطء زمن إعادة تركيب الأزواج الإلكترون / الفجوة عند إثارة

الإلكترونات .لذلك، أظهر الماغنيتيت الذي تمّ تصنيعه من مستخلص نباتي أكثر حمضّية مزيدًا من الفاعلية الحرارية والضوئية في امتزاز أخضر المثيل.

ACKNOWLEDGEMENTS

I would like to thank my doctoral advisor Pr. Boubaker Benhaoua for supporting me during the long of this thesis. His scientific advice and knowledge and many insightful discussions and suggestions have enriched this thesis.

I would like to thank Dr. Abdelkrim Rebiai for accepting to be the president of my committee. I would like to thank my committee members Pr. Mohamed Lamine Sekirifa, Dr. BelKhalfa Hakim, and Pr. Omar Ben Mya for being my committee members even at hardship.

The person I would like to thank deeply is my husband Dr. Mounir Beggas. He was my all strength that pushed me to accomplish this work and he supported me during the long of this work, thank you Mounir.

I would like to thank my kids who supported me during the long of this work, thank you, my lovers. I would like to thank my Father Nadjib and my Mother Mabrouka for their unconditional support, thank you. I would also like to thank my Stepfather Mohammed and my Stepmother Messaouda for their unconditional support, thank you.

I would especially like to thank my brothers and sisters, and my brothers-in-law and my sister-in-law for their unconditional support during the long of this thesis.

Table of Contents

List of Figures

List of Tables

General Introduction

Iron oxide NPs exist under several forms such as Fe (II) oxide (wüstite Fe_xO), Fe (II, III) oxide (magnetite, Fe_3O_4), Fe (III) oxide (hematite, $\alpha{-}Fe_2O_3$ and maghemite, $\gamma{-}Fe_2O_3$) [1], [2].

Fe_3O_4 and $\gamma{-}Fe_2O_3$ are ferrimagnetic, and both crystallize in the inverse spinel cubic structure. At ambient conditions, these phases are thermodynamically less stable [1]. In contrast, $\alpha{-}Fe_2O_3$ crystallizes in the corundum structure and is thermodynamically the most stable phase of Fe_2O_3. It is weakly ferromagnetic at room temperature and it is antiferromagnetic below 263 K. At an elevated temperature of $> 950\ K$, which is its Curie temperature, $\alpha{-}Fe_2O_3$ shows paramagnetic behavior [3]. Magnetite differs from most other iron oxides in that it consists both divalent (Fe^{II}) and trivalent (Fe^{III}) iron cations. Its formula is written as $Fe^{II}[Fe^{II}Fe_2^{III}]O_4$. Magnetite is frequently non-stoichiometric. It has a Fe^{III} cation deficient sublattice; $Fe^{II}/Fe^{III} \neq 0.5$ (in stoichiometric magnetite ($Fe^{II}/Fe^{III} = 0.5$) [1].

Unlike other iron oxides, stoichiometric wüstite NPs, FeO, cannot exist as a stable phase at low pressures or at pressures exceeding 10 MPas [4]. The nonstoichiometric wüstite is denoted Fe_xO where x represents iron composition and $1{-}x$ represents Fe^{2+} vacancies (defects). It always contains more oxygen than that in the stoichiometric wüstite ($O/Fe > 1$). The nonstoichiometric is accommodated by oxidation of proportion of iron cations and formation of cation vacancies.

Iron oxide NPs are used in several applications such as the heavy crude oil cracking process [5], catalysts for efficient biodiesel production [6], in lithium ion batteries [7], and the treatment of various environmental contaminants [8], [9]. They showed high efficiency for the treatment of various environmental contaminants such as heavy metals [10], pesticides [11], antibiotic [12], [13], nitrate [14], arsenic (III) [15], and dyes [16].

Dyes are produced in a huge amount and their wide-ranging application areas generate a large volume of colored wastewater and different types of post-production waste. The textile industry is an important source of dyes in water environments; during different dyeing processes, dye wastage is at least 5% and can reach 50%, depending on the type of fabric and dye. As a result, almost 200 billion liters of colored effluents are generated annually [17]. Moreover, some of the synthetic organic dyes are slow or nonbiodegradable which makes wastewater more difficult to clean up by commercially available methods [18]. For this purpose, iron oxide NPs are widely used in the purification of wastewater [19]–[22]. They allow a rapid thermodynamic equilibrium between pollutant and adsorbate during the adsorption process and selective removal of pollutants [16], [23], [24].

In this thesis, two novel studies are presented. The first one investigated how the Ferrous Reducing Antioxidant Potential (FRAP) of aqueous plant extracts affects Fe^{2+} vacancies formation in greenly synthesized wüstite (Fe_xO) NPs. In the second study, after the complete oxidation of Fe_xO NPs into Fe_3O_4 NPs under ambient conditions, the influence of mediating plant extract's acidity on magnetite surface reactivity in the preferential, in ambient dark conditions, and enhance MG adsorption by thermocatalysis process under heat, in dark conditions, and photocatalysis process under UV irradiation, in ambient conditions has been investigated.

Properties and Applications of Wüstite (Fe_xO) NPs

A stable cation-deficient phase of Fe_xO with iron x ranging from 0.83 to 0.96 exists at 0.1 MPas pressure and temperature greater than 567 $°C$ [25]. This phase disproportionates to Fe metal and Fe_3O_4 when cooled slowly to temperatures lower than $567\ °\ C$. If however Fe_xO is rapidly quenched the nonstoichiometric form can be obtained as a metastable phase at ambient temperature [25]. Wüstite will be oxidized completely to Fe_3O_4 in about 4 months in ambient conditions [26].

The structure of wüstite NPs is a defective form of an ideal NaCl-type lattice where oxygen ions form an fcc lattice and Fe^{2+} cations are located on the interstitial sites [27]. It is known that Fe^{2+} deficiency is attributed to the formation of neutral vacancies on cation sublattices together with Fe^{3+} cations which provide charge compensation with the aim of preserving the total crystal electroneutrality of Fe_xO. Thus some of the Fe^{2+} cations liberate other electrons and become Fe^{3+} cations. This means that for a given value of x (iron composition in Fe_xO), there are $2(1-x)Fe^{3+}$ and $(1-3(1-x))Fe^{2+}$ cations. This iron deficiency leads to the formation of $1-x$ cation vacancies. These vacancies are partly located as Frenkel defects on interstitial tetrahedral sites [28]. The detailed representative structure of Fe_xO is thus [29]: $Fe^{2+}_{1-3(1-x)}Fe^{3+}_{2(1-x)}\square_{1-x}O^{2-}$ where $\square$ represents cation vacancies. The formation of cation vacancies is responsible for charge redistribution and appearance of Fe^{3+} cations in the octahedral and tetrahedral (interstitial) sites [28], [30].

The study of cation vacancies effect on Fe_xO NPs properties makes the subject of extensive experimental studies and theoretical considerations. It is reported that cation vacancies have an effect on wüstite NPs formation reaction thermodynamic [31], [32], structural [33], [34], physical [29], electrical, and optical properties [35]–[38]. Wdowik et al. [39] reported that cation vacancies have an effect on electronic and dynamical properties of FeO. Zhang et al. [40] found that iron defects have a strong effect on the elastic properties of wüstite NPs. Those defects on interstitial tetrahedral sites make physical and chemical properties of wüstite NPs distinguishable [1], [36], [41]. The plant extract used in the green synthesis of iron oxide NPs is one of the parameters that may influence iron oxide morphologies and hence the reactivity of their surfaces [42]. Macarov et al. [43] reported that pH of plant extract affects the stability of magnetite NPs. In [44] authors found that plant extract concentration has an effect on NPs morphology while authors of [45] found that plant type impacts NPs morphology. According to [46]–[50], one can conclude that plant extract type may impact iron composition within wüstite NPs because they used Medicago sativa (alfalfa), Terminalia chebula dry fruit pericarp, Eucalyptus tereticornis, Cymbopogon citratus, and Avicennia marina extracts, respectively, and they found different iron composition in wüstite NPs. Such plant extract effects need more focus on the properties that impact synthesis iron NPs.

Adsorption Process for Dye Removal

Adsorption has been extensively studied as a cost-effective process for removing a wide variety of pollutants from aqueous solutions [12], [13], [51], [52]. The adsorption ability of the iron oxides arises from the intervention of hydroxyl groups during adsorbate dissociation [53]. Surface hydroxyl groups, with amphoteric properties, are the functional groups of iron oxide surfaces and they are their chemically reactive entities that behave as the active sites upon the adsorption process. These hydroxyl groups may be singly, doubly, and triply coordinated to Fe atoms having different reactivity. The overall density of these groups depends on both the crystal structure and the extent of development of the different crystal faces [54].

Dyes Preferential Adsorption on Metal Oxide NPs

The preferential adsorption of dyes on iron oxide NPs has been studied in several works. Saha et al. [16] studied the preferential adsorption of seven different dyes on magnetite NPs. They reported that magnetite surface preferred adsorbing dyes containing higher OH content. Where Xiao et al. [55] studied the preferential adsorption of different cationic and anionic dyes on iron NPs. They reported that iron NPs preferred removing cationic dyes more than anionic dyes. Madrakian et al. [56] studied the preferential adsorption of seven cationic and anionic dyes on magnetite-coated waste tea. They reported that this nanoadsorbent preferred adsorbing cationic dyes more than anionic dyes.

Several factors can influence the adsorption such as solution pH [54], solution ionic strength [57], dye concentration [58], magnetite NPs concentration [16], and hydroxyl groups density on adsorbent surface [59]. The impact of changing plants on greenly synthesized metal oxide NPs reactivity in dyes adsorption was studied in several works. Huang et al. [60] studied the effect of three different tea extracts (green, oolong, and black teas) on the properties of iron oxide NPs surface: their reactivities in the removal of methyl green from aqueous solutions. They reported that the plant extract has an effect on the reactivity of iron oxide NPs surface that 81.2%, 75.6%, and 67.1% of methyl green dye has been removal by iron oxide NPs synthesised using the extracts of green, oolong, and black teas, respectively. Likewise, Xiao et al. [55] studied the removal of six cationic and anionic dyes. They reported that greenly synthesised iron NPs by tea extract showed preferential adsorption of cationic dyes from an aqueous solution. Other authors [61] synthesized metal oxide NPs using the extracts of flowers, bark, and the leaf of Tecoma stans in order to use them in the removal of Congo red (CR) and crystal violet (CV) dyes. They reported that the adsorbent derived from flower extract gave better dyes adsorption efficiency than those derived from other extracts. Furthermore, Islam et al. [62] synthesized magnetite NPs using six plant extracts in order to use them in the removal of methyl orange (MO) and crystal violet (CV) dyes. They reported that plant extract had an effect on magnetite NPs surface reactivity in the adsorption, where magnetite Nps synthesized using tea extract showed the highest performance (MO 92.34%, CV 96.1%).

Dye Adsorption under Photo- and Thermocatalysis Processes

The fact that metal oxide NPs have a high surface area, good light absorption capacity, and more stableness, makes them have renowned photocatalytic and thermocatalytic activities [63], [64]. Several works studied thermo- and photocatalysis of dyes adsorption on nanomaterials, and they reported the high-efficiency thermo- and photocatalytic activities of nanomaterials. Wu et al. [65] studied the thermocatalysis of methylene blue adsorption on magnetite Fe_3O_4@C NPs. They found that the increase of temperature leads to the increase of methylene blue thermodegradation which indicates the high thermocatalytic activity of studied nanomaterial. Other authors [66] studied the thermocatalysis of N719 dye on anatase TiO_2 nanosheets with dominant (*001*) facets and TiO_2 NPs with dominant (*101*) facets. They found that the increase of temperature leads to the increase of N719 dye thermodegradation on both studied nano-adsorbents due to thermocatalytic activities of TiO_2 NPs. Farghali et al. [67] studied the thermocatalysis of methylene blue on multi-walled carbon nanotubes decorated with $CoFe_2O_4$ NPs by increasing temperate. They reported that this nanocomposite showed an efficient thermocatalytic activity.

Furthermore, Ge et al. [68] studied the photocatalysis of methylene blue and methyl orange adsorption on iron oxide anchored to single-wall carbon nanotubes by UV irradiation. They reported that the studied adsorbent showed an efficient photocatalytic activity. Elhadj et al. [69] studied the photocatalysis of Basic Red 46 dye adsorption over ZnO NPs under solar irradiation. They reported that ZnO NPs exhibit a high photocatalytic activity. Moreover, Kumar et al. [70] studied the photodegradation of methylene blue (MB), Congo red (CR), and methylene orange (MO) under sunlight irradiation in the presence of greenly synthesised magnetite mediated by Andean blackberry leaf extract. They reported that the presence of those magnetite NPs accelerated the photodegradation of the three dyes due to their high photocatalytic activity. Whereas, Sirdeshpande et al. [71] studied the photodegradation of malachite green under sunlight irradiation in the presence of greenly synthesized magnetite using leaf extract of Calliandra haematocephala. They reported that the presence of those magnetite NPs increased the photodegradation of malachite green. Other authors [72] compared the photocatalytic activity of several composites of titanium dioxide containing magnetite NPs with different morphologies and structures in the photodegradation of Rhodamine.Be by UV irradiation. They reported that the highest dye photodegradation was observed when both spherical and rod-shaped composite structures based on titanium dioxide containing 1 wt% of magnetite NPs were used as a photocatalyst. Jassal et al. [73] studied the thermo- and photodegradation of malachite green (MG) and Eriochrome Black T (EBT) dyes on greenly synthesised potassium zinc hexacyanoferrate nanocubes. They found that this adsorbent acted as a photocatalyst, not a thermocatalyst.

Several parameters can impact photo- and thermocatalysis processes such as solution pH, adsorbent concentration, dye concentration, solution ionic strength, temperature [73]–[76], dye structure properties [77], [78], adsorbent particle size [79], gap energy, recombination of electron/hole pairs lifetime [80], [81], adsorbent type [82], [83], light source and time of light exposition [82]. Ullah et al. [80] reported that Mn^{2+} dopant in the ZnO NPs decreased the recombination of the electron/hole pairs lifetime which enhanced the photocatalytic activity efficiency for the removal of dyes. Where Rafaie et al. [81] studied the photocatalytic properties of ZnO NPs microstructures decorated with Ag NPs for degradation of methylene blue under UV irradiation. They reported that the presence of Ag NPs played the role of electron sinks and trapped the photogenerated electrons, which slowed the electron-hole pair lifetime. As a result, ZnO-Ag nanostructure exhibited higher photocatalytic activity for the degradation of MB dye.

Contributions

In this thesis, two novel contributions are presented; the first one investigated how variation in FRAP impacts the formation of cation vacancies within greenly synthesized Fe_xO NPs samples was conducted. In the second contribution, the adsorption of MG dye on four greenly synthesized magnetite NPs has been studied to investigate the mediating plant extract's acidity influence on magnetite surface reactivity in the preferential and enhanced MG adsorption by thermocatalysis under heat in dark conditions and photocatalysis under UV irradiation.

Contribution I: Plant Extract FRAP Effect on Cation Vacancies Formation in Greenly Synthesized Wüstite (Fe_xO) NPs

Cation vacancies directly affect wüstite NPs properties and consequently their applications; thus, finding a process that controls cation vacancies in wüstite is still needed. One of the contributions of this thesis is to look for parameters that impact cation vacancies in the case of green synthesis.

The effect of FRAP power of aqueous plant extract on cation vacancies formation (Fe^{2+} defects) within greenly synthesized Fe_xO NPs has been studied. To the best of our knowledge, there is no study in the literature that dealt with this topic. Since FRAP power reduces Fe^{3+} to Fe^{2+}, four plant extracts are used as reducing agents and $FeCl_3$ as a precursor to greenly synthesize four Fe_xO NPs samples, so as to study how variation in FRAP impacts the formation of cation vacancies in Fe_xO samples as a novelty contribution. Furthermore, a deep focus on Fe_xO formation reaction kinetic and the effect of cation vacancies on its thermodynamic are provided. Iron oxide samples are characterized by XRD, SEM, FTIR-ATR, and UV-Vis techniques. The used plants are Artemisia herba-alba (L), Matricaria Pubescens.(L), Juniperus Phoenicia.(L), and Rosemarinus Officinalis.(L) and the synthesized Fe_xO samples from their extracts are respectively denoted in this thesis by $ARM - Fe_xO$, $MAT - Fe_xO$, $JUN - Fe_xO$ and $ROS - Fe_xO$ NPs.

Contribution II: Influence of The Mediating Plant Extract's Acidity on Magnetite NPs Surface Reactivity in The Preferential and Enhanced MG Adsorption by Thermo- and Photocatalysis

In the second contribution, the preferential and enhanced adsorption of MG on four greenly synthesized Fe_3O_4 NPs surfaces has been studied by coupling three processes. The preferential adsorption of MG on the four magnetite surfaces in ambient dark conditions at first time, followed by adsorption enhancement by thermocatalysis of MG/Fe_3O_4 residual solutions in dark conditions at the second process, and finally the adsorption enhancement by photocatalysis under UV irradiation (365 nm) in ambient conditions of MG/Fe_3O_4 residual solutions after applying thermocatalysis. The focus of this study is on the investigation of the influence of mediating plant extract's acidity on greenly synthesised magnetite NPs physicochemical characteristics which impact the preferential and enhanced MG adsorption. The studied physicochemical characteristics are functional hydroxyl groups density on magnetite surfaces, grain size, and band gap energy. The mediating plants in the green synthesis are Artemisia herba-alba.(L), Matricaria Pubescens.(L), Juniperus Phoenicia.(L), and Rosemarinus Officinalis.(L) and synthesized Fe_3O_4 samples from their extracts are respectively denoted in this thesis by $ARM{-}Fe_3O_4$, $MAT{-}Fe_3O_4$, $JUN{-}Fe_3O_4$ and $ROS{-}Fe_3O_4$. Fe_3O_4 NPs samples were characterized by XRD, SEM, FTIR-ATR, and UV-Vis techniques. In preferential MG adsorption, the pseudo-first-order and pseudo-second-order kinetics of the adsorption as well as the intra-particles diffusion mechanism have been analyzed. Under thermocatalysis, activated thermodynamic parameters free energy; ΔG^0, entropy; ΔS^0, enthalpy; ΔH^0, and activation energy; E_a have been analyzed. Under photocatalysis, the pseudo-first-order has also been analyzed. The mediating plants in the green synthesis were: Artemisia herba-alba.(L), Matricaria Pubescens.(L), Juniperus Phoenicia.(L), and Rosemarinus Officinalis.(L) and the synthesized Fe_3O_4 samples from their extracts are respectively denoted in this thesis by $ARM{-}Fe_3O_4$, $MAT{-}Fe_3O_4$, $JUN{-}Fe_3O_4$ and $ROS{-}Fe_3O_4$. Fe_3O_4 NPs samples were characterized by XRD, SEM, FTIR-ATR, and UV-vis techniques. In preferential MG adsorption, the pseudo-first-order and pseudo-second-order kinetics of the adsorption as well as the intra-particles diffusion mechanism have been analyzed.

Thesis Organization

The next chapter provides a background on iron oxide types and properties and presents the state of the art about synthesis methods and applications. Chapter 2 details nanomaterial surface reactivity in dye adsorption and thermo- and photocatalysis processes mechanisms. It presents also the state of the art and on factors that impact dye adsorption preferential and enhancement by thermo- and photocatalysis. In Chapter3, the effect of plant extracts FRAP on the formation of cation vacancies within greenly synthesized Fe_xO samples is investigated. The study of methyl green (MG) dye adsorption on four greenly synthesized magnetite NPs is detailed in Chapter 4 to investigate the influence of the mediating plant extract on magnetite surface reactivity in preferential and enhanced MG adsorption by thermo- and photocatalysis processes. The last chapter is dedicated to the general conclusion.

PART I

Background and State of the Art

Chapter 1

Iron Oxide-Hydroxide Nanoparticle: Structures, Properties, Synthesis Methods, and Applications

1.1 Introduction

Ferrous and ferric iron oxide nanoparticles (NPs) exist in a rich variety of structures. They present seven crystalline phases, the more common are $\alpha{-}Fe_2O_3$ (hematite), $\gamma{-}Fe_2O_3$ (maghemite), Fe_3O_4 (magnetite) and Fe_xO (wüstite); the less commonly found are the $\beta{-}Fe_2O_3$ and $\epsilon{-}Fe_2O_3$ phases and the low-temperature rhombohedrical structure of magnetite.

Iron oxide NPs have been widely investigated by chemists, engineers, and physicists because of their multi-functional properties due to their large surface-to-volume ratio [84]. Related to their activity, selectivity and stability, and low toxicity [85], iron oxide NPs have a big importance in antibacterial catalysis [86], lithium-ion battery [87], information storage industry [88], and environmental remediation [51], [89], [90].

The physical and chemical properties of ferrous oxide NPs have attracted continuous attention for decades years. Wüstite constitutes, for instance, the main part of the oxide scale on iron and iron-based alloys, and plays an important role in the reduction processes of iron ores. The extremely large homogeneity range of this oxide, in turn, results in very high, and consequently complicated, electronic and ionic disorder. The defect and transport properties of wüstite are, then, the object of extensive experimental studies and theoretical consideration [29], [33], [91], [92].

1.2 Iron Oxide and hydroxide NP Structures and Properties

Several types of iron oxide and hydroxide NP compounds are presented in Table 1.1.

The magnetic properties of such iron oxide and hydroxide NPs at room temperature are presented in Table 1.2.

Oxides-hydroxides and hydroxides	Oxides
Goethite $\alpha - FeOOH$	Hematite $\alpha - Fe_2O_3$
Lepidocrocite $\gamma - FeOOH$	Magnetite Fe_3O_4 $Fe^{II}Fe_2^{III}O_4$
Akaganeite $\beta - FeOOH$	Maghemite $\gamma - Fe_2O_3$
Shwertmannite $Fe_16O_16(OH)_y(SO_4)_z.nH_2O$	$\beta - Fe_2O_3$
$\delta - FeOOH$	$\epsilon - Fe_2O_3$
Feroxyhyte $\delta - FeOOH$	Wüstite FeO
High pressure $FeOOH$	
Ferrihydrite $Fe_5HO_8.4H_2O$	
Bernalite $Fe(OH)_3$	
$Fe(OH)_2$	
Green Rusts $Fe_x^{III}Fe_y^{II}(OH)_{3x+2y-2z}(A^-)_z$, $(A)^- = (Cl)^-, 1/2SO_4^2$	

Table 1.1: Iron oxide-hydroxide, hydroxide, and oxide structures [1], [2]

1.2.1 Hematite $\alpha - Fe_2O_3$

Hematite is isostructural with corundum. The unit cell is hexagonal with $a = 0.5034$ and $c = 1.375\ nm$ [94]. There are six formulas per unit cell. For hexagonal symmetry, the Miller indices are $(hkil)$, i may be replaced by a dot or omitted $(h + k = -i)$. Hematite may be also indexed in a rhombohedral system with unit cell $a_{rh} = 0.5427nm$ and $\alpha = 55.3°$ and there are two formulas units per cell. Hematite structure consists of hcp arrays of oxygen ions stacked along the *001* direction, i.e. planes of anions are parallel to the *001* plane (Figure 1.1a). 2 thirds of the sites are occupied with Fe^{III} cations which are arranged regularly with 2 occupied sites being followed with one vacant site in the *001* plane hence forming sixfold rings as presented in (Figure 1.1b) [95].

The arrangement of cations forms pairs of $Fe{-}O_6$ octahedra. Each octahedron shares edges with three neighboring octahedra in the same plane and one face with an octahedron in an adjacent plane as presented in (Figure 1.1c). Face-sharing occurs along the c-axis. This octahedra face-sharing is responsible for the distortion of cation sublattice from ideal packing; Fe atoms in the octahedra that sharing faces are repelled along the direction normal to *001* plane, causing Fe^{III} cations to shift closer to unshared faces. The $O{-}O$ distances along unshared faces of an octahedron are longer $(0,3035\ nm)$ than the distances of the shared faces $(0,2669\ nm)$, thereby the octahedron is trigonally distorted as shown in Figure 1.1d. The Fe and O arrangement (triplet

Iron mineral	Curie/Néel T (K)	Saturation magnetisation (Am^2/Kg)	Room temperature
FeO	203-211		Antiferromagnetic
$\gamma - Fe_2O_3$	948	63.6	Ferrimagnetic
Fe_3O_4	853	62.2	Ferrimagnetic
$\alpha - Fe_2O_3$		0.093-0.47	Antiferromagnetic with parasitic paramagnetism
$\alpha - FeOOH$	400	0.22	Antiferromagnetic
$\gamma - FeOOH$	52		Antiferromagnetic
$Fe_16O_16(OH)_y(SO_4)_z.nH_2O$	85		Antiferromagnetic

Table 1.2: Magnetic properties of iron oxide and hydroxide NPs at room temperature [1], [93]

structure $Fe{-}O_3{-}Fe$, Figure 1.1e) around shared faces affects iron oxide magnetic properties [96].

1.2.2 Magnetite Fe_3O_4

Magnetite is an inverse spinel structure [1]. It has a face-centered cubic unit cell based on 32 O^{2-} ions which are regularly cubic close-packed along *111* plane with unit cell edge length is $a = 0.839nm$. There are 8 formula units per unit cell. Magnetite differs from most other iron oxides in that it consists of both divalent (Fe^{II}) and trivalent (Fe^{III}) iron cations. Its formula is written as $Fe^{II}[Fe^{II}Fe_2^{III}]O_4$, where the brackets denote octahedral sites (M sites). Eight tetrahedral sites (T sites) are distributed between divalent and trivalent iron cations, i.e. the trivalent cations occupy both octahedral and tetrahedral sites. Magnetite structure consists of octahedral and mixed tetrahedral/octahedral layers stacked along *111* plane as it is shown in Figure 1.2a. The sequence of Fe and O layers is presented in Figure 1.2b whereas a section of this structure with 3 octahedra and 2 tetrahedra is presented in Figure 1.2c. Magnetite is frequently non-stoichiometric. It has a Fe^{III} cation deficient sublattice; $Fe^{II}/Fe^{III} \neq 0.5$ (in stoichiometric magnetite ($Fe^{II}/Fe^{III} = 0.5$) [1].

1.2.3 Maghemite $\gamma - Fe_2O_3$

Maghemite (magnetite-hematite) has a structure similar to that of magnetite. It differs from magnetite in that all or most iron atoms are in the trivalent state Fe^{II}. Cations vacancies compensate

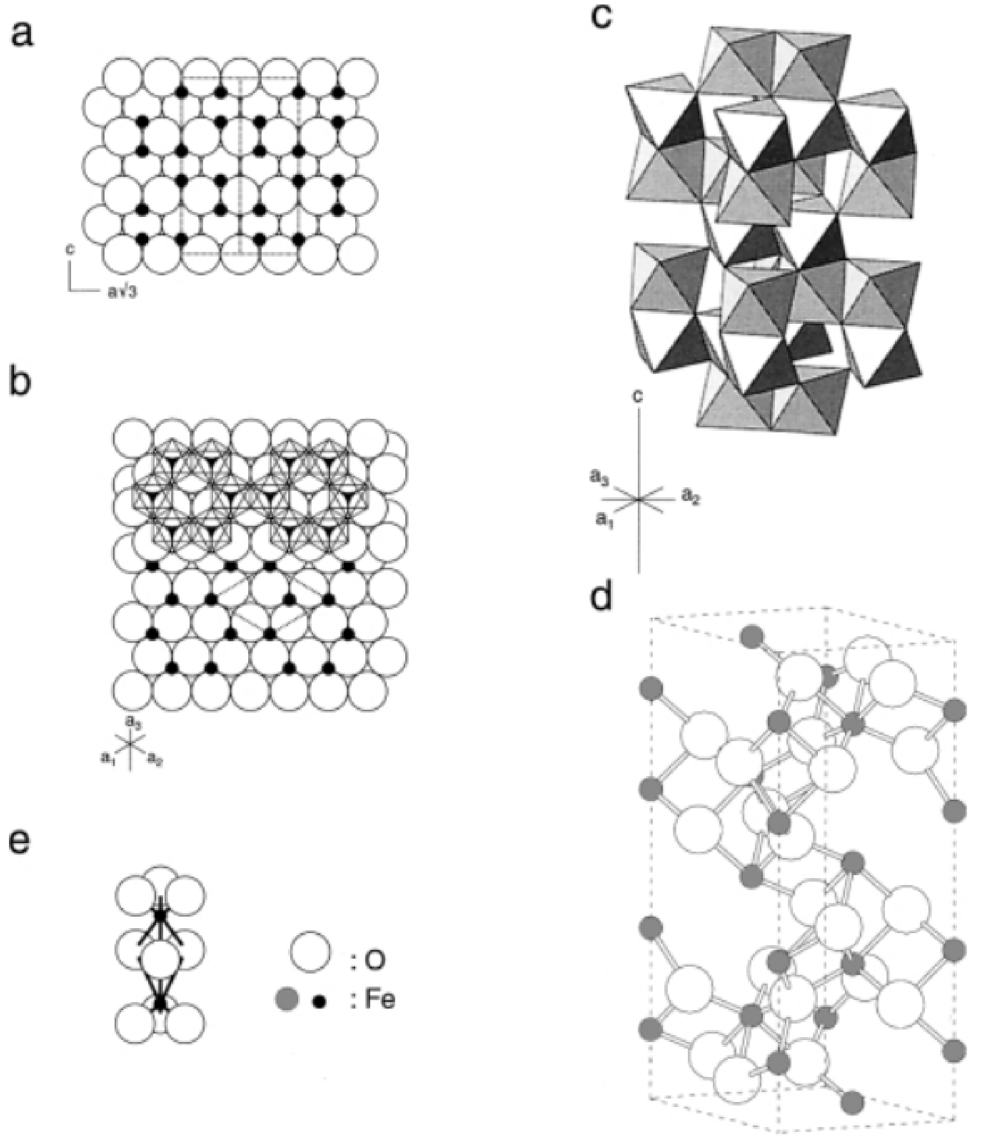

Figure 1.1: Structure of Hematite: (a) Hexagonal close packing of oxygen with iron cations distributed in the octahedral interstices, (b) View down of c-axis showing Fe cations distribution over a given oxygen layer and the hexagonal arrangement of octahedra [95], (c) Arrangement of octahedra with their face-sharing, (d) Ball-and-stick model and (e) $O_3-Fe-O_3-Fe-O_3$ triplets [96]

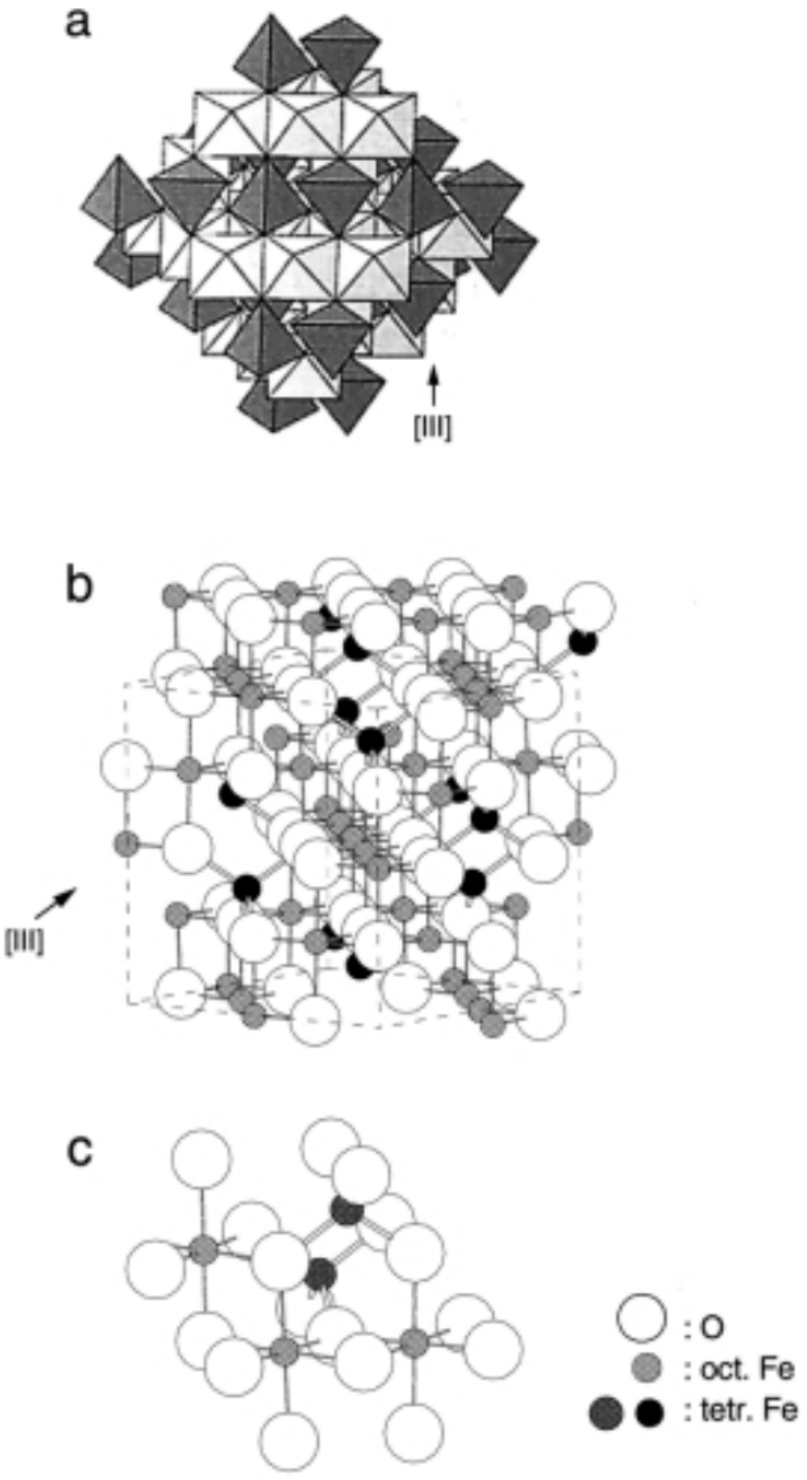

Figure 1.2: Structure of Magnetite. (a) The polyhedral model with alternating octahedral and tetrahedral-octahedral layers. (b) Ball-and-stick model. (c) Ball-and-stick model of the arrangement of octahedra and tetrahedra layers [96]

for the oxidation of Fe^{II}. Maghemite has a cubic unit cell with lattice parameter $a = 0.834\ nm$. Each cell contains 32 O^{2-} ions, 21 (1/3 Fe^{III}) cations, and 21 (1/3) vacancies. 8 iron cations occupy the tetrahedral sites and the remaining cations are randomly distributed over the octahedral sites. The vacancies are confined to the octahedral sites. This gives the following formula: $Fe_8^{IV}[Fe_{13.3}^{VI}\Box_{2.67}]O^{2-}$, where $\Box$ represents iron cation vacancies and the space group Fd3m [97].

1.3 Green Synthesis of Iron Oxide and Hydroxide NPs and Their Applications

Green synthesis of nanomaterials refers to the synthesis of different metal NPs using bioactive agents such as plant materials [44] and microorganisms (yeast, fungi, diatoms, and bacteria) [98], [99]. The involvement of natural bioactive agents in the synthesis of metal NPs greatly minimizes the risk of environmental pollution.

1.3.1 Green Synthesis of Iron Oxide and Hydroxide NPs

Several works in the literature dealt with iron oxide and hydroxide NPs green synthesis. Magnetite NPs have been successfully greenly synthesised from Hordeum vulgare and Rumex acetosa plants extracts [43]. Whereas Kumar et al. [70] synthesised magnetite NPs mediated by Andean blackberry leaf extract. The authors in [100] synthesised maghemite NPs using Chestnut tree (Castanea sativa), Eucalyptus (Eucalyptus globulus), Gorse (Ulex europaeus), and Pine (Pinus pinaster) extracts. Moreover, Jamzad et al. [101] synthesized hematite NPs using an aqueous extract of Laurus nobilis (L). leaves. Furthermore, Al-Ruqeishi [5] et al. synthesised hematite and maghemite NPs mediated by omani mango tree leaves as a reducing agent. Whereas Ehrampoush et al. [102] synthesised iron oxide NPs mediated by tangerine peel plant extract, and Xiao et al. [103] synthesised iron oxide NPs mediated by 15 plant extracts grown widely in the southeast of China including: A. moluccana Willd, C. camphora Presl, P. Orientalis Franco, B. variegata, Oolong tea, Black tea, A. carambola, E. citriodora, S. aromaticum, S. jambos Alston, D. longan Lour, N. indicum, G. robusta, D. regia, and speciosa Pers.

Iron oxy- and hydroxide NPs were also successfully greenly synthesized from black tea leaves extract [104], oolong tea leaves extract [105], and sorghum bran extract [106]. Where Demirezen et al. [107] synthesised lepidocrocite/maghemite NPs phases from Ficus carica (common fig) dried fruit extract. Likewise, Wang et al. [48] synthesised iron oxyhydroxide/oxide NPs using eucalyptus leaves extract. However, the authors in [108] synthesised zerovalent iron (ZVI) NPs from leaves extracts of different trees which are: apple, apricot, avocado, cherry, eucalyptus, kiwi, lemon, mandarin, medlar, mulberry, oak, olive, orange, passion fruit, peach, pear, pine, pomegranate, plum, quince, raspberry, strawberry, black tea, green tea, vine, and walnut.

1.3.1.1 Effect of Mediating Plant Extract on Iron Oxide and Hydroxide Physicochemical Properties

The mediating plant extract used in the green synthesis of iron oxide NPs is one of the parameters that may influence their physicochemical properties. Makarov et al. [43] studied the effect of pH of aqueous extracts of Hordeum vulgare and Rumex acetosa on the stability of magnetite NPs. They found that the synthesized magnetite NPs using H.vulgare extract were colloidally unstable and were prone to aggregation. However, magnetite NPs produced from Rumex acetosa plant extract were highly stables. The authors suggested that the higher stability of magnetite NPs synthesized by R.acetosa extracts was due to the presence of organic acids (such oxalic or citric acids) as stabilizer agents on the surface of magnetite. Xiao et al. [103] reported that the surface reactivity of greenly synthesised Fe NPs is consistent with the reducing capacity of plant extracts used. Where Wang et al. [48] demonstrated the tremendous potential of eucalyptus leaf-Fe NPs for in situ treatment of eutrophic wastewater in the removal of chemical oxygen.

Ehrampoush et al. [102] studied the effect of the concentration of tangerine peel plant extract on the size of iron oxide NPs. They found that the different concentration of tangerine peel extract has an impact on the size of iron oxide NPs. The increase of tangerine peel extract concentration from 2 to 6 $\%$ led to a decrease in the average size of synthesized iron oxide NPs from 200 nm to 50 nm. Whereas, Al-Ruqeishi [5] et al. reported that synthesised hematite and maghemite NPs nanorods mediated by omani mango tree leaves were formed with 15 ± 2 nm in average length and 3.0 ± 0.2 nm in average diameter. However, Jamzad et al. [101] reported that greenly synthesised hematite NPs from Laurus nobilis (L). leaves extract were crystalline, almost spherical like and partly as a hexagonal shape with an average size of 8.03 ± 8.99 nm. Whereas Demirzen et al. [107] found that greenly synthesised lepidocrocite/ maghemite NPs were produced smaller than 20 nm diameters and oxidized due to the high phenolic compound content in the common fig dried fruit extract.

In an other study [60], Huang et al. compared the capability of three plant extracts (green tea, oolong tea, and black tea) for the formation of ZVI NPs. The authors reported that green tea extract could produce more ZVI NPs as compared to the oolong and black tea extract. The synthesised NPs varied in aggregation state and size diversity depending on plant extracts, where Machado et al. [108] reported that the smallest ZVI NPs (5–10 nm) were formed by using mulberry and pomegranate leaf extracts.

1.3.2 Applications of Greenly Synthesised Iron Oxide and Hydroxide NPs

Iron oxide and hydroxide NPs have been widely used in several applications (as summarized in Figure 1.3), such as the treatment of various environmental contaminants [8], heavy crude oil cracking process [5], catalysts for efficient biodiesel production [6], and in environmental remediation activities [44].

Al-Ruqeishi et al. [5] studied the use of greenly synthesised $\alpha{-}Fe_2O_3$ and $\gamma{-}Fe_2O_3$ NPs from deciduous omani mango tree leaves for heavy oil viscosity treatment. They reported that the use of these iron oxide NPs increased the efficiency of microwave treatments for the dynamic viscosity of crude oil. The increase in the process efficiency was found to be in direct relation with the concentration of iron oxide nanorods, where the crude oil viscosity can be reduced up to 49% by using 0.6 g nanorods per liter of crude oil. El-Nahas et al. [6] use the sulfonated cellulose-magnetite nanocomposite (MSNC) as a catalyst in biodiesel production. They reported that this catalyst showed the highest catalytic activity toward the esterification reaction (96%) due to the high dispersion of the Lewis acid sites resulting from the impregnation of magnetite NPs (0.98 wt%). However, Kumar et al. [70] synthesised magnetite NPs from Andean blackberry leaves extract to use in the removal of three organic dyes. They found that magnetite NPs showed a high photocatalytic activity in the removal of Congo red, methylene blue, and methyl orange.

Jassal et al. [73] synthesised iron hydroxide $\alpha{-}FeOOH$ NPs using Sapindus mukorossi extract, to use in the removal of 2, 3, and 4-aminopyridines. They found that produced nanorods of $\alpha{-}FeOOH$ showed a high catalytic activity due to their high surface area. In [101], authors synthesised hematite NPs mediated by Laurus nobilis L. leaves extract to evaluate their antimicrobial activity against three bacteria and two fungi. They found that these NPs showed moderately effective on the gram-positive bacterium of Listeria monocytogenes, the fungi Aspergillus flavus, and Penicillium spinulosum. Furthermore, Xiao et al. [103] synthesised Fe NPs by three plant extracts to use them in Cr (VI) removal. They found that S. JambosL.Alston extract showed a

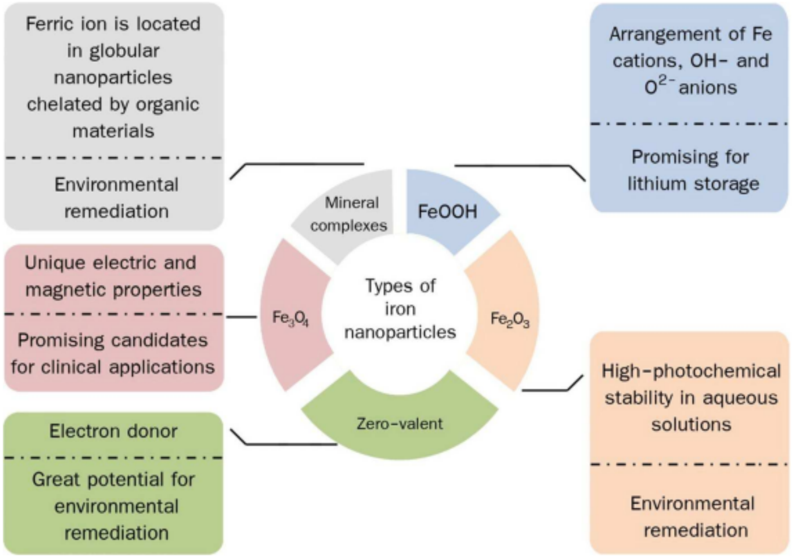

Figure 1.3: The applications of iron oxide and hydroxide NPs [44]

significant removal capacity of Cr (VI) with 698.6 mg Cr (VI) per g of iron. Also, Wang et al. [48] synthesised iron oxyhydroxide/oxide NPs from eucalyptus leaf extracts to use them in wastewater treatment. They demonstrated the tremendous potential of eucalyptus leaf-Fe NPs for in situ treatment of eutrophic wastewater where the removal of chemical oxygen reached 84.5%.

1.4 Wüstite NPs Structure

Stoichiometric wüstite NPs, FeO, cannot exist as a stable phase at low pressures or at pressures exceeding 10 MPas [4]. The nonstoichiometric wüstite is denoted Fe_xO where x represents iron composition and $1 - x$ represents Fe^{2+} vacancies (defects). It always contains more oxygen than that in the stoichiometric wüstite ($O/Fe > 1$). The nonstoichiometric is accommodated by oxidation of proportion of iron cations and formation of cation vacancies. A stable cation-deficient phase of Fe_xO with iron stoichiometry x ranging from 0.83 to 0.96 exists at 0.1 MPas pressure and temperature greater than 567 $°C$ [25]. Wüstite disproportionates to Fe metal and Fe_3O_4 when cooled slowly to temperatures lower than $567\ °C$. If however Fe_xO is rapidly quenched, the nonstoichiometric form can be obtained as a metastable phase at ambient temperature [25]. Wüstite will be oxidized completely to Fe_3O_4 in about 4 months in ambient conditions [26].

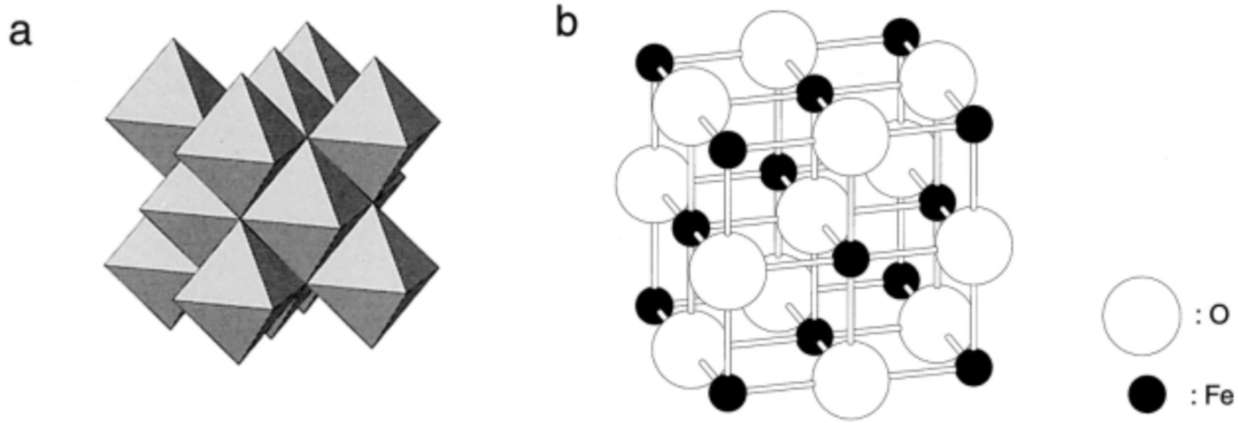

Figure 1.4: Structure of wüstite. (a) Arrangement of octahedra layers. (b) Ball-and-stick model [96]

1.4.1 Defects Within Crystal Structure: Definitions and Types

1.4.1.1 Crystal Defects Definition

Crystal defects are an imperfection or a deviation from the perfect atomic geometrical arrangement of the atoms in a crystalline solid structure. These imperfections result from deformation of the solid, rapid cooling from high temperature, or high-energy radiation (X-rays or neutrons) striking the solid. Crystal defects may be Located on a single point, long lines, or on whole surfaces in the solid structure [109]. Many solid surface properties are controlled by these defects such as structural [33], [34], physical [29], electrical, and optical [35]–[38].

1.4.1.2 Types of Crystal Defects

Point Defects

Point defects include vacancies, interstitial atoms, impurity atoms, and the combination of all these types. The most known of them are:

- **Schottky defect**: it consists of an atomic site from which the atom is missing which leads to an anion and a cation vacancy. The absence of an atom would change the balance of forces near the vacancy. The atoms in the vacancy neighborhood will shift their positions slightly inward until a new equilibrium configuration is reached [109], [110].

- **Frenkel pair defect**: it involves in first a single cation, which is displaced from its normal lattice point, and in second this displayed cation shifts to a nearby unoccupied site in the lattice. This is called an interstitial defect. So, in Frenkel pair defect, if an interior atom was to displace into an interstitial position, both a vacancy and interstitial defect would be created at the same time [109], [110].
- **Interstitial defect**: it consists of the presence of an atom in a normally unoccupied site, that is, a site between normal lattice sites. An interstitial may be self interstitial wherein the same atom belonging to the lattice is misplaced in the interstitial position or it may be a foreign atom in the interstitial position [109].
- **Impurity defect**: it is a foreign atom that replaces some of the atoms making up the solid or that squeeze into the interstices [109].

Line Defects

Line defects, or dislocations, are defined as lines along which whole rows of atoms in a solid are exceptionally arranged. The resulting irregularity in spacing is most severe along a line called the line of dislocation. Line defects can weaken or strengthen the solid structure [110].

1.4.2 Defects Within Wüstite NPs Structure

The pioneering Roth study [111] showed, for the first time, that cation vacancies and interstitial iron cations occur both in sublattice of the wüstite crystalline structure. Thus Frenkel defect pair is simultaneously formed by the transfer of a trivalent octahedral iron cation Fe^{3+} to a tetrahedral interstitial site [111]. Thereby the presence of the Frenkel point defect is a consequence of a departure from the stoichiometric composition FeO to the nonstoichiometric composition Fe_xO. This departure causes instability in the total wüstite crystal electroneutrality. In order to preserve the total crystal electroneutrality of Fe_xO, some of the Fe^{2+} cations liberate another electron and become Fe^{3+} cations. The Fe^{2+} cation deficiency is attributed to the formation of neutral vacancies on cation sublattices together with Fe^{3+} cations which provide charge compensation with the aim of preserving the total crystal electroneutrality of Fe_xO. This means that for a given value of x (iron composition in Fe_xO), there are $2(1-x)Fe^{3+}$ and $(1-3(1-x))Fe^{2+}$ cations.

This iron deficiency leads to the formation of $1-x$ cation vacancies. These vacancies are partly located on interstitial tetrahedral sites [28].

The detailed representative structure of Fe_xO is thus [29]: $Fe^{2+}_{1-3(1-x)}Fe^{3+}_{2(1-x)}\square_{1-x}O^{2-}$ where $\square$ represents iron cation vacancies. The formation of those cation vacancies is responsible for charge redistribution and appearance of Fe^{3+} cations in the octahedral and tetrahedral (interstitial) sites [28], [30], and they are the cause that Fe_xO having interesting properties [1], [29].

Catlow and Fender [28] are the first who suggested that the basic building block in wüstite cluster is identified as a complex of 4 cation vacancies and 1 tetrahedral Fe^{3+} cation; [4:1] cluster (see Figure 1.5a). [4:1] basic building block cluster is formed as a result of a large Coulomb term favoring the occupation of the tetrahedral site when all nearest-neighbor cations are vacant. Full charge compensation requires the presence of 5 octahedral Fe^{3+} cations at lattice sites surrounding the cluster of wüstite NPs. Charge compensation has a large effect on cluster stability; the increase in binding energy leads to the increase of full charge compensation and consequently the stability approaches. The Fe^{3+} charge compensating cations occupy first the neighbor sites. Furthermore, the distribution of the charge-compensating ions around the cluster has only a marginal effect on its stability in all types of clusters, so long as the Fe^{3+} cations are approximately uniformly distributed [28]. The aggregation of these clusters occurs by vacancy-sharing may occur with edge-sharing, corner-sharing, and Face-sharing, as presented in Figure 1.5.

Catlow et al. [28] suggest that the most stable small defects aggregates are formed by edge-sharing rather than corner-sharing (e.g. the Koch-Cohen cluster [6:2] or [8:3] clusters). The authors confirmed that the binding energy per net vacancy increased when [4:1] cluster is formed from isolated point defects. They then demonstrated that the binding energy increases further when [4:1] clusters share faces to form firstly [6:2] and secondly [8:3] clusters (Fig.1.5). Edge-sharing, therefore, appears to be the most favored mode of interaction for the formation of small aggregates of [4:1] defects. But the growth of clusters by this mode of sharing is evidently limited.

1.4.2.1 Influence of Structural Defects on Wüstite NP Properties

The physical and chemical properties of wüstite have attracted continuous attention for decades [29], [36]. This unflagging interest results from both practical and cognitive reasons. Wüstite constitutes, for instance, the main part of the oxide scale on iron and iron-based alloys, and plays an important role in the reduction processes of iron ores. The extremely large homogeneity range of this oxide, in turn, results in very high, and consequently complicated, electronic and ionic disor-

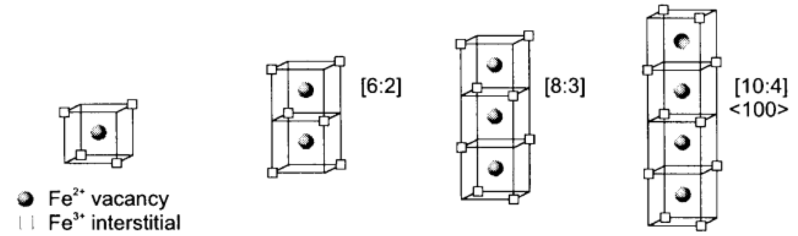

(a) [4:1] cluster (b) <100> type clusters

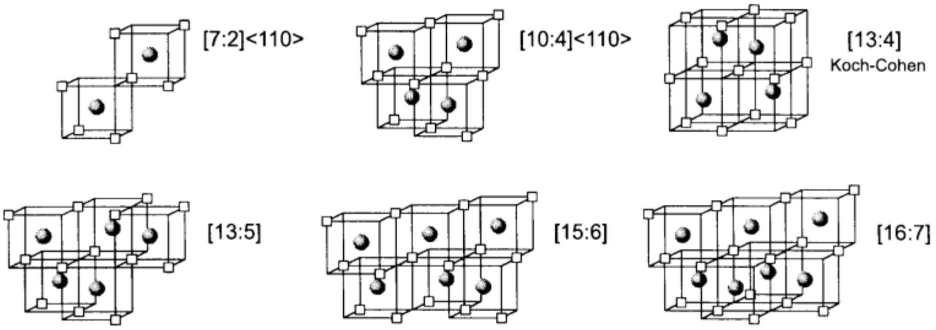

(c) <110> zincblende type clusters

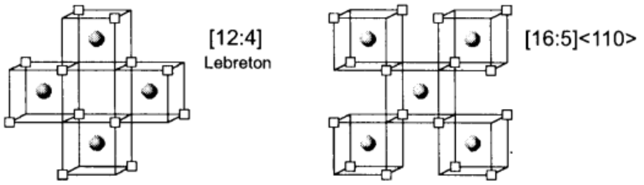

(d) <110> Lebreton-Hobbs type clusters

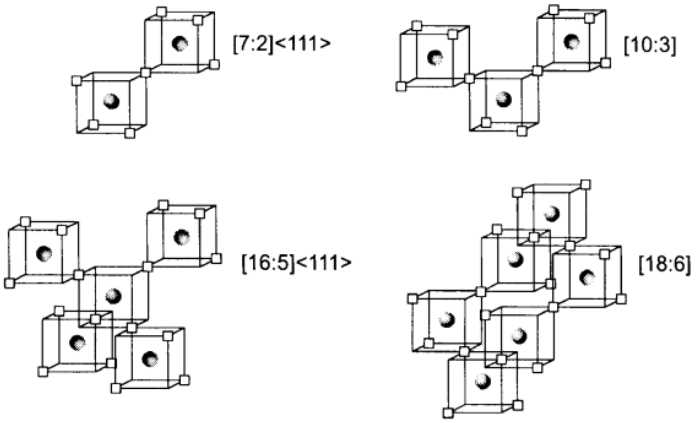

(e) <111> spinel type clusters

Figure 1.5: Different defect clusters [33]

der. The defect and transport properties of wüstite are then the object of extensive experimental studies and theoretical consideration [28], [29], [33].

The study of cation vacancies' effect on Fe_xO properties makes the subject of extensive experimental studies and theoretical considerations. It was reported that cation vacancies have an effect on wüstite formation reaction thermodynamic [31], [32], structural [33], [34], physical [29], electrical, and optical properties [35]–[38]. Wdowik et al. [39] reported that cation vacancies have an effect on electronic and dynamical properties of wüstite. Zhang et al. [40] found that iron defects have a strong effect on the elastic properties of wüstite. Bowen et al. [36] studied the optical properties of $Fe_x0.8772O$, $Fe_x0.8928O$ $Fe_x0.9174O$ and $Fe_x0.9523O$ NPs. They reported that optical properties were independent of iron stoichiometry within wüstite. Wetterskog et al. [112] studied the effect of internal defects on wüstite magnetic properties. They found that internal defects play an important role in dictating the magnetic properties of wüstite NPs.

1.4.3 Methods of Wüstite NPs Synthesis

Several methods have been developed for the synthesis of wüstite NPs such as physical, chemical, and green methods.

1.4.3.1 Physical and Chemical Methods of Wüstite NPs Synthesis

Strobel et al. [113] synthesised wüstite NPs by flame spray pyrolysis physical process. The Fe oxidation state was controlled by varying the fuel to air ratio (ψ) during combustion as well as by varying the valence state of the applied Fe precursor. They reported that an increase of ψ above 1 promoted wüstite NPs formation. Pure wüstite, however, could not be prepared as a further increase of ψ resulted in unstable flame conditions. However, in the study of Gheisari et al. [114] wüstite NPs have been prepared by mechanochemical processing (MCP), where high-purity hematite ($\alpha{-}Fe_2O_3$) and iron (Fe) powders as the raw materials were milled with different mole ratios of (Fe/Fe_2O_3). The authors announced that a single-phase $Fe_{0.93}O$ has formed with a crystallite size of 13 ± 1 nm. Whereas, Hiramoto et al. [115] synthesised nonstoichiometric Fe_xO (x = 0.833-1) NPs by self-propagating high-temperature synthesis (SHS) using Fe, $NaCl_4O$ as oxidizer and NaCl as a diluent, with particular focus on the effects of nonstoichiometric Fe content and diluent addition on the phase of the SHS product. They reported that in the presence of the NaCl diluent, the raw materials were converted to high-purity Fe_xO powders during the SHS process. Without the NaCl diluent, the lattice parameter of SHS $Fe_{0.947}O$ corresponded to the theoretical lattice parameter. Nonstoichiometric compounds of Fe_xO (0.942 $\leq$ x $\leq$ 0.952) were obtained through SHS without additional external heating.

Park et al. [116] synthesised wüstite NPs by the thermal decomposition process. They found that $\alpha - Fe_2O_3$ NPs were transformed into well-crystallized $Fe_{0.935}O$ after heat treatment at $1373\ °C$ during 84 h. Likewise, Yin et al. [117] synthesised wüstite NPs by thermal decomposition method of iron (II) acetate in the presence of oleic acid as the surfactant at $250°C$ during 2h. They found that a well-stabilized $Fe_{0.8870}O$ phase was formed. Moreover, Spivakov et al. [118] synthesised wüstite NPs by thermal decomposition process at a temperature of $400°C$ and the reaction time varied from 1 to 3h for the purpose of studying the effect of time reaction on the stoichiometry and the purity of wüstite NPs. They reported that the stoichiometry of wüstite can be changed by the change of synthesis time. The increase in the reaction time led to the formation of phase pure wüstite NPs.

The main inconvenience of physical and chemical methods is the employ of toxic chemicals as reducing agents, organic solvents, or nonbiodegradable stabilizing agents. Therefore, they become potentially dangerous to the environment and biological systems. Furthermore, most of these methods require complex controls or nonstandard conditions making them quite expensive [119]. They also suffer from the limitations of being time and energy-consuming because the raw materials must be kept at a high temperature for an extended period in order to reach the equilibrium composition of wüstite NPs [31].

1.4.3.2 Green Synthesis of Wüstite NPs

The green synthesis of iron oxide NPs is an emerging technique attracting more attention in recent years due to their availability, low cost, and eco-friendliness over the conventional chemical/physical processes [120], [121]. During iron oxides synthesis, phytochemicals can play the role of reductants and capping agents. Nature represents an extraordinary reservoir of phytochemicals in the form of polyphenolics, carotenoids, terpenes, flavonoids, steroids, saponins, proteins, lipids, etc [42], [44].

Only a few reports in the literature have investigated the green synthesis of wüstite (Fe_xO) NPs. In the study of Herrara et al. [46], they synthesized $Fe_{0.92}O$ NPs using Medicago sativa (alfalfa) plant extract. Kumar et al. [47] synthesized stable wüstite NPs using aqueous extract of Terminalia chebula dry fruit pericarp. In [48], Wang et al. synthesized wüstite using leaves of Eucalyptus tereticornis. Muthukumar et al. [122] synthesized wüstite NPs from Amaranthus spinosus leaf extract as reducing agent and chemically from sodium borohydride as reducing agent in order to study the effect of mediated plant extract on wüstite morphology and antioxidant capacity. They found that greenly synthesised wüstite NPs were stoichiometric FeO NPs having a spherical shape with rhombohedral phase structure, smaller size, and large surface with less aggregation. Additionally, these greenly synthesised NPs showed a better antioxidant capacity than sodium borohydride-mediated NPs. Ahmouda et al. [123] synthesised wüstite NPs from four plant aqueous extracts: Rosemarinus officinalis.L, Juniperus phoenicia.(L), Matricaria Pubescens.(L), and Artemisia herba-alba.(L). They found that plant extract had an effect on both iron vacancies within wüstite NPs and wüstite NPs size. Iron cation vacancies within synthesised wüstite NPs from Rosemarinus officinalis.L, Juniperus phoenicia.(L), Matricaria Pubescens.(L), and Artemisia herba-alba.(L) were respectively $ROS - Fe_{0.9060}O$, $JUN - Fe_{0.8720}O$, $MAT - Fe_{0.8560}O$ and $ARM - Fe_{0.8319}O$, with different grain sizes 36.07, 29.87, 24.08, and 20.64 nm, respectively.

1.4.4 Applications of Wüstite NPs

Situ et al. [124] used FeO and Fe_3O_4 as precursors for fabricating smaller iron oxide/carbon nano chains. They reported that nano chains fabricated from FeO NPs can reach above 2-fold enhancement in microbe-killing activity when compared to the larger nano chains fabricated directly from Fe_3O_4 NPs. Pernicone et al. [125] used wüstite as a new precursor of industrial ammonia synthesis catalysts. They reported that the presence of wüstite as the only crystalline phase in catalyst precursor is indispensable for high catalyst activity. The high activity referred to bed volume of wüstite-based catalyst which is due in part to its higher density, but mostly to the higher efficiency of Fe surface sites in the activation of dinitrogen. Chavez-Galan et al. [126] studied the use of wüstite NPs as solar filters when deposited onto soda-lime glass substrates and they reported the efficiency of wüstite as solar filters. As result, a significant reduction in required energy for heating and cooling was observed.

Wang et al. [48] studied the use of wüstite NPs in the removal of chemical oxygen from eutrophic wastewater. They demonstrated the tremendous potential of wüstite for in situ treatment of eutrophic wastewater, where the reached yield of chemical oxygen removal was 84.5%. Muthukumar et al. [122] greenly synthesized wüstite NPs from Amaranthus spinosus leaf extract and chemically synthesised wüstite NPs from sodium borohydride to use them in the removal of methylene blue and methyl orange under sunlight. They found that greenly synthesised wüstite displayed a strong photocatalytic activity in the removal of methyl orange and methylene blue with 75% and 69%, respectively, in contrast to chemically synthesized NPs.

1.4.5 Wüstite Oxidation to Magnetite NPs

Wüstite is an antiferromagnet with a Néel temperature (TN) of approximately $200\ K$, below which the spins are antiparallel. However, bulk wüstite is only stable above $560°C$ and remains in a metastable phase under ambient conditions when rapidly quenched from temperatures at which it is stable. This metastable phase can undergo a disproportionation reaction to Fe and Fe_3O_4 [26], [127].

$$Fe_xO \rightarrow Fe_yO + Fe_3O_4 \tag{1.1}$$

Chen et al. [26] studied wüstite oxidation during 4 months under ambient conditions. They found that as the storage time increases, the spinel-type phase becomes dominant. The study of Catlow et al. [28] established that the modification of iron composition within FeO is accompanied by the aggregation of a basic cluster [4:1] in which four Fe^{2+} vacancies at octahedral sites surround each Fe^{3+} ion that is located in tetrahedral interstitials. The aggregation of these basic clusters by edge and corner-sharing can generate clusters of various sizes, and the larger [16:5] clusters can be regarded as a partial Fe_3O_4 structure. Accordingly, the oxidation of some Fe^{2+} in FeO NPs may promote the formation of the extended spinel-type Fe_3O_4. The gradual oxidation of FeO slowly changes the composition from wüstite to the spinel-type Fe_3O_4 phase.

1.5 Conclusion

In this chapter, a background on iron oxide and hydroxide NP structures, properties, defects, types, and applications were presented. Furthermore, wüstite formation defects (mainly cation vacancies), methods of synthesis, and synthesis conditions' effect on their physicochemical properties was detailed. Moreover, an overall discussion of the state of the art on the green synthesis of iron oxide and hydroxide NPs, plant extract effect on physicochemical properties of iron oxides/hydroxides, and their applications has been done. This chapter also presented wüstite NP synthesis methods and conditions and their effect on its physicochemical properties. Particularly green synthesis methods and mediated plant extract effect on physicochemical properties of wüstite NPs and their applications are discussed. The presented chapter would be useful to express the first contribution to present in the chapter 3, in which the effect of plant extract FRAP on cation vacancies formation in greenly synthesised wüstite will be presented.

Chapter 2

Nanomaterials Surface Reactivity in Dye Adsorption

2.1 Introduction

Dyes are highly used in various industries including plastics, rubber, textile, paper, and coating. However, the discharge of dyes into water effluents has raised global concerns over their major inconvenient effect on the environment [128]. Thus the development of technologies to reduce their discharge and contamination is very important.

Adsorption is currently considered to be a very suitable method for wastewater treatment because of its simplicity and cost-effectiveness. For that, it is a commonly used technique for the removal of dyes from wastewater [16], [23], [129]. Iron oxide nanomaterials are one of the widely used adsorbents for removing contaminants [130], [131].

The reaction in the nanoparticles-dye adsorption process is a surface-mediated process. Thus, the reaction rate, yield, and adsorption capacity are related to NPs surface properties from one side and to dye properties from another side [132]. According to [23], [24], the dominant mechanism for dyes adsorption on iron oxide NPs surfaces under most solution conditions is surface complexation through electrostatic interactions. They reported that dyes are almost dissociated at the surface, which is an important step for adsorption. The interactions between these dissociated dyes and specific sites on iron oxide surface functional groups, which occur to stabilize charges, facilitate the adsorption process through binding different types of bonds on their surfaces. Surface hydroxyl groups, with amphoteric properties, are the functional groups of iron oxide surfaces and they are their chemically reactive entities that behave as the active sites upon the adsorption process. These hydroxyl groups may be singly, doubly, and triply coordinated to Fe atoms having different reactivity. The overall density of these groups depends on both the crystal structure and the extent of development of the different crystal faces [54].

The electric double layer interaction is the main surface force responsible for the attachment of the particles to the surface. It originates from the charge that develops on the surface of particles immersed in an aqueous solution. A colloidal particle of iron oxide in an electrolyte solution carries the surface charge due to adsorption of ions (called potential determining ions) on its surface or due to dissociation of hydroxyl groups ((OH_z)) formed on the surface [133]. When this group reacts with the acidic and basic species from the water environment the surface charges were formed. The positive charge ($Fe - OH_2^+$) on the oxide comes from the addition of a proton to the neutral surface hydroxyl group, while the negative charge ($Fe - O^-$) arises from the acidic dissociation of the surface hydroxyl group and loss of a proton. Consequently, the protons and hydroxyl ions are identified as potential determining ions. Adsorption or desorption of protons is determined by the pH of the solution [134], [135].

2.2 Adsorption Process for Dye removal

2.2.1 Adsorption Process Definition and Types

Adsorption is a physicochemical surface interaction between the adsorbate and the adsorbent. Adsorption is a spontaneous process that takes place if the free energy of adsorption is negative. There is a wide range of energies contributing to the free energy of adsorption, which can be grouped into non-electrostatic and electrostatic.

$$\Delta G_{ads} = \Delta G_{non-elec} + \Delta G_{elec} \tag{2.1}$$

Although at the atomic level all ionic and molecular interactions can be interpreted as electric, this term is restricted to Coulomb interactions, and all other interactions are termed non-electrostatic, whatever their origin. Electrostatic interactions appear when the adsorptive is an electrolyte that is dissociated or protonated in an aqueous solution under experimental conditions. These interactions, which can be either attractive or repulsive, strongly depend on the charge densities for both the adsorbent surface and the adsorptive molecule and on the ionic strength of the solution. The non-electrostatic interactions are always attractive and can include van der Waals forces, hydrophobic interactions, and hydrogen bonding. Factors that influence the adsorption process are the characteristics of the adsorbent, adsorptive, and solution chemistry [136].

2.2.1.1 Physical and Chemical Adsorption

The adsorption can be categorized based on their interaction with the adsorbate into chemisorption or chemical adsorption and physisorption or physical adsorption, as detailed below:

- **Chemisorption** is usually accomplished by the chemical reaction between the adsorbate and adsorbent and is an irreversible approach. In chemisorption, there is an ionic or chemical interaction between adsorbent and adsorbate. Generally, chemical adsorption is an irreversible process and it is found to be highly efficient [137].
- **Physisorption** is reversible in most cases [137]. In physisorption, weak attractive electrostatic interactions, hydrophobic interactions, hydrogen bonding, polar-polar interaction, π-stacking, cation-π interactions, and van der Waals forces are typical examples of the intermolecular forces that dominate the interaction of dye molecules with the surfactant aggregates in the adsorption process. Such a type of adsorption is more prominent and reversible. Therefore, adsorbents can be easily regenerated for their use in subsequent batches [138].

2.2.2 Factors Influencing Adsorption Process

The effect of several factors on dyes adsorption on iron oxide NPs has been studied in several works such as solution chemistry [16], [54], the characteristics of dye [16], [55], and adsorbent surface functionally [59], [60], [139]–[141].

2.2.2.1 Effect of Solution pH and Ionic Strength

The solution pH and ionic strength are important parameters that affect dye adsorption. Saha et al. [16] studied the effect of solution pH and the ionic strength (NaCl) on the adsorption of different dyes. They found that the adsorption capacities of erichrome black T, bromophenol blue, bromocresol green, and fluorescein dyes were high in the pH range of 4 to 6. They suggested that it is mainly due to the surface complexation of the deprotonation dyes on the magnetite surface over this pH range. Magnetite particles have a PZC (point of zero charges) of 6.4-6.7. At a pH below the PZC, the magnetite surface remains protonated, which can form hydrogen bonding with dye molecules to facilitate adsorption. However, they found that the influence of ionic strength in the range from 0.01 to 0.1 M did not have any significant effect on studied dyes' adsorption processes.

Likewise, Pirillo et al. [54] studied the effect of solution pH on the adsorption of Alizarin and Eriochrome Blue Black R onto three different adsorbents: goethite, Cogoethite, and magnetite NPs. They reported that at low pH, the amounts of Alizarin and Eriochrome Blue Black R adsorbed on goethite and Co-goethite are similar. However, a higher dependence with the increase of pH is observed by Eriochrome Blue Black R. On magnetite, the dye adsorption shows less affinity for both dyes. Moreover, Weng et al. [57] studied the effect of solution ionic strength ($NaClO_4$) at different concentrations on acid dye; new coccine (NC) adsorption on magnetite NPs. They found that the amount of NC adsorbed decreased with increasing supporting electrolyte concentration. They suggested that the increase of ionic strength can affect the electrical double layer structure of a hydrated particulate because of the increase of the competition between NC^{-} and ClO_4^{-} ions for surface sites.

2.2.2.2 Effect of Adsorbent and Dye Concentrations

Saha et al. [16] studied the effect of magnetite NPs (adsorbent) concentration on different dyes' adsorption. They reported that the increase in magnetite NPs concentration resulted in a decrease in adsorption capacity of erichrome black T, bromophenol blue, bromocresol green, and fluorescein dyes. They suggested that the decrease in adsorption capacity value with the increase in magnetite concentration is mainly due to the presence of more surface area for a fixed amount of adsorbate. Likewise, Borth et al. [58] studied the effect of congo red dye concentration on its adsorption on iron oxide NPs. They found that the CR adsorbed quantity increased as the initial concentration increased until there was an adsorbent saturation, followed by a little sharp decrease. They suggested that the increase proportional to the dye concentration increase is explained due to the super action of the mass transfer resistance by the higher driving force and, also, by the increase of the collisions between the CR and the adsorbent molecules. On the other hand, the adsorbed dye percentage decreases, because the higher molecules quantity generates competition for the active sites on the solid surface.

In [57] authors studied the effect of acid dye; new coccine (NC) concentration on adsorption on magnetite NPs. They reported that the increase of NC concentration leads to the increase of adsorption capacity due to the fact that the higher the NC concentration the stronger is driving forces of the concentration gradient exhibits and thus showing a higher adsorption capacity. Where authors in [142] studied the effect of adsorbent (iron NPs loaded on ash) concentration on malachite green adsorption. They found that as the adsorbent dose increases, the adsorption removal percentage also increases but the reverse trend is followed for the adsorption capacity (q_e) i.e. on increasing the adsorbent dose the adsorption capacity decreases. They suggested that this is due to the increase in the adsorptive surface area and the presence of a large number of active sites and the lesser biosorption ability of malachite green at an elevated nano adsorbent dose is due to the fact that there is the adsorption competition among adsorbent molecules and the splits present in the concentration gradient.

2.2.2.3 Effect of Physicochemical Properties of Dye

Saha et al. [16] studied the adsorption of seven different dyes on magnetite NPs. They reported that dyes containing higher OH content were more adsorbed on magnetite NPs surface. Likewise, Xiao et al. [55] studied the adsorption of different cationic and anionic dyes on iron NPs. They reported that cationic dyes were more adsorbed on iron NPs than anionic dyes. Moreover, Madrakian et al. [56] studied the adsorption of seven cationic and anionic dyes on magnetite-coated waste tea. They reported that cationic dyes were more adsorbed on this nano adsorbent compared to anionic dyes. Where, Valadi et al. [143] studied the selective separation of Congo Red from a mixture of anionic and cationic dyes using $La{-}MOF{-}NH_2@Fe_3O_4$ (magnetic-MOF). They found that Congo red was highly and quickly separated from the mixture with 92.02% removal after 2 minutes, due to the fact that Congo red can have stronger electrostatic and host-gust interactions with magnetic-MOF.

2.2.2.4 Effect of Mediating Plant Extract Properties in The Adsorbent Properties

The impact of changing mediating plant on greenly synthesized metal oxide NPs behavior in dyes adsorption was studied in several works. Huang et al. [60] synthesized Fe NPs from three different tea extracts: green, oolong, and black teas, in order to use them in the removal of malachite green. They reported that malachite green (MG) adsorption was the highest (81.2%) on Fe NPs synthesized by green tea extracts because it contains a high concentration of caffeine/polyphenols which act as both reducing and capping agents in the synthesis of Fe NPs. Additionally, Duyen et al. [61] synthesized metal oxide NPs using the extracts of flowers, bark, and the leaves of Tecoma stans in order to use in the removal of Congo red (CR) and crystal violet (CV). They reported that the nano adsorbent synthesised using flower extract gave a better adsorption efficiency than those synthesised from other plant extracts.

In [62] authors synthesized magnetite NPs using six plant extracts in order to use them in the removal of methyl orange (MO) and crystal violet (CV). They found that plant extract had an effect on magnetite NPs surface reactivity in the adsorption, where magnetite NPs synthesized using tea extract showed the highest performance (MO 92.34%, CV 96.1%). Where in [129], the adsorption of crystal violet and methylene blue on magnetite NPs loaded Azolla (MNLA) has been studied. The authors found that MNLA preferred adsorbing crystal violet more than methylene blue.

2.2.2.5 Effect of Modified Adsorbent Surface functionality by Binding Ligands

Other authors studied the effect of adsorbent surface functionality by binding ligands on the adsorbent surface. Khurshid et al. [139] found that the bind of amine-functionalized to cobalt–iron oxide NPs surface enhanced the removal of anionic azo dyes. Whereas the study of Madrakian et al. [144] reported that magnetite-modified activated carbon preferred adsorbing cationic dyes than anionic dyes. They suggested that a rapid adsorption rate is mainly attributed to the activated carbon structure and functional groups on the adsorbent providing a large surface area and good affinity for the facile and fast cationic dyes much higher than the anionic dyes. Where Chamchoy et al. [145] compared the adsorption of methylene blue on sericin-modified and unmodified with magnetite NPs. They declared that sericin-modified with magnetite NPs was approximately 40% more effective than the unmodified magnetite NPs in the removal of methylene blue.

2.2.2.6 Effect of Surface Hydroxyl Groups Density

Surface active sites densities were also found to impact the adsorption process. Indeed, a study of the adsorption of organic contaminants on both natural and synthesized magnetite [59] found that the adsorption on natural magnetite was more efficient than the synthesized one, and this is because of its higher surface active sites density. Moreover, Gogoi et al. [146] studied the degradation of catechol using $Fe_3O_4 - CeO_2$ nanocomposite as a Fenton-like heterogeneous catalyst. They reported that the increase of Brönsted acid sites density of this nanocomposite increased the degradation of catechol. Valdes et al. [147] studied the influence of zeolite surface active sites on the adsorption of volatile organic compounds (VOCs). They found that Brönsted and Lewis acid sites of the adsorbent surface could be mainly responsible for the abatement of VOCs.

2.2.3 Preferential Adsorption of Dyes on Iron Oxide NPs

The preferential adsorption of dyes on iron oxide NPs has been studied in several works. Saha et al. [16] studied the preferential adsorption of seven different dyes on magnetite NPs. They reported that magnetite surface preferred adsorbing dyes containing higher OH content. Xiao et al. [55] studied the preferential adsorption of different cationic and anionic dyes on iron NPs. They reported that iron NPs preferred removing cationic dyes more than anionic dyes. Madrakian et al. [56] studied the preferential adsorption of seven cationic and anionic dyes on magnetite-coated waste tea. They reported that studied nano adsorbent preferred more adsorbing cationic dyes compared to anionic dyes.

2.3 Dye Adsorption process under Thermo- and Photocatalysis

Photo- and thermocatalysis processes are clean, sustainable, and environmentally friendly processes to decompose or degrade organic pollutants. The photo- and thermocatalysis remediation approaches eliminate the organic pollutants from the wastewater without the persistence of toxic products as they completely decomposed the hazardous compounds or converted them into non-toxic forms. The photo- and thermocatalysis remediation are advanced oxidative processes, which take place in the presence of a photo- and thermocatalyst [148].

2.3.1 Mechanisms of Thermo- and Photocatalysis Processes

Thermo- and photocatalysis mechanisms are based on electron excitation by phonons and photons absorption respectively. The mechanisms are summarized in Figures 2.1a and 2.1b, and detailed as follow:

- In the first step, thermo- and photocatalytic materials absorb the phonons/photons have energy equal to or more than their band gap energy between the valence and conduction bands. The phonons/photons absorption causes the charge separation by exciting electrons from the valence to the conduction band followed by the generation of positive holes in the valence band [149], as presented in the following equations:

$$Catalyst + Heat/Light \rightarrow Catalyst(h^+ + e^-) \tag{2.2}$$

$$Catalyst + Heat/h\nu \rightarrow Catalyst(e^-(CB) + h^+(VB)) \tag{2.3}$$

- In the second step, the positive holes either oxidize adsorbed water molecules to produce hydroxyl radical $OH^\bullet$ as presented in the equation 2.4. Whereas excited electrons reduce adsorbed oxygen molecules on photo- and thermocatalyst surfaces in the conduction band to produce superoxide ions as presented in the equation 2.5, which may not only take part in the further oxidation process but also prevents the electron/hole pairs recombination, thus maintaining electron neutrality on photo- and thermocatalyst surfaces,

$$h^+ + H_2O \rightarrow OH^\bullet + H^+ \tag{2.4}$$

$$O_2 + e^-(CB) \rightarrow O_2^{-\bullet}(ads) \tag{2.5}$$

- In the third step, $OH^\bullet$ free-radical formed on photo- and thermocatalyst surfaces is an extremely powerful oxidizing agent. It attacks organic groups of the pollutant and undergoes various reactions to convert the organic pollutant into non-toxic and non-hazardous forms or completely degrade into the CO_2 and H_2O as presented in the following equation [148]:

$$OH^\bullet + Organic - pollutant \rightarrow Intermediates \rightarrow CO_2 + H_2O \tag{2.6}$$

However, the photo- and thermogenerated electron/hole pairs exhibit a strong tendency to recombine, which influences the photo- and thermocatalysis efficiency. Thus, the recombination of photo- and thermogenerated charge carriers should be minimized or controlled to facilitate photo- and thermocatalytic reactions. The photo- and thermocatalytic degradation efficiencies of organic pollutants for wastewater remediation are affected by the operating conditions such as the type and nature of photo- and thermocatalyst, organic pollutants, pH, and temperature of the reaction medium, light source, and intensity, and solvent nature [148], [150], [151]. Figure 2.2 presents a proposed methyl green photodegradation mechanism on magnetite NPs.

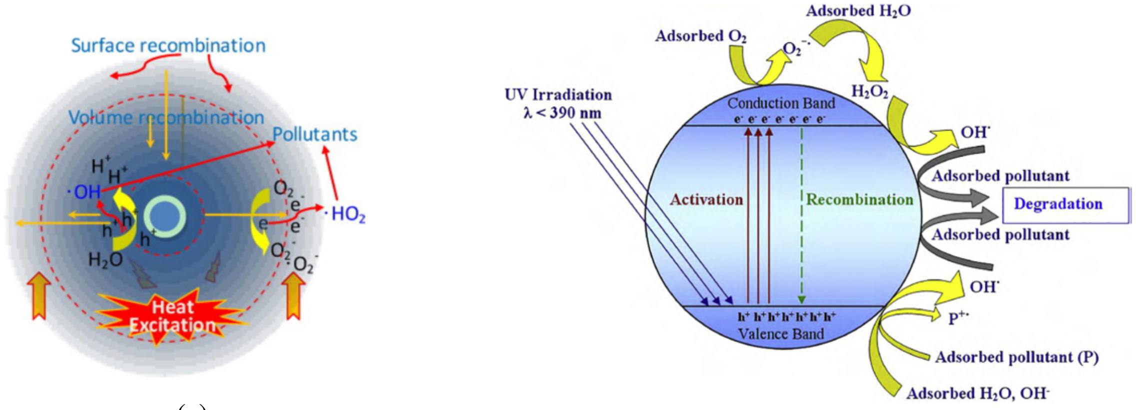

(a)

(b)

Figure 2.1: (a) A schematic illustration of thermocatalysis process mechanism of metal oxides [64], (b) A schematic illustration of photocatalysis process mechanism of metal oxides [77]

2.3.1.1 Dye Adsorption on Nanomaterials under Thermo- and Photocatalysis Processes

Several works studied thermo- and photocatalysis of dyes adsorption on nanomaterials, and they reported the high-efficiency thermo- and photocatalytic activities of nanomaterials. Luo et al. [152] studied the thermocatalysis of methylene blue adsorption on five mixed nano metal oxides by increasing the temperature. They reported that studied adsorbents have an efficient thermocatalytic activity in methylene blue degradation where adsorption yield reached 82.07%. Where Wu et al. [65] studied the thermocatalysis of methylene blue adsorption on magnetite Fe_3O_4@C NPs. They found that the increase of temperature leads to the increase of methylene blue thermodegradation which indicates the high thermocatalytic activity of studied nanomaterial. Other authors [66] studied the thermocatalysis of N719 dye on anatase TiO_2 nanosheets with dominant (*001*) facets and TiO_2 NPs with dominant (*101*) facets. They found that the increase of temperature leads to the increase of N719 dye thermodegradation on both studied nano-adsorbents due to thermocatalytic activities of TiO_2 NPs. Farghali et al. [67] studied the thermocatalysis of methylene blue on multi-walled carbon nanotubes decorated with $CoFe_2O_4$ NPs by increasing temperate. They reported that this nanocomposite showed an efficient thermocatalytic activity.

Furthermore, Ge et al. [68] studied the photocatalysis of methylene blue and methyl orange adsorption on iron oxide anchored to single-wall carbon nanotubes by UV irradiation. They reported that the studied catalyst showed an efficient photocatalytic activity. Elhadj et al. [69] studied

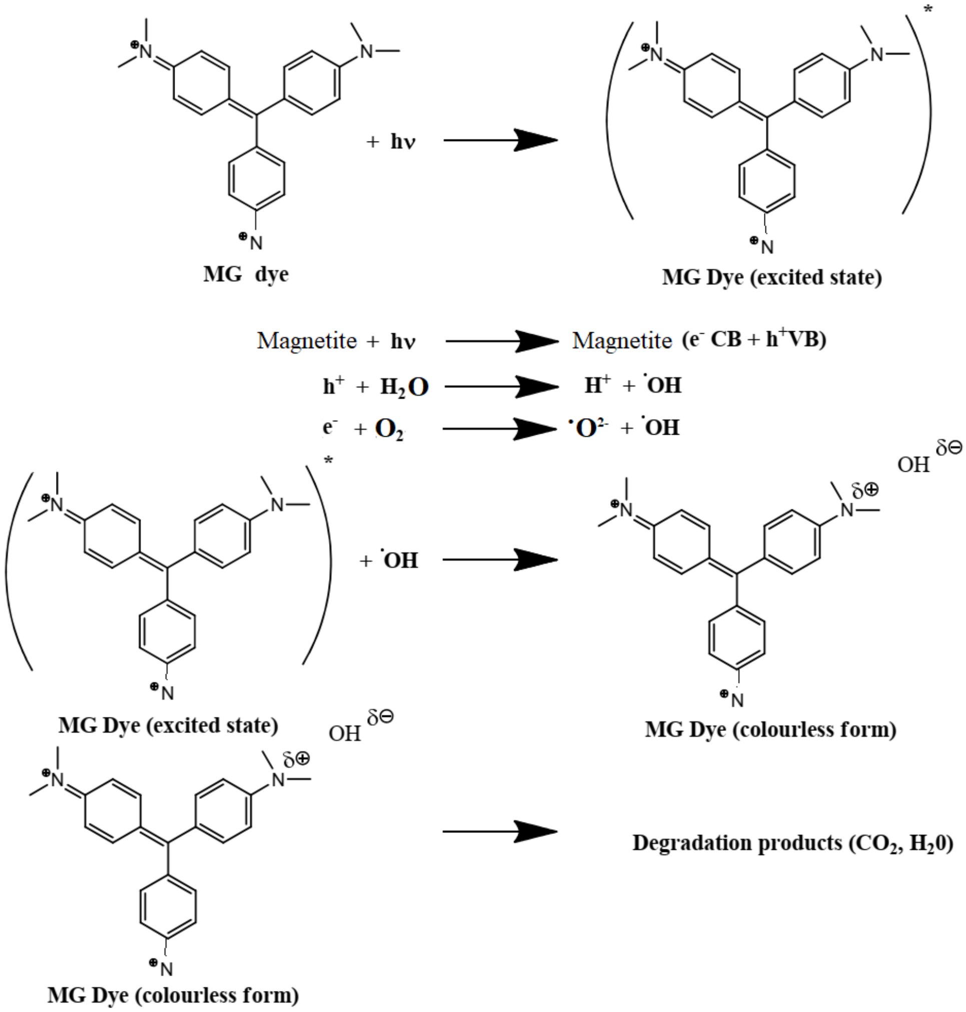

Figure 2.2: Proposed photodegradation mechanism of methyl green on magnetite NPs

the photocatalysis of Basic Red 46 dye adsorption over ZnO NPs under solar irradiation. They reported that ZnO NPs exhibit a high photocatalytic activity. Moreover, Kumar et al. [70] studied the photodegradation of methylene blue (MB), Congo red (CR), and methylene orange (MO) under sunlight irradiation in the presence of greenly synthesised magnetite mediated by Andean blackberry leaf extract. They reported that the presence of those magnetite NPs accelerated the photodegradation of the three dyes due to their high photocatalytic activity. Whereas, Sirdeshpande et al. [71] studied the photodegradation of malachite green under sunlight irradiation in the presence of greenly synthesized magnetite using leaf extract of Calliandra haematocephala. They reported that the presence of those magnetite NPs increased the photodegradation of malachite green. Other authors [72] compared the photocatalytic activity of several composites of titanium dioxide containing magnetite NPs with different morphologies and structures in the photodegradation of Rhodamine.Be by UV irradiation. They reported that the highest dye photodegradation was observed when both spherical and rod-shaped composite structures based on titanium dioxide containing 1 wt% of magnetite NPs were used as a photocatalyst. Jassal et al. [73] studied the thermo- and photodegradation of malachite green (MG) and Eriochrome Black T (EBT) dyes on greenly synthesised potassium zinc hexacyanoferrate nanocubes. They found that this adsorbent acted as a photocatalyst, not a thermocatalyst.

Several parameters can impact photo- and thermocatalysis processes such as solution pH, adsorbent concentration, dye concentration, solution ionic strength, temperature [74]–[76], gap energy, recombination of electron/hole pairs lifetime [80], [81], adsorbent type [82], [83], light source and time of light exposition [82]. Ullah et al. [80] reported that Mn^{2+} dopant in the ZnO NPs decreased the recombination of the electron/hole pairs lifetime which enhanced the photocatalytic activity efficiency for the removal of dyes. Where Rafaie et al. [81] studied the photocatalytic properties of ZnO NPs microstructures decorated with Ag NPs for degradation of methylene blue under UV irradiation. They reported that the presence of Ag NPs played the role of electron sinks and trapped the photogenerated electrons, which slowed the electron-hole pair lifetime. As a result, ZnO-Ag nanostructure exhibited higher photocatalytic activity for the degradation of MB dye.

2.4 Conclusion

In this chapter, a background on dye adsorption process types was presented. Moreover, an overall discussion of the state of the art on the effect of several factors on dyes adsorption has been done. Dyes preferential adsorption on nanomaterials is also presented with a discussion of several results. This chapter also presented thermo- and photocatalysis processes definition and mechanisms. Additionally, an overall discussion of state of art on dyes adsorption on nanomaterials under thermo- and photocatalysis and the effect of several factors on thermo- and photocatalysis has been discussed.

The presented chapter would be useful to express the second contribution to present in the chapter 4, in which the effect of plant extract on preferential and enhanced MG adsorption under thermo- and photocatalysis will be presented.

PART II

Contributions

Chapter 3

Plant Extract FRAP Effect on Cation Vacancies Formation in Greenly Synthesized Wüstite (Fe_xO) NPs: a New Contribution

3.1 Introduction

Iron oxide nanoparticles (NPs) exist under several forms such as Fe (II) oxide (wüstite Fe_xO), Fe (II, III) oxide (magnetite, Fe_3O_4), Fe (III) oxide (hematite, $\alpha - Fe_2O_3$ and maghemite, $\gamma - Fe_2O_3$) [1], [2]. Unlike other iron oxides, stoichiometric wüstite NPs, FeO, cannot exist as a stable phase at low pressures or at pressures exceeding 10 MPas [4]. The nonstoichiometric wüstite is denoted Fe_xO where x represents iron composition and $1-x$ represents Fe^{2+} vacancies (defects). It always contains more oxygen than that in the stoichiometric wüstite ($O/Fe > 1$). The nonstoichiometric is accommodated by oxidation of proportion of iron cations and formation of cation vacancies.

A stable cation-deficient phase of Fe_xO with iron x ranging from 0.83 to 0.96 exists at 0.1 MPas pressure and temperature greater than 567 $°C$ [25]. This phase disproportionates to Fe metal and Fe_3O_4 when cooled slowly to temperatures lower than 567 $°C$. If however Fe_xO is rapidly quenched the nonstoichiometric form can be obtained as a metastable phase at ambient temperature [25]. Wüstite will be oxidized completely to Fe_3O_4 in about 4 months in ambient conditions [26].

The structure of wüstite is a defective form of an ideal NaCl-type lattice where oxygen ions form an fcc lattice and Fe^{2+} cations are located on the interstitial sites [27].

It is known that Fe^{2+} deficiency is attributed to the formation of neutral vacancies on cation sublattices together with Fe^{3+} cations which provide charge compensation with the aim of preserving the total crystal electroneutrality of Fe_xO. Thus some of the Fe^{2+} cations liberate other electrons and become Fe^{3+} cations. This means that for a given value of x (iron composition in

Fe_xO), there are $2(1-x)Fe^{3+}$ and $(1-3(1-x))Fe^{2+}$ cations. This iron deficiency leads to the formation of $1-x$ cation vacancies. These vacancies are partly located as Frenkel defects on interstitial tetrahedral sites [28]. The detailed representative structure of Fe_xO is thus [29]: $Fe^{2+}_{1-3(1-x)}Fe^{3+}_{2(1-x)}\square_{1-x}O^{2-}$ where $\square$ represents cation vacancies. The formation of cation vacancies is responsible for charge redistribution and appearance of Fe^{3+} cations in the octahedral and tetrahedral (interstitial) sites [28], [30].

The study of cation vacancies' effect on Fe_xO properties makes the subject of extensive experimental studies and theoretical considerations. It is reported that cation vacancies have an effect on wüstite formation reaction thermodynamic [31], [32], structural [33], [34], physical [29], electrical, and optical properties [35]–[38]. Wdowik et al. [39] reported that cation vacancies have an effect on electronic and dynamical properties of FeO. Zhang et al. [40] found that iron defects have a strong effect on the elastic properties of wüstite. Those defects on interstitial tetrahedral sites make physical and chemical properties of wüstite NPs distinguishable [1], [36], [41]. Seeing that cation vacancies directly affect wüstite properties and consequently their applications; finding a process that controls cation vacancies in wüstite NPs is still needed. So, the work of this chapter looks for parameters that impact cation vacancies in the case of green synthesis namely the sort of four plants extracts.

The mediating plant extract used in the green synthesis of iron oxide NPs is one of the parameters that may influence iron oxide NP morphologies and hence the reactivity of their surfaces [42]. Makarov et al. [43] reported that pH of plant extract affects the stability of magnetite NPs. In [44] authors found that plant extract concentration has an effect on NPs morphology while authors of [45] found that plant type impacts NPs morphology. According to [46]–[50], one can conclude that plant extract type may impact iron composition within wüstite because they used Medicago sativa (alfalfa), Terminalia chebula dry fruit pericarp, eucalyptus tereticornis, Cymbopogon citratus, and Avicennia marina extracts, respectively, and they found different iron composition in wüstite. Such mediating plant extract effects need more focus on the properties that impact synthesis iron NPs.

In this chapter, the effect of FRAP power of mediating aqueous plant extract on cation vacancies formation (Fe^{2+} defects) within greenly synthesized Fe_xO NPs has been studied. To the best of our knowledge, there is no study in the literature that dealt with this topic. Since FRAP power reduces Fe^{3+} to Fe^{2+}, four plant extracts are used as reducing agents and $FeCl_3$ as a precursor to greenly synthesize four Fe_xO samples, so as to study how variation in FRAP impacts the formation of cation vacancies in Fe_xO samples as a novelty contribution. Furthermore, a deep focus on

Fe_xO formation reaction kinetic and the effect of cation vacancies on its thermodynamic were provided. Iron oxide samples are characterized by XRD, SEM, FTIR-ATR, and UV-Vis techniques. The used plants are Artemisia herba-alba (L), Matricaria Pubescens.(L), Juniperus Phoenicia.(L), and Rosemarinus Officinalis.(L) and the synthesized Fe_xO samples from their extracts are respectively denoted in this chapter by $ARM - Fe_xO$, $MAT - Fe_xO$, $JUN - Fe_xO$ and $ROS - Fe_xO$.

The remainder of this chapter is organized as follows. The next Section gives a description of used materials and followed methods during experiments. In Section 3.3, obtained results are presented and discussed by analyzing XRD, SEM, FTIR-ATR, and UV-Vis data. The Section 3.3.5 is then devoted to presenting our investigation on the effect of FRAP power on cation vacancies formation within synthesised Fe_xO. Thermodynamic of wüstite formation is studied in Section 3.3.6. The last Section presents the conclusion.

3.2 Materials and Methods

This section focuses on listing needed materials and used apparatuses. It also provides methods utilized to perform FRAP essay, green synthesis, and characterization of iron oxide NPs.

3.2.1 Materials

Chemicals

Tripyridyltriazine (TPTZ), HCl, acetic acid, sodium acetate, $FeSO_4$, $7H_2O$, and quercetin are purchased from Alpha Asear, France. Iron salt ($FeCl_3$, $6H_2O$) is purchased from Biochem chemopharma Co, Canada. Artemisia herba-alba.(L) (Asteraceae family), Matricaria Pubescens.(L) (Asteraceae family), Juniperus Phoenicia.(L) (Cupressaceae family), Rosemarinus officinalis.(L) (Lamiaceae family) plants, and doubly distilled water.

Apparatuses

XPERT-PRO X-ray diffractometer (RigakuMiniflex 600) with (30 keV, 30 mA) as conditions of X-ray generation and $K\alpha$ radiation of copper $\lambda = 1.54056$ Å. Scanning Electron Microscope (SEM): FEI Quanta 250 with a tungsten filament. Fourier transform infrared spectroscopy (FTIR-ATR): Shimadzu IR-Infinity. UV-Vis spectroscopy: Shimadzu UV-Vis spectrophotometer apparatus Model 1800 operating in the range of $200 - 900$ nm.

3.2.2 Methods

In this section, used methods for plant extracts preparation and their FRAP essay are described. Used protocol in green synthesis of iron oxide NPs and characterization techniques are described as well.

3.2.2.1 Plant Extracts Preparation

The preparation of the aqueous plant extracts dealt with in this study (Artemisia herba-alba.(L), Matricaria Pubescens.(L), Juniperus Phoenicia.(L), and Rosemarinus officinalis.(L) is described here. Firstly, we well washed the plants with doubly distilled water. After being dried, they are ground into fine powders. Afterward, 30 g of each fine powder of plants are mixed with 540 ml of doubly distilled water. To well extracting the antioxidant substances, the mixtures are stirred continually for 24 h with a stirrer at ambient temperature. Next, the extracts are passed through two layers of muslin and the liquids are then passed through 0.22 μm filters (Millipore) to be used in later NPs synthesis reactions.

3.2.2.2 Ferric Reducing Antioxidant Potential Essay

To measure the ferric reducing potential of plant extracts, we used the Ferric Reducing Antioxidant Potential assay described in [153]. This method is based on the reduction of a colorless ferric complex (Fe^{3+}-tripyridyltriazine) to a blue-colored ferrous complex (Fe^{2+}-tripyridyltriazine) by the action of electron-donating antioxidants. The reduction is therefore monitored by measuring the change of absorbance at 593 nm.

The working FRAP reagent is freshly prepared by mixing 2.5 ml of a mixture of 10 mM tripyridyltriazine (TPTZ) and 40 mM HCl with 2.5 ml of 20 mM $FeCl_3$ and 25 ml of 0.3 M acetate buffer (pH 3.6). Then, 0.2 ml of each aqueous plant extract is mixed with 1.8 ml of the prepared FRAP reagent. The absorbance of sample solutions is measured at 593 nm using a UV-Vis spectrophotometer. To make sure of results, analyses are achieved in duplicate. The results are expressed as μ M of Fe(II), using linear calibration obtained with different concentrations of aqueous $FeSO_4 \times 7H_2O$ ranging from $100 to 700$ mM. where quercetin is used as positive control. The obtained calibration curve equation of $FeSO_4 \times 7H_2O$ is $Y = 6.908X$ with $R^2 = 0.998$.

3.2.2.3 Green Synthesis and Characterisation of Iron Oxide NPs

For the green synthesis of iron oxide NPs, we followed the protocol as follows: $200\ ml$ of plant aqueous extract is mixed with $100\ ml$ of aqueous iron chloride salt solution with a concentration of $0.4\ M$. The mixtures are stirred continually for $1h$ at reaction temperature $70\ °C$. They are then dried in the drying oven.

The phases of the obtained products are identified by XRD in the 2θ range of $10-80°$. FTIR-ATR provides additional confirmation on the presence of the oxide phase as well as information on the sample's crystallinity. The surface investigation is done with the scanning electron microscope (SEM). UV-Vis spectroscopy is a technique widely used to examine the optical properties such as the band gap energy of the synthesised products (Total Attenuated Reflectivity). All measurements are achieved at ambient conditions of temperature and pressure.

3.3 Results and Discussion

This Section presents and analyses obtained results from XRD, SEM, FTIR-ATR, and UV-Vis data. Section 3.3.5 is in particular devoted to presenting our investigation on the effect of plant extract FRAP power on cation vacancies formation within synthesised Fe_xO NPs. Thermodynamic of wüstite formation reaction is also studied in section 3.3.6.

3.3.1 XRD Analysis of Iron Oxide NPs

Through the analysis of XRD patterns, shown in Figure 3.1, it is found that all synthesized samples have crystalline structures. Bragg reflection peaks at around $2\theta° = 36.24\ °$, $42.09\ °$ and $61.04\ °$ are present in all patterns. Those peaks are consistent and much well with wüstite NPs phase corresponding to Miller indices (*111*, *200*, and *220* respectively) indicated in standard diffraction of cubic wüstite powder (JCPDF No 01-074-1880), except for minor differences in intensities and a shift in $2\theta°$ values arising from octahedral vacancies and tetrahedral ferric iron cations. The structure of wüstite having the above-mentioned code reference (JCPDF file 01-74-1880 [1]) is cubic with Fm3m face-centered cubic (fcc) and lattice parameter $a = 4.2902$ Å.

The most useful information to be extracted from XRD patterns, additionally to the grain size, is the lattice parameter of Fe_xO samples. For cubic crystal cells, it is calculated using the following

---

[1] See Appendix A

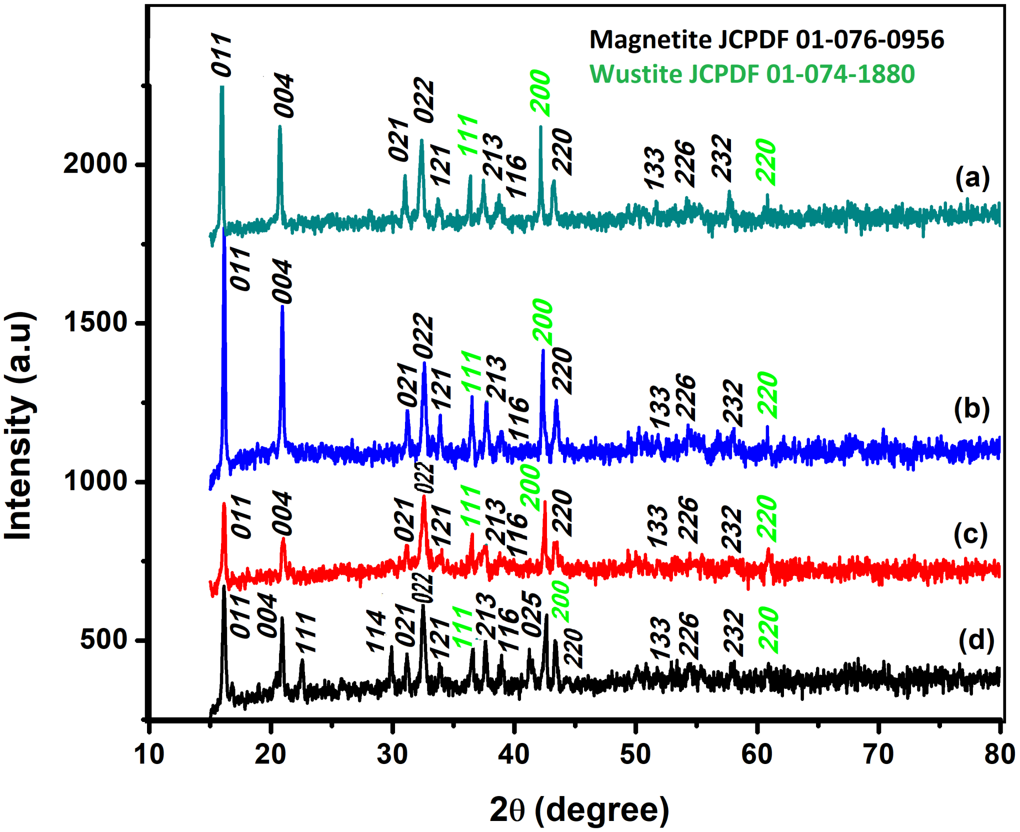

Figure 3.1: XRD patterns of (a) $ROS - Fe_{0.9060}O/Fe_3O_4$, (b) $JUN - Fe_{0.8720}O/Fe_3O_4$, (c) $MAT - Fe_{0.8560}O/Fe_3O_4$, and (d) $ARM - Fe_{0.8319}O/Fe_3O_4$ NPs, JCPDF file 01-074-1880 and Fe_3O_4 NPs, JCPDF file 01-076-0956

equation [154]:

$$\frac{1}{d_{hkl}^2} = \frac{1}{a^2}h^2 + k^2 + l^2 \tag{3.1}$$

where, d_{hkl} and (*hkl*) are the inter-planer distance and Miller indices, respectively. Fe^{2+} composition (x) in Fe_xO samples is related to lattice parameter *a* through McCammon equation [31] as follow:

$$a = 3.856 + 0.478x \tag{3.2}$$

The lattice parameters (a), Fe^{2+} composition (x) and defects $(1 - x)$ within Fe_XO NPs are calculated based on their XRD (*200*) peaks around $2\theta°= 42$ ° and presented in Table 3.1.

Sample Fe_xO	$2\theta°$	d (Å)	a (Å)	x	$1-x$	D_{AG} (nm)	M (g/mol)
JUN	42.28	2.13640	4.2729	0.8720	0.1280	29.874	64.6950
MAT	42.43	2.13259	4.2652	0.8560	0.1440	24.080	63.8047
ROS	42.20	2.14455	4.2891	0.9060	0.0940	36.074	66.5993
ARM	42.52	2.12675	4.2535	0.8319	0.1681	20.640	62.4401

Table 3.1: Crystallite data ($2\theta°$, *hkl=200*, d-spacing, lattice parameter a), Fe^{2+} composition (x), Fe^{2+} defects (1-x), D_{AG} (average grain diameter), and M (molar mass) of $ROS - Fe_{0.9060}O$, $JUN - Fe_{0.8720}O$, $MAT - Fe_{0.8560}O$, and $ARM - Fe_{0.8319}O$ samples

Table 3.1 shows that Fe^{2+} composition (x) in $ROS - Fe_xO$, $JUN - Fe_xO$, $MAT - Fe_xO$, and $ARM - Fe_xO$ are 0.9060, 0.8720, 0.8560 and 0.8319, respectively. The corresponding Fe^{2+} defects in cubic crystal cells ($1-x$) are 0.0940, 0.1280, 0.1440 and 0.1681, respectively. Calculated lattice parameters (a) are 4.2891, 4.2729, 4.2652 and 4.2535 Å, respectively.

Furthermore, X-ray diffraction pattern of synthesised iron oxide NPs exhibit Bragg reflection peaks at around $2\theta° = 15.85$ °, 21.19 °, 21.85 °, 30.13 °, 30.62 °, 32.01 °, 34.22 °, 37.52 °, 38.71 °, 40.60 °, 43.20 °, 51.67 °, 54.75 °, and 57.50 °. All Bragg peaks are in agreement with Fe_3O_4 phase corresponding to Miller indices *011*, *004*, *111*, *114*, *021*, *022*, *121*, *213*, *116*, *025*, *220*, *133*, *226* and *232*, respectively, according to standard diffraction of orthorhombic Fe_3O_4 powder (JCPDF file 01-076-0956 [2]).

XRD patterns analysis allows one to deduce the coexistence of both cubic Fe_xO and orthorhombic Fe_3O_4 NP phases. Fe_3O_4 NPs are formed due to the oxidation of wüstite under ambient conditions [25].

The grain size of different wüstite samples are calculated from XRD patterns using Scherrer's equation [155]:

$$D = \frac{0.9\lambda}{\beta \cos\theta} \tag{3.3}$$

where D, β, λ, and θ are the crystallite size, the full width at half-maximum (FWHM) of the most intense diffraction peak, the X-ray wavelength (1.54056 Å), and Bragg angle, respectively.

The minimum dislocation density σ is calculated using Williamson and Smallman's equation 3.4:

$$\sigma = \frac{n}{D^2} \tag{3.4}$$

---

[2] See Appendix B

where n is a factor equals unity giving minimum dislocation density and D is the grain size [156].

Table 3.1 shows that $ROS - Fe_{0.9060}O$, $JUN - Fe_{0.8720}O$, $MAT - Fe_{0.8560}O$, and $ARM - Fe_{0.8319}O$ NPs exhibit a grain sizes of 36.07, 29.87, 24.08, and 20.64 nm, respectively. The corresponding minimum dislocation densities are: $7.6843.10^{13}$, $1.1205.10^{14}$, $1.7245.10^{14}$, and $2.3473.10^{14}$ $lines/m^2$, respectively. The results show that the increase in iron composition leads to an increase in grain size and hence a decrease in minimum dislocation density.

3.3.2 SEM Images of Iron Oxide NPs

SEM images of synthesized iron oxide NP samples are presented in Figure 3.2. It is clearly shown that, in general, the NPs are more depending on the plant extract. Different irregular shapes are observed in all samples as rocks shape. For synthesized $ROS - Fe_{0.9060}O/Fe_3O_4$ NPs it is clear that a few agglomerations like dried cotton are present with rocks lower than 5 μm (Figure 3.2a). For synthesized $JUN - Fe_{0.8720}O/Fe_3O_4$ NPs, like mountains with bigger rocks having dimensions more than 6 μm are present, as shown in Figure 3.2b. Whereas for the synthesized $MAT - Fe_{0.8560}O/Fe_3O_4$ NPs a decrease in the dimension of the like mountains with more adherence of its structure is observed (Figure 3.2c). Finally, $ARM - Fe_{0.8319}O/Fe_3O_4$ NPs SEM image contains sometimes big structured single crystal having dimension more than 14 μm as mentioned in Figure 3.2d.

3.3.3 FTIR-ATR Spectroscopy Analysis

To indicate the biomolecules responsible for the reduction of the iron precursor, comparisons of FTIR spectra of residual solutions after iron oxide NPs synthesis with those of their as-prepared aqueous plant extracts were carried out. FTIR spectra were recorded between 1500 and 4000 cm^{-1} are presented in Figure 3.3.

As can be seen, the vibrational stretching of the OH polyphenolic group of plant extracts which is measured before and after the NPs synthesis reveals a huge decrease. The range 3500–3000 cm^{-1} indicates the vibrational stretching of the OH polyphenolic group of Artemisia herba-alba.(L), Matricaria Pubescens.(L), Juniperus Phoenicia.(L), and Rosemarinus officinalis.(L) plant extracts with an intensive band at 3288.26, 3293.27, 3307.97, and 3287.03 cm^{-1}, respectively. For residual solution after iron oxide NPs synthesis, those bands undergo a shift to 3174.93, 3247.94, 3187.25, and 3179.74 cm^{-1}, respectively, upon interaction with iron salt. Also, FTIR spectra of the four

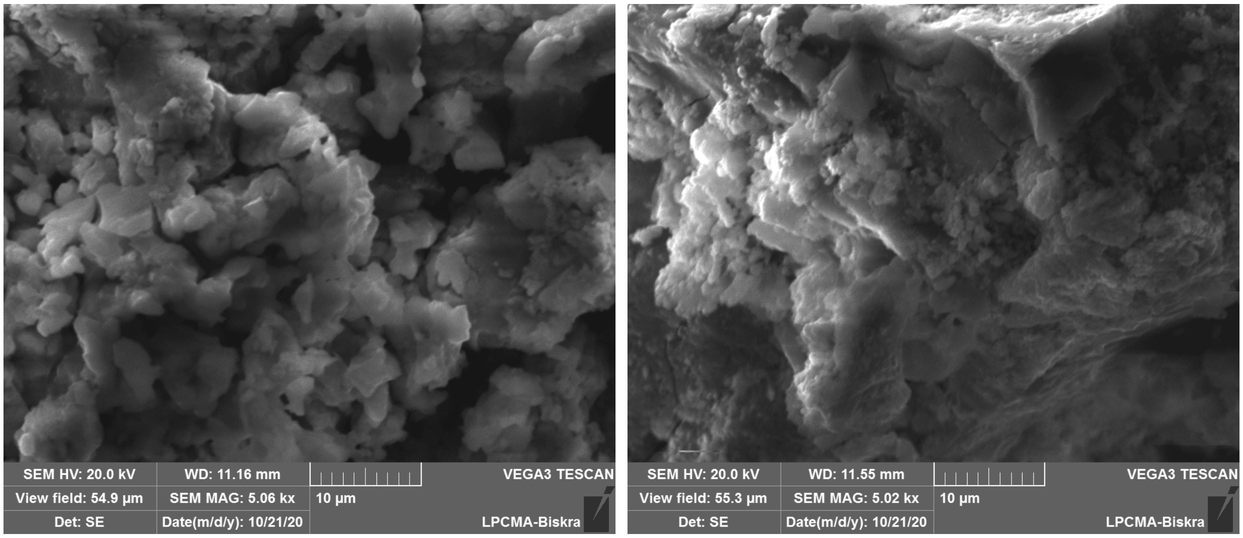

(a) $ROS - Fe_{0.9060}O/Fe_3O_4$

(b) $JUN - Fe_{0.8720}O/Fe_3O_4$

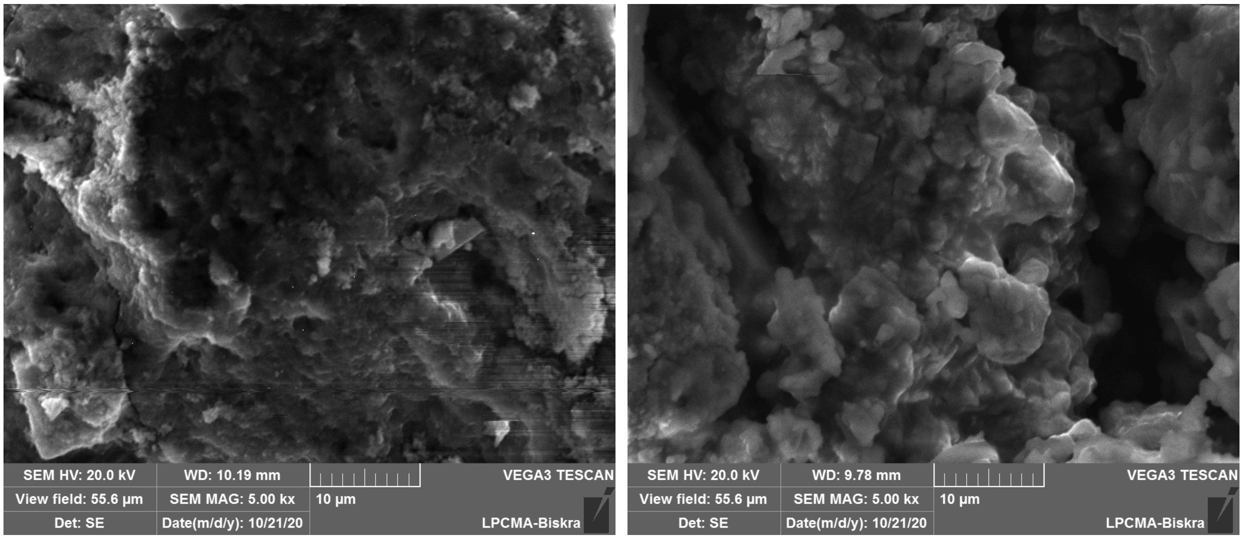

(c) $MAT - Fe_{0.8560}O/Fe_3O_4$

(d) $ARM - Fe_{0.8319}O/Fe_3O_4$

Figure 3.2: SEM micrographes of synthesized Fe_xO/Fe_3O_4 NP samples

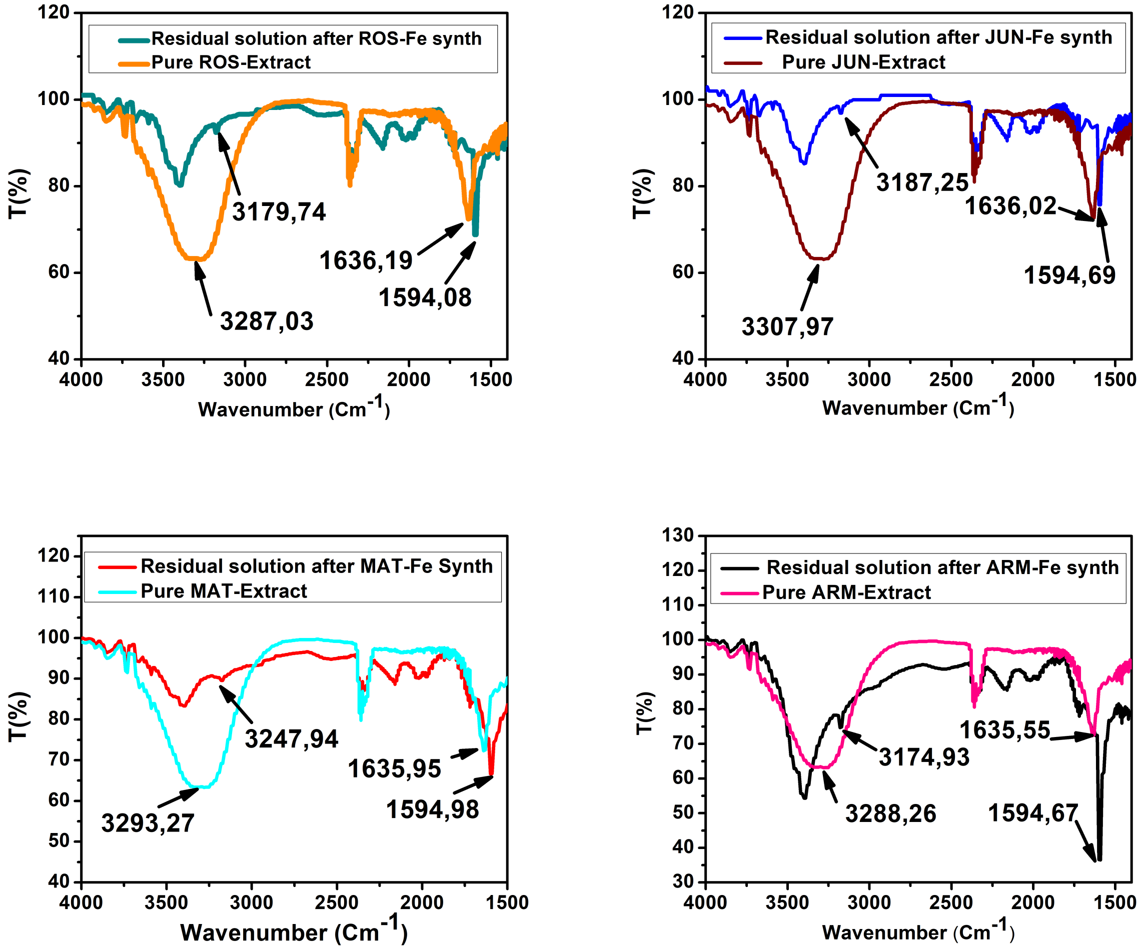

Figure 3.3: Comparisons of FTIR spectra of aqueous extracts before their use and after synthesizing iron oxide NPs for each extract

plant extracts cited above exhibit bands around 1635.55, 1635.95, 1636.02 and 1636.19 cm^{-1}, respectively. These bands may be attributed to the stretching vibration of $C = C$ and $C = O$ groups or to the aromatic ring deformation [47]. The reduction of $FeCl_3$ into iron oxide NPs caused a shift of these bands to 1595.60, 1594.98, 1594.69, and 1594.08 cm^{-1} respectively. This indicates that during the formation of iron oxide NPs, there is a weakness in the OH group and/or $C = C$ and $C = O$ groups -in residual solutions- which become less overlapped and leads to a feeble bands absorption with such shifts of their wavenumbers as seen in Figure 3.3.

FTIR spectra of synthesised iron oxide NP samples recorded between 500 and 1500 cm^{-1} are presented in Figure 3.4. $ROS - Fe_{0.9060}O$, $JUN - Fe_{0.8720}O$, $MAT - Fe_{0.8560}O$, and $ARM - Fe_{0.8319}O$ FTIR spectra exhibit peaks at around 556.80, 535.04, 528.23 and 509.75 cm^{-1}, respectively. These peaks are corresponding to the $Fe - O$ stretching band of wüstite NP. These results are in accordance with Bowen et al. [36] results. They reported that $Fe_{0.93}O$ NPs exhibit a peak at 570 cm^{-1}. It is known that the decrease in iron composition within wüstite shifts to weaker peak intensity [157].

Thus, the fact that Fe^{2+} composition in $ROS - Fe_{0.9060}O$ is close to that in $Fe_{0.93}O$ sample is what makes their peaks close (556.80 and 570 cm^{-1} respectively). Figure 3.4 shows that all IR scepters exhibit peaks at around 581.63 [158], 599.05, [159] and 668.55 cm^{-1} [160] which correspond to the $Fe - O$ stretching band of Fe_3O_4 NPs.

3.3.4 UV-Vis Spectroscopy Analysis

The optical absorbance spectra of all Fe_xO/Fe_3O_4 NP samples are measured in the wavelength range of $200 - 900$ nm. The band gap energies of Fe_xO/Fe_3O_4 samples are then deduced from those spectra. The band gap E_g and the optical absorption coefficient (α) of semiconductor are related through the known following equation [161]:

$$\alpha h\nu = A(h\nu - E_g)^n \tag{3.5}$$

where α is the linear absorption coefficient of the material, $h\nu$ is the photon energy, A is a proportionality constant, and the exponent n depends on the nature of electronic transition; it is equal to $1/2$ for direct allowed transition and 2 for indirect allowed transition.

E_g of the direct transition of all samples were obtained from plotting $(\alpha h\nu)^2$ as a function of $\alpha h\nu$ by the extrapolation of the linear portion of the curve (Figure 3.5). However, E_g of the

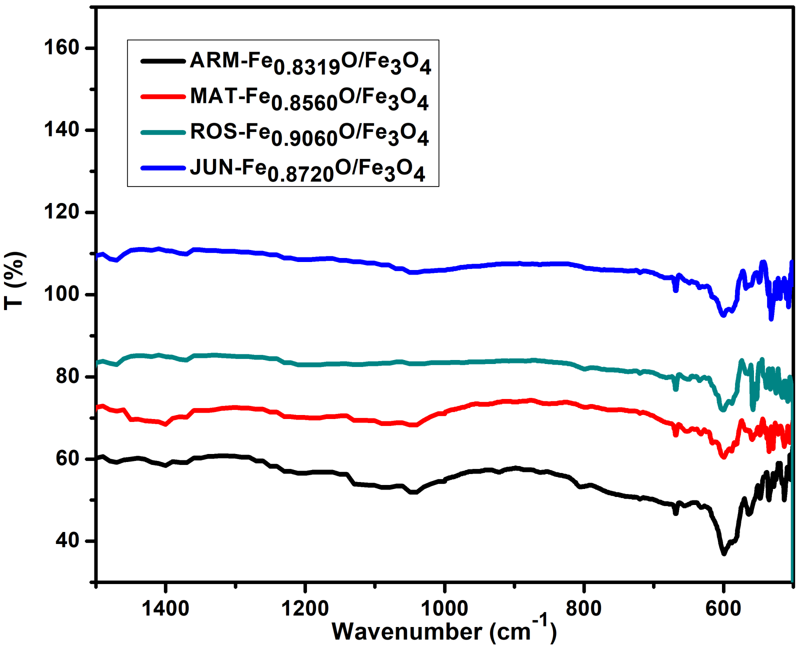

(a)

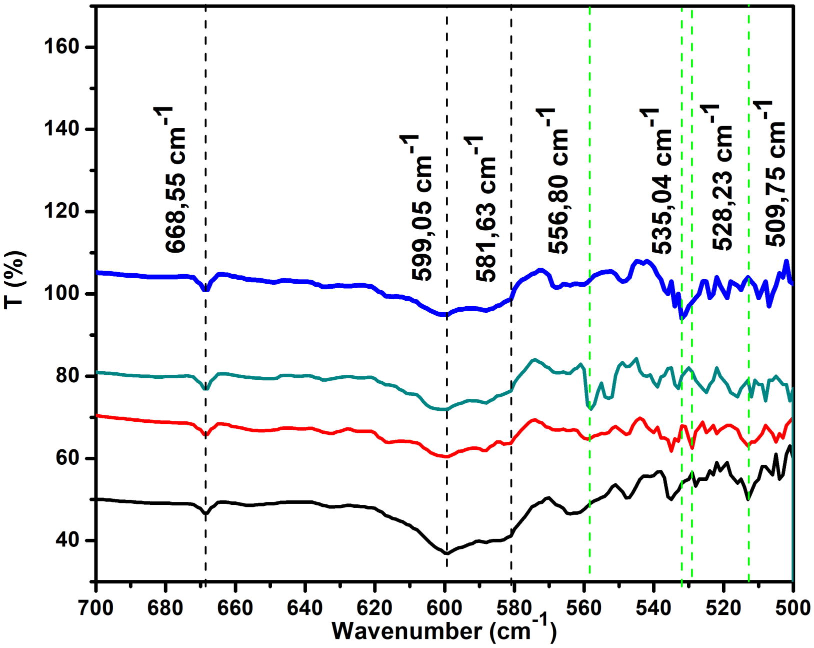

(b)

Figure 3.4: (a) IR spectra of synthesized $ROS - Fe_{0.9060}O/Fe_3O_4$, $JUN - Fe_{0.8720}O/Fe_3O_4$, $MAT - Fe_{0.8560}O/Fe_3O_4$, and $ARM - Fe_{0.8319}O/Fe_3O_4$ NP samples, (b) FT-IR spectra Illustrative at range 500 to 700 cm^{-1}, focuses on Fe-O bonds, of synthesized wüstite NPs

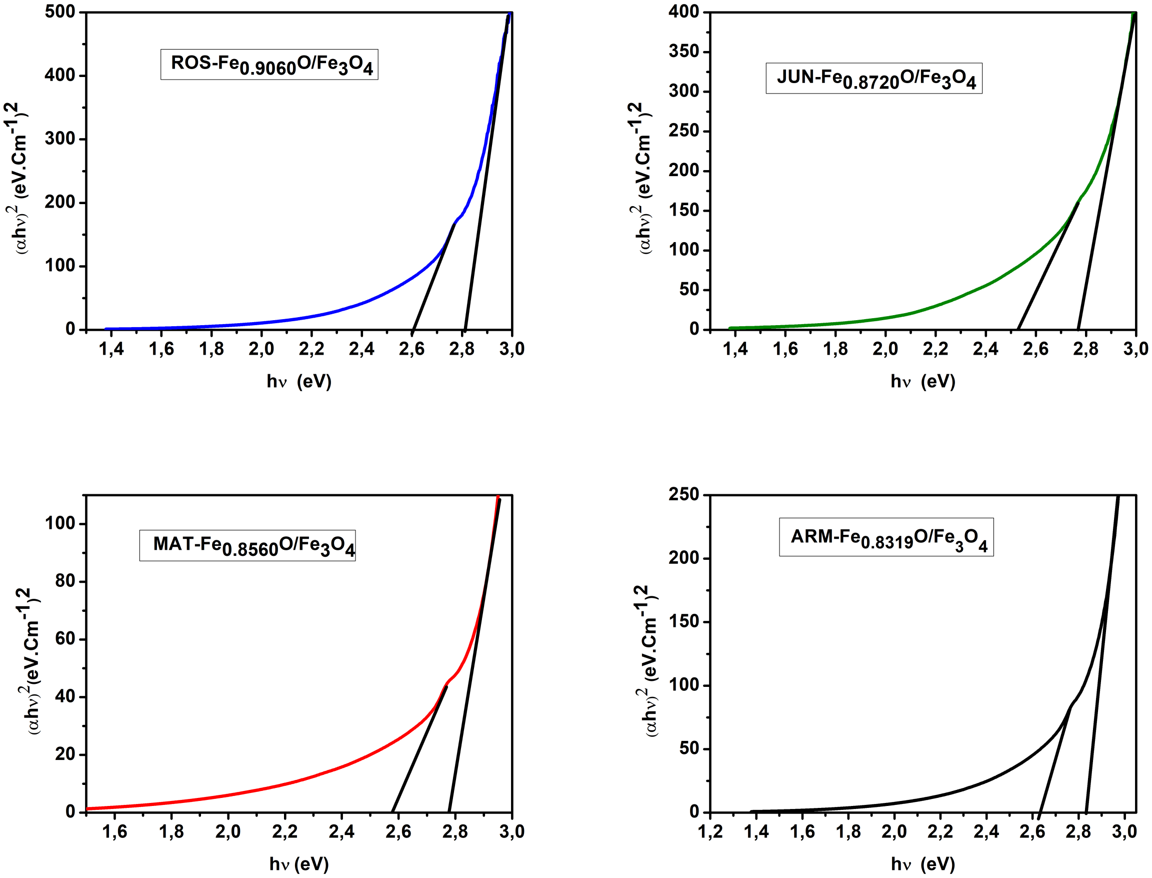

Figure 3.5: Plots of $(\alpha h\nu)^2$ versus $(\alpha h\nu)$ for direct transition of synthesized Fe_xO/Fe_3O_4 NP samples sonicated in acetone during 15 minutes

Sample Extract/Fe_xO	FRAP ($mmolFe^{2+}/g$)	Fe^{2+} defects $1-x$	O/Fe	D_{AG} (nm)
ROS	6.970	0.0940	1.103	36.07
JUN	5.066	0.1280	1.146	29.87
MAT	2.530	0.1440	1.168	24.08
ARM	1.622	0.1681	1.202	20.63

Table 3.2: FRAP of mediating plant aqueous extracts values and Fe^{2+} defects within wüstite samples

indirect transition of all samples were obtained from plotting $(\alpha h\nu)^{1/2}$ as a function of $\alpha h\nu$ by the extrapolation of the linear portion of the curve (3.6). UV-Vis spectra of all samples exhibit two fundamental absorption edges (as shown in Figure 3.5 and Figure 3.6) due to the coexistence of both phases wüstite and Fe_3O_4 NPs. Estimated direct band gap energies of $JUN - Fe_{0.8720}O$, $MAT - Fe_{0.8560}O$, $ROS - Fe_{0.9060}O$, and $ARM - Fe_{0.8319}O$ phases are found to be 2.52, 2.58, 2.61, and 2.62 eV, respectively. Bowen et al. [36] found that gap energy for single-phase Fe_xO with different iron composition ($x = 0.8772$, 0.8928, 0.9174 and 0.9523) is always $E_g = 2.4\ eV$. All band gap energies are close to the above-mentioned direct gap energy. The found minor shifts in band gap energies of wüstite are due to the existence of the second phase of Fe_3O_4.

Estimated indirect band gap energies of $ROS - Fe_{0.9060}O$, $JUN - Fe_{0.8720}O$, $MAT - Fe_{0.8560}O$ and $ARM - Fe_{0.8319}O$ phases are found to be 2.09, 1.99, 2.11 and 1.83 eV, respectively. Schrettle et al. [38] found that the indirect band gap energy of wüstite is E_g = 1 eV. All indirect band gap energies of wüstite are far from mentioned indirect gap energy.

It is clear that the direct gap energy is closer to the theoretical value than the indirect gap energy. The values of all direct band gap energies of wüstite NP samples classify them as semiconductors. The energy band gap of the semiconductors is between 0 and 3 eV [162].

3.3.5 FRAP Effect on Wüstite Defects

To explain our investigation on FRAP effect on wüstite defects, firstly, reaction phases of wüstite NPs formation is described. Then how variation in FRAP of plant extracts impacts iron defects within formed wüstite samples is discussed.

In all experiments, the addition of aqueous plant extract to aqueous $FeCl_3$ changes immediately the color of this later from light brown to dark green which means the reduction of Fe^{3+} to

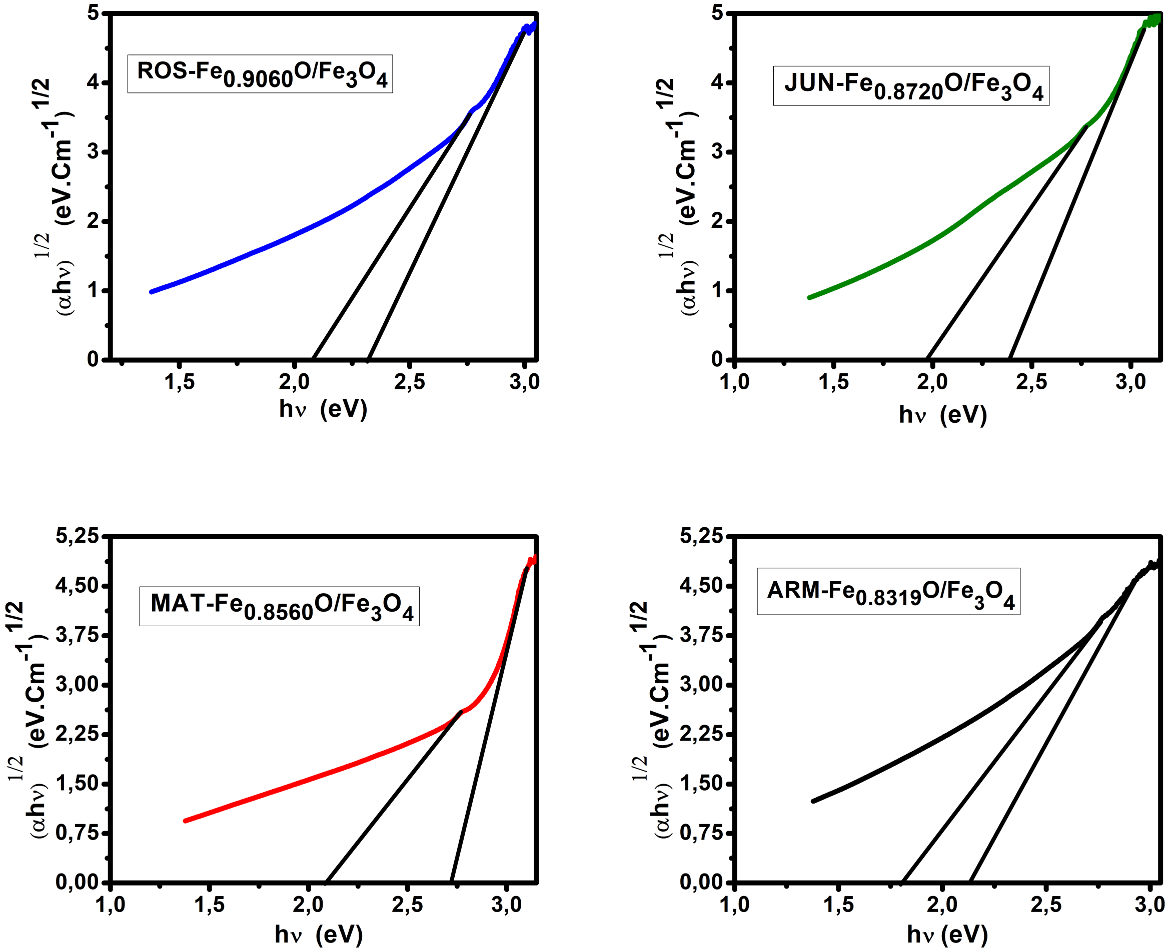

Figure 3.6: Plots of $(\alpha h\nu)^{1/2}$ versus $(\alpha h\nu)$ for indirect transition of synthesized Fe_xO/Fe_3O_4 NP samples sonicated in acetone during 15 minutes

Fe^{2+} (first reaction phase). The FRAP power of the antioxidants substances in the aqueous extract play the role of reductant of Fe^{3+} to Fe^{2+} cations. This allows one to conclude that FRAP of plant extract impacts the amount of Fe^{3+} reduced to Fe^{2+}; an increase in FRAP leads to an increase of Fe^{2+} amount reduced from Fe^{3+}. In the second reaction phase, the dark green color is changed gradually to dark black revealing the formation of wüstite NPs (see Fig 3.7). It is worth noting that, in the conditions of our experiments ($70°C$ and $1\ atm$), wüstite NPs are formed with Fe^{2+} defects as seen in the introduction § 3.

After analyzing XRD data in section 3.3.1, it was found that wüstite samples are formed with different iron defects, according to the used plant extract. Since the amount of oxidized Fe^{2+} is influenced by plant extract FRAP, the effect of FRAP on iron defects is investigated. Table 3.2 and Figure 3.8a show the variation of iron defects with the variation of FRAP for the studied samples. Results show that ROS aqueous extract has the highest FRAP $6.97\ mmolFe^{2+}/g$, and the formed $ROS - Fe_xO$ NPs has the lowest defects value ($1 - x = 0.0940$) with the closest O/Fe ratio to 1 ($O/Fe = 1.103$). On the other side, ARM aqueous extract has the lowest FRAP $1.622\ mmolFe^{2+}/g$, and the formed $ARM - Fe_xO$ NP defects value is the highest one ($1 - x = 0.1681$) with the furthest O/Fe ratio from 1 ($O/Fe = 1.202$). In the same way, the increase in FRAP of plant extract leads to a decrease in defects within Fe_xO samples and hence to a O/Fe ratio closer to 1.

Since high FRAP leads to an excess of Fe^{2+} in the intermediate solution, the oxidation of Fe^{2+} by the antioxidants substances in this medium produces wüstite NPs closer to stoichiometry composition. This decreases the quantity of Fe^{2+} cations liberate electrons and become Fe^{3+} to compensate the total electrical charge of the formed clusters and hence decreases cation vacancies. Such decrease in cation vacancies is confirmed by the increase in grain size of studied samples as shown in Table 3.2. These results are in accordance with the results reported in [163]. Furthermore, Figure 3.8b depicts that grain size increases linearly ($R^2 = 0.9933$) with the increase of FRAP.

Results allow one to conclude that iron defects within Fe_xO NPs are impacted by the FRAP power of plant extract. This leads to report that FRAP of plant extract provides a preconceived idea about the defects within wüstite NPs structure.

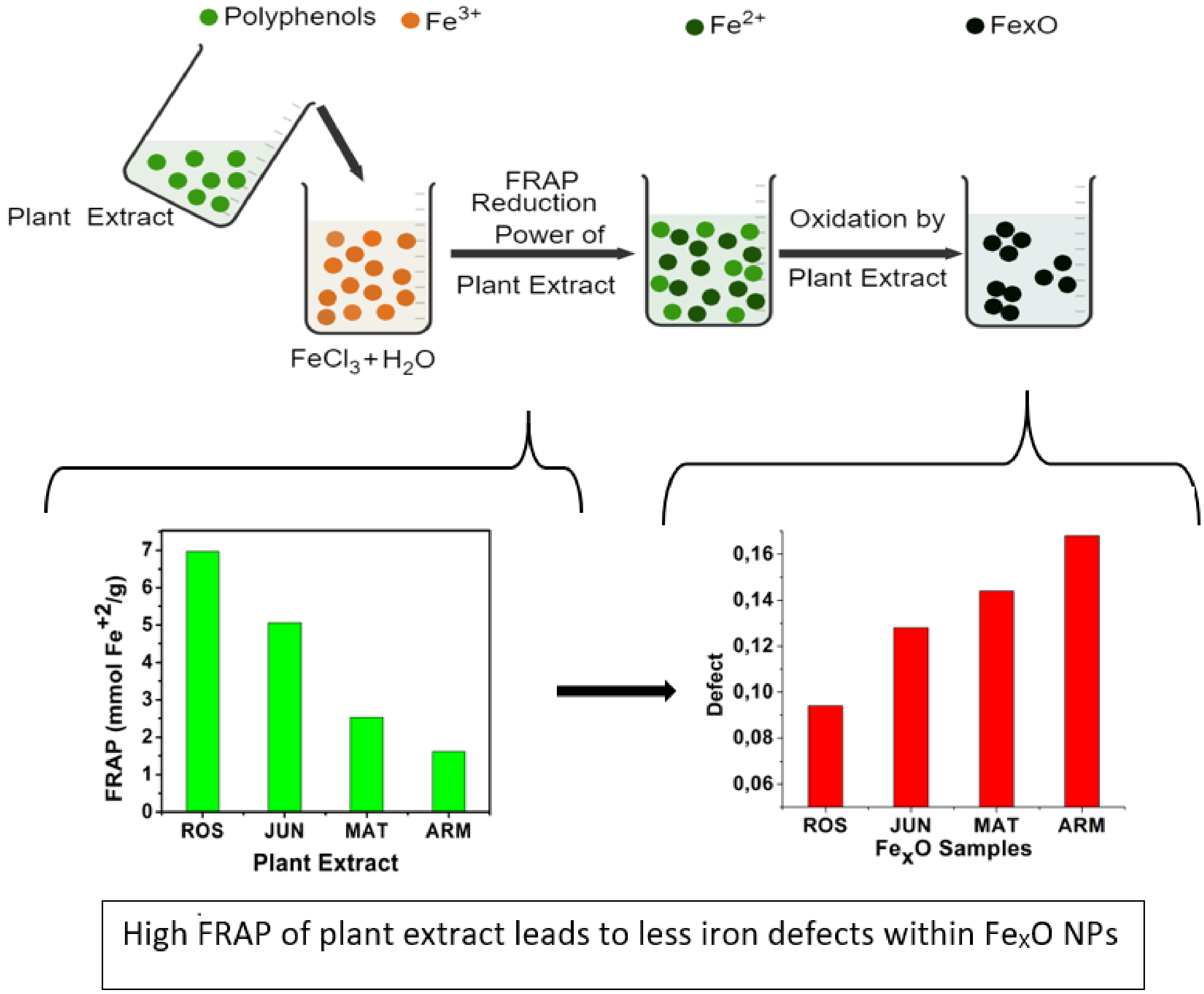

High FRAP of plant extract leads to less iron defects within Fe_xO NPs

Figure 3.7: FRAP of plant aqueous extracts effect on Fe^{2+} defects within wüstite samples

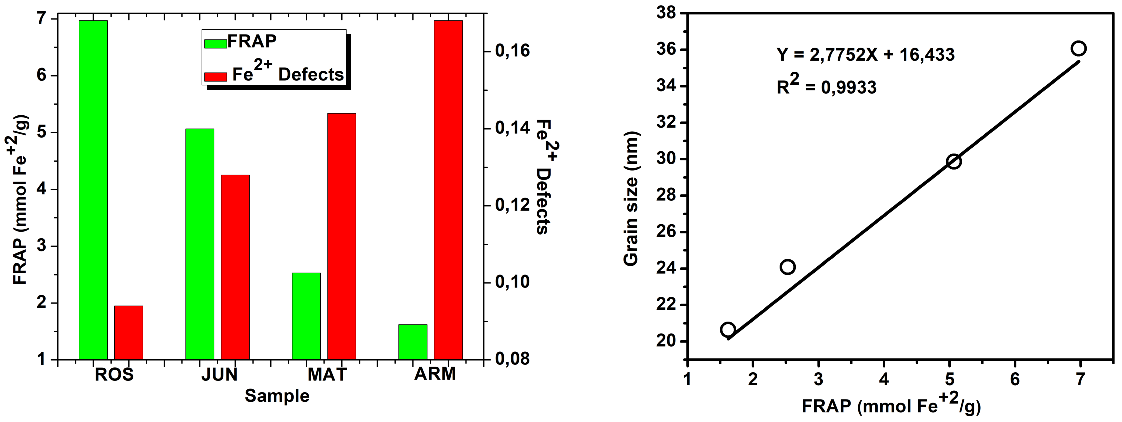

(a) (b)

Figure 3.8: (a) Proportionality of Fe^{2+} defects within Fe_xO samples, (b) Proportionality of grain size of Fe_xO samples with FRAP of their plant extracts

3.3.6 Cation Vacancies Effect on Wüstite Formation Thermodynamic

In all experiments, the addition of aqueous plant extract to aqueous $FeCl_3$ caused an increase in the recipient temperature leading to state that the reaction is exothermic.

The equilibrium reaction of wüstite formation is given by the following equation [31]:

$$Fe + \frac{1}{2x}O_2 \rightarrow \frac{1}{x}Fe_xO \tag{3.6}$$

where Fe_xO is treated as $((FeO)_x(O_2)_{(1-x)/2})$. At atmospheric pressure $(0.1MPa = 1atm)$ the free energy change of wüstite formation reaction is given by following equation:

$$\Delta G^0_{fF_eO}(1, T, x) = \Delta H^0_{fF_eO}(1, T, x) - T\Delta S^0_{fF_eO}(1, T, x) \tag{3.7}$$

where x refers to the equilibrium composition of wüstite at $0.1\ MPas$.

The variation of molal enthalpy $(\Delta H^0_{fF_eO}(x))$ and entropy $(\Delta S^0_{fF_eO}(x))$ of wüstite formation and their relation to equilibrium composition are studied by Giddings et al. [32]. They reported that molal enthalpy and molal entropy are independent of temperature, they depend only on wüstite composition. In order to calculate molal enthalpy and entropy of formation of $ROS - Fe_{0.9060}O$,

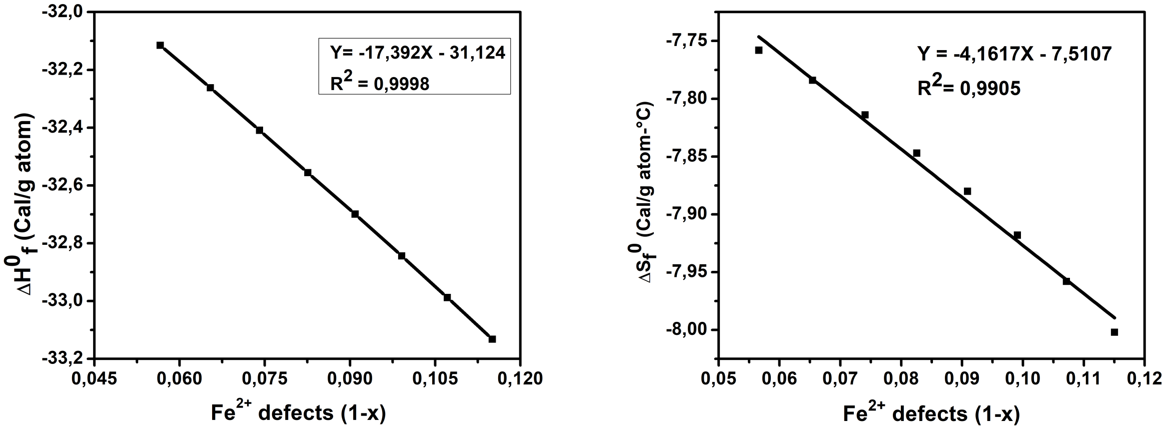

(a) (b)

Figure 3.9: (a) Variation of molal enthalpy of wüstite formation vs. Fe^{2+} defects (b) Variation of molal entropy of wüstite formation vs. Fe^{2+} defects [32]

Fe_xO	Fe^{2+} defects	$\Delta H^0_{fF_eO}(x)$	$\Delta S^0_{fF_eO}(x)$	$\Delta G^0_{fF_eO}(P,T,x)$
		$(cal/g.atm)$	$(cal/g.atm-°C)$	$(cal/g.atm)$
ROS	0.0940	-32.7588	-7.9019	-585.892
JUN	0.1280	-33.3502	-8.0434	-596.388
MAT	0.1440	-33.6284	-8.1099	-601.327
ARM	0.1681	-34.0476	-8.2102	-608.767

Table 3.3: Thermodynamic data of wüstite NPs formation reaction at 0.1 MPas and T=70 $°C$

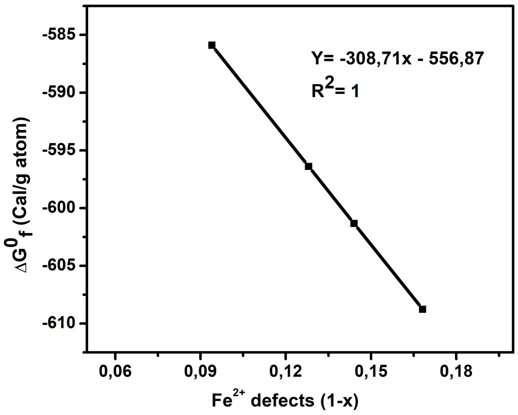

Figure 3.10: Variation of molal free energy of wüstite formation reaction as function of Fe^{2+} defects at 70 $°C$ and 0.1 MPas

$JUN - Fe_{0.8720}O$, $MAT - Fe_{0.8560}O$ and $ARM - Fe_{0.8319}O$ NP samples, thermodynamic data of the previous study are used to plot the variation of molal enthalpy and entropy as a function of Fe^{2+} defects $(1 - x)$, as depicted in Figures 3.9b and 3.9a. Figures show that molal enthalpy and entropy are nearly linear functions of Fe^{2+} defects. Thus, used equations to calculate molal enthalpy and entropy vs. x (Table 3.3) are deduced from linear fitting equations stated in Figures 3.9a and 3.9b ($R^2 = 0.9998$ and 0.9905 respectively).

In order to study the effect of cation vacancies content on the variation of molal free energy of formation ($\Delta G^0_{fF_eO}(x)$) of $ROS - Fe_{0.9060}O$, $JUN - Fe_{0.8720}O$, $MAT - Fe_{0.8560}O$, and $ARM - Fe_{0.8319}O$ at 70 $°C$ is calculated using equation 3.7.

Figure 3.10 illustrates that $\Delta G^0_{fF_eO}(x)$ of Fe_xO NP samples varies linearly with cation vacancies (defect). Results show that molal enthalpy of formation becomes more negative (see Table 3.3) as Fe^{2+} defects increases in Fe_xO NPs. The decrease in molal enthalpy may be a result of defects complexing. We remarked that Fe_xO NPs formation is sufficiently exothermic (as cited in section 3.3.1). This may be occurred to overrule the entropy change which accompanies the reaction. Thus, the free energy becomes more negative as cation vacancies within wüstite becomes more increased which is consistent with results found in [32].

Since FRAP power impacts cation vacancies formation in Fe_xO and cation vacancies impacts formation $\Delta G^0_{fF_eO}(x)$ of Fe_xO then one can conclude that FRAP power impacts $\Delta G^0_{fF_eO}(x)$ of Fe_xO formation. As FRAP decreases as $\Delta G^0_{fF_eO}(x)$ becomes more negative.

3.4 Conclusion

Wüstite Fe_xO NPs have been greenly synthesized using four different aqueous plant extracts as reducing agents and $FeCl_3$ as a precursor. Characterization of synthesized samples shows that wüstite is formed with different iron cation vacancies and grain sizes. For this reason, the effect of FRAP power of aqueous plant extracts on Fe^{2+} vacancies formation within synthesised wüstite NPs has been considered. It is found that iron cation vacancies formation within wüstite NPs are clearly impacted by the FRAP power of plant aqueous extract. Indeed, the increase in the FRAP leads to a decrease in Fe^{2+} defects and consequently an increase in the grain size. This leads to proclaim that FRAP of plant extract provides a preconceived idea about cation vacancies within wüstite NP structure. From thermodynamic study, FRAP power also impacts $\Delta G^0_{fF_eO}(x)$ of Fe_xO formation, where the decrease in FRAP makes $\Delta G^0_{fF_eO}(x)$ more negative. the

Chapter 4

Preferential and enhanced adsorption of methyl green on different greenly synthesized magnetite nanoparticles: investigation of the influence of the mediating plant extract's acidity

4.1 Introduction

Nanomaterials are widely used in the purification of aqueous media [19]–[22]. They allow a rapid thermodynamic equilibrium between adsorbent and adsorbate during the adsorption process and selective removal of pollutants [16], [23], [24]. Adsorption has been extensively studied as a cost-effective process for removing a wide variety of pollutants from aqueous solutions such as dyes [8], [51], [164].

The adsorption ability of iron oxide NPs arises from the intervention of hydroxyl groups during pollutant dissociation [1]. Surface hydroxyl groups, with amphoteric properties, are the functional groups of iron oxide surfaces and they are their chemically reactive entities that behave as the active sites upon the adsorption process. These hydroxyl groups may be singly, doubly, and triply coordinated to Fe atoms having different reactivity. The overall density of these groups depends on both the crystal structure and the extent of development of the different crystal faces [54].

The photo- and thermocatalysts absorb the photons/phonons having energy equal to or more than the band gap energy between the valence band (VB) and conduction band (CB) of the photo- and thermocatalyst. The photons absorption causes the charge separation by exciting electrons from the VB to the CB followed by the generation of positive holes in the VB [149], [152]. These positive holes oxidize adsorbed H_2O molecules and produce hydroxyl radicals ($OH^\bullet$). Whereas, excited electrons reduce the adsorbed O_2 in the CB and produce hydroxyl radicals ($OH^\bullet$). These

$OH^{\bullet}$ radicals attack organic groups of the pollutant and undergo various reactions to convert the organic pollutants into non-toxic and non-hazardous forms or completely degrade them into the CO_2 and H_2O [148], [152].

The photo- and thermogenerated electron/hole pairs exhibit a strong tendency to recombine. Recombination speed is an important factor that influences the photo- and thermocatalysis efficiency. As recombination of photo- and thermogenerated charges is slow as the photo- and thermocatalytic degradation of pollutants is more efficient [165]. Several parameters can impact photo- and thermocatalysis processes such as solution pH, adsorbent concentration, dye concentration, solution ionic strength, temperature [73]–[76], dye structure properties [77], [78], adsorbent particle size [79], gap energy, recombination of electron/hole pair lifetime [80], [81], adsorbent type [82], [83], light source and time of light exposition [82]. Several works studied thermo- and photocatalysis of dyes adsorption on nanomaterials, and they reported the high-efficiency thermo- and photocatalytic activities of nanomaterials. Wu et al. [65] studied the thermocatalysis of methylene blue adsorption on magnetite Fe_3O_4@C NPs. They found that the increase of temperature leads to the increase of methylene blue thermodegradation which indicates the high thermocatalytic activity of studied nanomaterial. Other authors [66] studied the thermocatalysis of N719 dye on anatase TiO_2 nanosheets with dominant *001* facets and TiO_2 NPs with dominant *101* facets. They found that the increase of temperature leads to the increase of N719 dye thermodegradation on both studied nano-adsorbents due to thermocatalytic activities of TiO_2 NPs. Farghali et al. [67] studied the thermocatalysis of methylene blue on multi-walled carbon nanotubes decorated with $CoFe_2O_4$ NPs by increasing temperate. They reported that this nanocomposite showed an efficient thermocatalytic activity.

Furthermore, Ge et al. [68] studied the photocatalysis of methylene blue and methyl orange adsorption on iron oxide anchored to single-wall carbon nanotubes by UV irradiation. They reported that the studied adsorbent showed an efficient photocatalytic activity. Elhadj et al. [69] studied the photocatalysis of Basic Red 46 dye adsorption over ZnO NPs under solar irradiation. They reported that ZnO NPs exhibit a high photocatalytic activity. Moreover, Kumar et al. [70] studied the photodegradation of methylene blue (MB), Congo red (CR), and methylene orange (MO) under sunlight irradiation in the presence of greenly synthesised magnetite mediated by Andean blackberry leaf extract. They reported that the presence of those magnetite NPs accelerated the photodegradation of the three dyes due to their high photocatalytic activity. Whereas, Sirdeshpande et al. [71] studied the photodegradation of malachite green under sunlight irradiation in the presence of greenly synthesized magnetite using leaf extract of Calliandra haematocephala. They reported that the presence of those magnetite NPs increased the photodegradation of the dye.

Other authors [72] compared the photocatalytic activity of several composites of titanium dioxide containing magnetite NPs with different morphologies and structures in the photodegradation of Rhodamine.Be by UV irradiation. They reported that the highest dye photodegradation was observed when both spherical and rod-shaped composite structures based on titanium dioxide containing 1 wt% of magnetite NPs were used as a photocatalyst. Jassal et al. [73] studied the thermo- and photodegradation of malachite green (MG) and Eriochrome Black T (EBT) dyes on greenly synthesised potassium zinc hexacyanoferrate nanocubes. They found that this adsorbent acted as a photocatalyst, not a thermocatalyst.

Several parameters can impact photo- and thermocatalysis processes such as solution pH, adsorbent concentration, dye concentration, solution ionic strength, temperature [74]–[76], adsorbent particle size [79], gap energy, recombination of electron/hole pairs lifetime [80], [81], adsorbent type [82], [83], light source and time of light exposition [82]. Ullah et al. [80] reported that Mn^{2+} dopant in the ZnO NPs decreased the recombination of the electron/hole pairs lifetime which enhanced the photocatalytic activity efficiency for the removal of dyes. Where Rafaie et al. [81] studied the photocatalytic properties of ZnO NPs microstructures decorated with Ag NPs for degradation of methylene blue under UV irradiation. They reported that the presence of Ag NPs played the role of electron sinks and trapped the photogenerated electrons, which slowed the electron-hole pair lifetime. As a result, ZnO-Ag nanostructure exhibited higher photocatalytic activity for the degradation of MB dye.

Several works studied the preferential adsorption of dyes on nano-adsorbents. Saha et al. [16] studied the preferential adsorption of seven different dyes on magnetite NPs. They reported that magnetite surface preferred adsorbing dyes containing higher OH content. Where Xiao et al. [55] studied the preferential adsorption of different cationic and anionic dyes on iron NPs. They reported that iron NPs preferred removing cationic dyes more than anionic dyes. Madrakian et al. [56] studied the preferential adsorption of seven cationic and anionic dyes on magnetite-coated waste tea. They reported that cationic dyes were more adsorbed on the studied nano adsorbent compared to anionic dyes.

Several factors can influence the adsorption such as solution pH [54], solution ionic strength [57], dye concentration [58], magnetite NPs concentration [16], and hydroxyl groups density on adsorbent surface [59]. The impact of changing plants on greenly synthesized metal oxide NPs reactivity in dyes adsorption was studied in several works. Huang et al. [60] studied the effect of three different tea extracts (green, oolong, and black teas) on the properties of iron oxide NPs surface: their reactivities in the removal of methyl green from aqueous solutions. They reported that the plant extract has an effect on the reactivity of iron oxide NPs surface that 81.2%, 75.6%, and 67.1% of methyl green dye has been removal by iron oxide NPs synthesised using the extracts of green, oolong, and black teas, respectively. Likewise, Xiao et al. [55] studied the removal of six cationic and anionic dyes. They reported that greenly synthesised iron NPs using tea extract showed preferential adsorption of cationic dyes from an aqueous solution. Other authors [61] synthesized metal oxide NPs using the extracts of flowers, bark, and leaves of Tecoma stans in order to use them in the removal of Congo red (CR) and crystal violet (CV) dyes. They reported that the adsorbent derived from flower extract gave a better dyes adsorption efficiency than those derived from other extracts. Furthermore, Islam et al. [62] synthesized magnetite NPs using six plant extracts in order to use them in the removal of methyl orange (MO) and crystal violet (CV) dyes. They reported that plant extract had an effect on magnetite NPs surface reactivity in the adsorption, where magnetite Nps synthesized using tea extract showed the highest performance (MO 92.34%, CV 96.1%).

In this chapter, the preferential and enhanced adsorption of MG on four greenly synthesized Fe_3O_4 NP surfaces has been studied by coupling three processes. The preferential adsorption of MG on the four magnetite surfaces in ambient dark conditions first process, followed by adsorption enhancement by thermocatalysis of MG/Fe_3O_4 residual solutions in dark conditions in the second process, and finally the adsorption enhancement by photocatalysis under UV irradiation (365 nm) in ambient conditions of MG/Fe_3O_4 residual solutions after applying thermocatalysis. The focus of this study is on the investigation of the influence of mediating plant extract on greenly synthesised magnetite NP physicochemical characteristics which impact the preferential and enhanced MG adsorption. The studied physicochemical characteristics are functional hydroxyl groups density on magnetite surfaces, grain size, and band gap energy.

The mediating plants in the green synthesis of iron oxide NPs are: Artemisia herba-alba.(L), Matricaria Pubescens.(L), Juniperus Phoenicia.(L), and Rosemarinus officinalis.(L), and the synthesized Fe_3O_4 samples from their extracts are respectively denoted in this chapter by $ARM{-}Fe_3O_4$, $MAT{-}Fe_3O_4$, $JUN{-}Fe_3O_4$ and $ROS{-}Fe_3O_4$. Fe_3O_4 NPs samples were characterized by XRD, SEM, FTIR-ATR, and UV-Vis techniques. In preferential MG adsorption, the pseudo-first-order and pseudo-second-order kinetics of the adsorption as well as the intra-particles diffusion

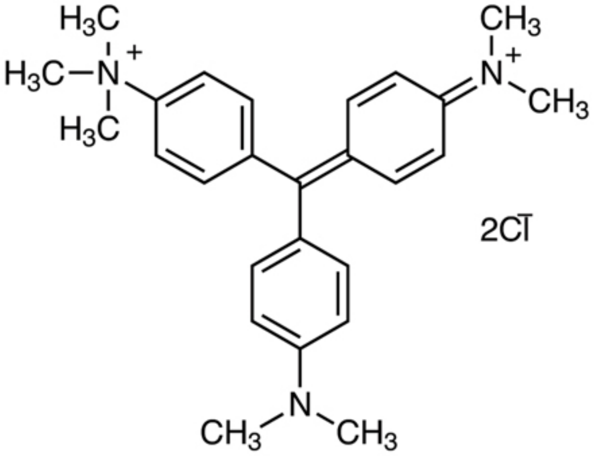

Figure 4.1: Methyl green structure

mechanism have been analyzed. Under thermocatalysis, activated thermodynamic Parameters free energy (ΔG^0), entropy (ΔS^0), enthalpy (ΔH^0), and activation energy (E_a) have been analyzed. Under photocatalysis, the pseudo-first-order has been also analyzed.

4.2 Materials and Methods

This section focuses on listing needed materials and used apparatuses. It also provides methods utilized to perform adsorption experiments and characterization of iron oxide NPs.

4.2.1 Materials

Chemicals

Methyl green dye, $NaCl$ salt, and HCl acid are purchased from Sigma-Aldrich. Greenly synthesised $JUN-Fe_3O_4$, $ROS-Fe_3O_4$, $MAT-Fe_3O_4$ and $ARM-Fe_3O_4$ NP powders using iron salt ($FeCl_3$, $6H_2O$) (purchased from Biochem chemopharma Co, Canada) as a precursor and Artemisia herba-alba.(L) (Asteraceae family), Matricaria Pubescens.(L) (Asteraceae family), Juniperus Phoenicia.(L) (Cupressaceae family), Rosemarinus officinalis.(L) (Lamiaceae family) plants as reducing agents. Fe_3O_4 samples were obtained after 4 months of storage of synthesized iron oxides in ambient conditions. Freshly synthesized samples were both wüstite and magnetite NPs phases [123]. The chemical structure of MG is presented in Figure 4.1.

Apparatuses

An XPERT-PRO X-ray diffractometer (RigakuMiniflex 600) with conditions of 30 keV and 30 mA for X-ray generation and the $K\alpha$ radiation of copper $\lambda = 1.54056$ Åwas used. Fourier transform infrared spectroscopy (FTIR-ATR): Shimadzu IR-Infinity. UV-Vis spectroscopy: Shimadzu UV-Vis spectrophotometer apparatus Model 1800 operating in the range of $200 - 900\ nm$. Instantaneous global UV (direct plus diffuse) was measured with a UV radiometer $\lambda_{Max} = 365\ nm$ VL.215.L, (Ecosystem-Environmental Services, France).

4.2.2 Methods

In this section, used methods for solution preparation are described. Used protocol in adsorption experiments of iron oxide NPs and characterization techniques are described as well.

4.2.2.1 Batch Adsorption Experiments of MG on Magnetite NPs in Dark Ambient Conditions

In the first step, the prepared standard aqueous solutions of MG dye were diluted several times as required. In the second step, $0.0015\ g$ of $JUN{-}Fe_3O_4$, $ROS{-}Fe_3O_4$, $MAT{-}Fe_3O_4$ and $ARM{-}Fe_3O_4$ NPs powders were added to a volume of $4\ ml$ of dye aqueous solutions. Dye solutions concentration was $0.0111\ mg/ml$. The ionic strength for all adsorption experiments was kept at $0.1\ M$ by adding an appropriate amount of $NaCl$ (0.023g). A dilute solution of HCl was used to adjust dye/Fe_3O_4 solutions pH to 4. All experiment sets are sonicated in an ultrasonic bath for 15 min and they were then stirred continually for 60 min until a steady state was reached. A control experiment (without NPs) was also performed. All adsorption experiments were carried out in dark ambient conditions in batch mode, and they were performed in triplicate for data consistency.

Kinetic experiments were performed by withdrawing samples of MG/Fe_3O_4 solutions at a regular interval of time to obtain, after centrifugation, adequate aliquots for the purpose of quantifying residual dye concentrations and the adsorbed amounts. The concentrations of residual dye aqueous solutions were quantified using UV-Vis spectrophotometer at absorbance maxima of MG

$\lambda_{max} = 249\ nm$. Furthermore, the adsorbed amounts of MG molecules are calculated from the calibration curve for all adsorption experiments (Y=42.049X-0.2885, R^2=0.996). In order to obtain the adsorption capacity q_e^1 (mg/g) and the amount of MG cations adsorbed per unit mass (q_t^1 in (mg/g)) of magnetite NPs at equilibrium contact time in the first process of MG adsorption in dark ambient conditions, the following equations were used:

$$q_e^1 = \frac{(C_0 - C_e^1)V}{m} \tag{4.1}$$

$$q_t^1 = \frac{(C_0 - C_t^1)V}{m} \tag{4.2}$$

Adsorption yield was calculated using the following equation:

$$R^1\% = \frac{(C_0 - C_e^1)}{C_0}.100 \tag{4.3}$$

where, C_0, C_e^1, C_t^1, V and m are respectively: initial dye concentration without any treatment (mg/ml), residual dye concentration in liquid phase at steady state after the first process of MG adsorption in dark ambient conditions (mg/ml), residual dye concentration in liquid phase at steady state after the accomplishment of the first process of MG adsorption in dark ambient conditions (mg/ml) at time t, the volume of dye solution (ml), and the amount of magnetite NPs (g).

Pseudo-First-Order and Pseudo-Second-Order Kinetics

The pseudo-first-order (PFO) of Lagergren [166] and pseudo second order of Ho and Mckay [167] kinetic models are selected to test the adsorption dynamics in this study due to their good applicability in most studies [168], [169]. The Lagergren kinetic model assumes that the rate of occupation of adsorption sites is proportional to the number of unoccupied sites [170]. Lagergren's model (eq. 4.5) is suitable for only the initial 20 to 30 minutes of the adsorption action and not for the whole range of contact times [167]. It is generally represented by the following equation:

$$\frac{dq_t^1}{dt} = K_1(q_e^1 - q_t^1) \tag{4.4}$$

After integration by applying conditions, $q_t^1 = 0$ at $t = 0$ and $q_t = q_t^1$ at $t = t$, then 4.4 becomes:

$$ln(q_e^1 - q_t^1) = lnq_e^1 - K_1 t \tag{4.5}$$

where, K_1, q_t^1 and q_e^1 are respectively: Pseudo-first-order kinetic constant (mn^{-1}), adsorbed dye quantity at instant t (mg/g) and adsorbed dye quantity at thermodynamic equilibrium in dark ambient conditions (mg/g).

If the active surface of the adsorbent is regarded as invariable, the reaction could be treated as pseudo-first-order kinetic. However, once the active sites have been saturated, the transfer at pollutant/adsorbent particle interface may be limited by mass transfer [132].

The pseudo-second-order (PSO) model (eq 4.6) is proposed by Ho and McKay [167]. It based on the adsorption capacity expressed as follow:

$$\frac{t}{q_t^1} = \frac{1}{K_2 q_e^1} + \frac{t}{q_e^1} \tag{4.6}$$

where, K_2, q_t^1 and q_e^1 are: Pseudo second order kinetic constant ($mg/g.mn$), adsorbed dye quantity at instant t (mg/g) and adsorbed dye quantity at thermodynamic equilibrium in first process (mg/g), respectively.

Intra-particles Diffusion Kinetics

In order to gain insights into the adsorption mechanisms involved, a homogeneous particle diffusion model (HPDM) as shown in Eq 4.7, originally proposed by Boyd et al. [171], is used to describe the diffusive adsorption process. In this model, the rate-limiting step is usually described by either an intra-particle diffusion or a film diffusion mechanism.

$$F(t) = 1 - \frac{6}{\pi^2} \sum_{Z=1}^{\infty} \frac{1}{Z^2} exp\left[\frac{-Z^2 \pi^2 D_{p^t}}{r_0^2}\right] \tag{4.7}$$

where F(t) is the fractional attainment at time t, i.e., $F(t) = qt^1/qe^1$, D_p (m^2/s) is the effective diffusion coefficient, r_o is the radius of Fe_3O_4 particles assumed to be spherical, and Z is an integer. For $0 < F(t) < 1$, a simplified equation can be obtained for the adsorption on spherical particles:

$$F(t) = 1 - exp - \frac{\pi^2 D_p^2 t^2}{r_0^2} \tag{4.8}$$

A further formula deformation gives the following:

$$-ln(1 - F^2(t)) = \frac{2D_p\pi^2}{r_0^2}t = 2k_pt \tag{4.9}$$

where k_p is the diffusion rate constant $(1/s)$ and $k_p = D_p\pi^2/r_0^2$. Eq 4.9 was used for the calculation of effective intra-particle diffusivity $(D_p(m^2/s))$ from the experimental data. In the first step, a graph of $-ln(1 - F^2(t))$ vs t was developed. The values of k_p of $MG/ARM{-}Fe_3O_4$, $MG/ROS{-}Fe_3O_4$, $MG/MAT{-}Fe_3O_4$, and $MG/JUN{-}Fe_3O_4$ adsorption processes are obtained from the slopes of the fitted lines (plots of $-\ln(1-F^2)$ vs time), and the values of effective diffusion coefficients, $D_p(m^2/s)$, can then be obtained from $D_p = k_p\pi^2/r_0^2$.

Additionally, Eq 4.10 can be used when the rate of adsorption is controlled by liquid film diffusion [172].

$$F(t) = 1 - exp(-\frac{3D_fC_e^1}{r_0\delta C_r^1}) \tag{4.10}$$

where D_f is the film diffusion coefficient (m^2/s) in the liquid phase, and C_e^1 (mol/l) and C_r^1 (mol/l) are respectively the equilibrium concentrations of MG dye in solution and in solid phases. δ is the thickness of liquid film which was assumed to be 10^{-5} m according to Yu and Luo [173]. A further formula deformation of Eq 4.10 gives the following equation:

$$-\ln(1 - F) = K_f.t \tag{4.11}$$

where k_f is the diffusion rate constant $(1/s)$.

The values of $k_f = 3D_fc_e^1/r_0\delta c_r^1$ of MG adsorption on the four magnetite surfaces are obtained from the slopes of the fitted lines (plots of $-\ln(1-F)$ vs time), and the values of effective diffusion coefficient, $D_f(m^2/s)$, can then be obtained from $D_f = k_fr_0c_r^1/3c_e^1$.

The linearity test of Boyd plots ($-\ln(1-F)$ and $-\ln(1-F^2)$) versus time plots are employed to distinguish between the film diffusion and particle diffusion-controlled adsorption mechanisms. If the plot of $-\ln(1-F)$ versus time is a straight line passing through the origin, then the adsorption rate is governed by particle diffusion mechanism otherwise if $-\ln(1-F^2)$ versus time is a straight line passing through the origin then the adsorption is governed by film diffusion.

4.2.2.2 Batch Thermocatalysis Experiments of Magnetite Samples in Dark Conditions

In order to study the thermocatalysis of the four magnetite NPs samples under heat, all sets of experiments containing MG/Fe_3O_4 residual solutions after the first process of MG adsorption are sonicated in an ultrasonic bath during 15 min and they were then stirred continually for 20 minutes in dark conditions in different temperatures ranging from 303.15 to $318.15\ K$. The concentrations of residual dye in liquid phases are quantified using UV-Vis spectrophotometer at absorbance maxima of MG $\lambda_{max} = 249\ nm$. Furthermore, the adsorbed amounts of MG molecules are calculated from the calibration curve for all adsorption experiments (Y=42.049X-0.2885, R^2=0.996). In order to obtain the adsorption capacity q_e^2 (mg/g) of all magnetite samples after thermocatalysis in the second process of MG adsorption in dark conditions the following equations are used:

$$q_e^2 = \frac{(C_0 - C_e^2)V}{m} \tag{4.12}$$

Adsorption yield was calculated using the following equation:

$$R^2\% = \frac{(C_0 - C_e^2)}{C_0}.100 \tag{4.13}$$

where, C_0, C_e^2, V and m are respectively: initial dye concentration without any treatment (mg/ml), residual dye concentration in liquid phase at steady state in the first process of MG adsorption in dark ambient conditions (mg/ml), the volume of dye solution (ml), and the amount of magnetite (g).

The activation enthalpy (ΔH^0) of MG adsorption on magnetite surface is determined using Arrhenius equation as follow:

$$lnk_d = \frac{\Delta S^0}{R} - \frac{\Delta H^0}{RT} \tag{4.14}$$

where R ($1.987\ cal/molK$) is the universal gas constant, T is the absolute solution temperature (K), and K_d is the distribution coefficient which can be calculated as:

$$k_d = \frac{C_{ae}^2}{C_e^2} \tag{4.15}$$

where C_{ae}^2 (mg/ml) and C_e^2 (mg/ml) are respectively the concentration of adsorbed dye on the solid and dye residual concentration in liquid phase after thermocatalysis in dark conditions.

The values of activated ΔH^0 and ΔS^0 were calculated from the slope and intercept of the plot between lnK_d versus $1/T$. ΔG^0 was then calculated using the relation:

$$\Delta G^0 = -RTlnK_d \tag{4.16}$$

The free energy change indicates the degree of the spontaneity of the adsorption process and the higher negative value reflects more energetically favorable adsorption. The activation energy (ΔE_a) of MG adsorption on magnetite surface is determined using the following Arrhenius's equation:

$$lnk_2 = lnA - \frac{E_a}{RT} \tag{4.17}$$

where K_2 is the distribution coefficient which can be calculated by:

$$k_2 = \frac{q_e^2}{C_e^2} \tag{4.18}$$

where q_e^2 (mg/g) and C_e^2 (mg/ml) are respectively the adsorption capacity of dye on solid and dye residual concentration in liquid phase after thermocatalysis in the second process of MG adsorption in dark conditions.

4.2.2.3 Batch Photocatalysis Experiments of Magnetite Samples in Ambient Conditions

In the third MG adsorption process, the study of photocatalysis of $JUN-Fe_3O_4$, $ROS-Fe_3O_4$, $MAT-Fe_3O_4$ and $ARM-Fe_3O_4$ NPs under UV irradiation to degrade MG are conducted on all sets of experiment containing residual solutions after thermocatalysis in dark conditions. All experiment sets are sonicated in an ultrasonic bath for 15 min and then they are stirred continuously and exposed to direct UV irradiation (365 nm) in ambient conditions at different times ranging from 60 to 240 minutes. The concentrations of residual dye aqueous solutions were quantified using UV-Vis spectrophotometer at absorbance maxima of MG $\lambda_{max} = 249\ nm$. Furthermore, the adsorbed amounts of MG molecules are calculated from the calibration curve for all adsorption experiments (Y=42.049X-0.2885, R^2=0.996). In order to obtain the adsorption capacity q_e^3 $(mg.g^{-1})$ by photocatalysis in ambient conditions under UV irradiation of $JUN-Fe_3O_4$, $ROS-Fe_3O_4$,

$MAT{-}Fe_3O_4$ and $ARM{-}Fe_3O_4$ the following equations are used:

$$q_e^3 = \frac{(C_0 - C_e^3)V}{m} \tag{4.19}$$

Adsorption yield was calculated using the following equation:

$$R^3\% = \frac{(C_0 - C_e^3)}{C_0}.100 \tag{4.20}$$

where, C_0, C_e^3, V and m are respectively: initial dye concentration without any treatment (mg/ml), dye residual concentration in liquid phase after photocatalysis in the third process of MG adsorption in ambient conditions (mg/ml) under UV irradiation, the volume of dye solution (ml), and the amount of magnetite (g).

The degradation kinetics of MG using Fe_3O_4 NPs can be expressed as a pseudo-first-order (PFO) reaction as follows:

$$ln(C_0/C_t^3) = k_{pd}.t \tag{4.21}$$

where, C_0, C_t^3, and k_{pd} are respectively the initial concentration of MG without any treatment (mg/g), dye residual concentration (mg/g) in liquid phase at time t after photocatalysis under UV irradiation, and the PFO photocatalytic degradation rate constant (min^{-1}) which can be calculated from the slope of $ln(C_0/C_t^3)$ versus t plot.

4.3 Results and Discussion

4.3.1 X-ray Analysis of Fe_3O_4 NPs Samples

X-ray patterns of all synthesised samples are presented in Figure 4.2. It is found that all synthesized samples have crystalline structures. X-ray diffraction of pattern (A)-Figure 4.2 exhibit Bragg reflection peaks at around $2\theta° = 16.20°$, $20.30°$, $22.39°$, $25.60°$, $29.72°$, $32.30°$, $41.05°$, $41.39°$, $42.48°$, and $52.69°$. All Bragg peaks are in agreement with orthorhombic Fe_3O_4 powder and corresponding to Miller indices *021*, *212*, *030*, *400*, *314*, *001*, *250*, *251*, *522*, and *644*, respectively (JCPDF file 01-076-0958).

X-ray diffraction pattern (B)-Figure 4.2 exhibit Bragg reflection peaks at around $2\theta° = 16.20°$, $16.70°$, $20.39°$, $22.42°$, $29.75°$, $30.80°$, $32.30°$, $41.10°$, $42.53°$, $49.82°$, and $52.72°$. All Bragg peaks are in agreement with orthorhombic Fe_3O_4 powder and corresponding to Miller indices *021*, *210*, *212*, *030*, *400*, *041*,*106*, *251*, *522*, *534*, and *644*, respectively (JCPDF file 01-076-0958).

X-ray diffraction of pattern (C)-Figure 4.2 exhibit Bragg reflection peaks at around $2\theta° =$ $16.20°$, $22.56°$, $26.04°$, $32.28°$, $37.11°$, $41.59°$, $49.98°$, and $52.69°$. All Bragg peaks are in agreement with orthorhombic Fe_3O_4 powder and corresponding to Miller indices *021*, *030*, *400*, *106*, *404*, *251*, *534*, and *644*, respectively (JCPDF file 01-076-0958).

X-ray diffraction of pattern (D)-(Figure 4.2 exhibit Bragg reflection peaks at around $2\theta° =$ $16.35°$, $20.58°$, $22.60°$, $25.77°$, $29.94°$, $32.47°$, $41.59°$, $42.69°$ $49.98°$, and $52.69°$. All Bragg peaks are in agreement with orthorhombic Fe_3O_4 powder and corresponding to Miller indices *021*, *212*, *030*, *400*, *001*, *106*, *251*, *522*, *534*, and *644*, respectively (JCPDF file 01-076-0958 [1]).

The average diameters of different Fe_3O_4 samples, presented in Table 4.2, were calculated from XRD patterns using Scherrer's equation [155]:

$$D = \frac{0.9\lambda}{\beta \cos\theta} \tag{4.22}$$

where D, β, λ, and θ are the crystallite size, the full width at half-maximum (FWHM) of the most intense diffraction peak, the X-ray wavelength (1.54056 Å), and Bragg angle, respectively.

Table 4.1: Calculated average diameter of $ARM{-}Fe_3O_4$, $ROS{-}Fe_3O_4$, $MAT{-}Fe_3O_4$ and $JUN{-}Fe_3O_4$ NPs

Samples	Average Diameter (nm)
$ARM - Fe_3O_4$	41.49
$ROS - Fe_3O_4$	39.89
$MAT - Fe_3O_4$	33.13
$JUN - Fe_3O_4$	29.27

4.3.2 FTIR-ATR Spectroscopy Analysis

FTIR spectra of synthesized Fe_3O_4 NP powders recorded between 4000 and 500 cm^{-1} are presented in Figure 4.3. Figure 4.3 shows that all IR spectra (A, B, C, and D) exhibit peaks in different ranges as is summarized in Table 4.2. The peaks at $3223.41 - 3266.69$ cm^{-1} correspond to $O - H$ stretching vibration, where the peaks at $2930.18 - 2932.06$ cm^{-1} correspond to $C - H$ vibrations.

---

[1] See Appendix C

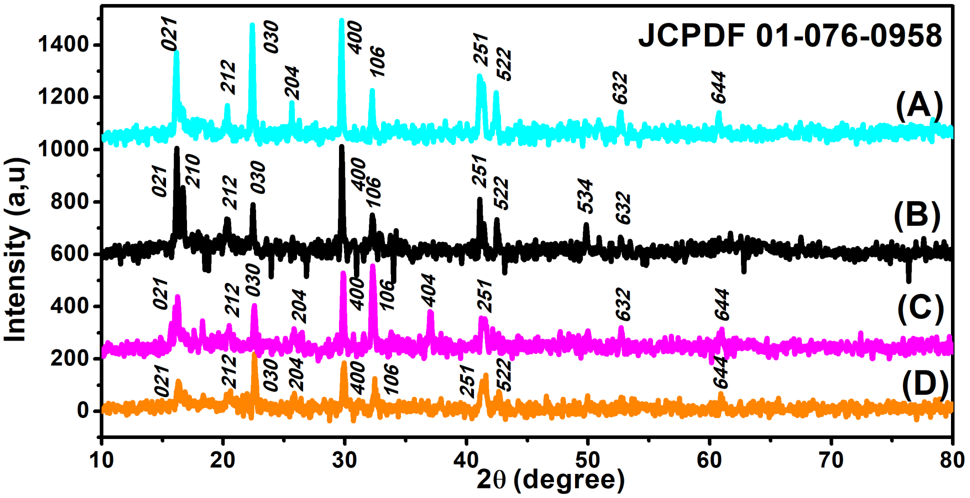

Figure 4.2: XRD patterns of (A) $ROS{-}Fe_3O_4$, (B) $ARM{-}Fe_3O_4$, (C) $MAT{-}Fe_3O_4$, and (D) $JUN{-}Fe_3O_4$ NP powders, JCPDF file 01-076-0958

Table 4.2: FTIR vibration of Fe_3O_4 functional groups

Sample	$O-H$ cm^{-1}	$C-H$ cm^{-1}	$C=C$ cm^{-1}	$C-O-C$ cm^{-1}	$Fe-O$ cm^{-1}
$ARM{-}Fe_3O_4$	3266.69	2932.06	1590.07	1036.36	592.64
$ROS{-}Fe_3O_4$	3249.77	2930.18	1590.83	1038.75	591.83
$MAT{-}Fe_3O_4$	3235.57	2929.75	1591.21	1039.54	592.46
$JUN{-}Fe_3O_4$	3223.41	2928.82	1594.63	1039.45	592.69

The peaks at $1590.07 - 1594.63$ cm^{-1} correspond to $C{=}C$ stretch in aromatic rings and anti-symmetric stretching of the carboxylate group (COO^-), whereas peaks at $1033.45{-}1044.36$ cm^{-1} are assigned to $C{-}O{-}C$ of the phenolic groups [70]. The peak at around 592 cm^{-1} is corresponding to $Fe - O$ stretching band of Fe_3O_4 NPs [174].

Figure 4.3 shows that the peaks of hydroxyl groups appear in remarkably different areas. Whereas, hydroxyl groups peak area appears the broadest one on $ARM{-}Fe_3O_4$ surface, next on $ROS{-}Fe_3O_4$, then on $MAT{-}Fe_3O_4$, and finally on $JUN{-}Fe_3O_4$. This reveals that the density of functional OH groups is more higher on $ARM{-}Fe_3O_4$ surface, next on $ROS{-}Fe_3O_4$, then on $MAT{-}Fe_3O_4$, and finally on $JUN{-}Fe_3O_4$.

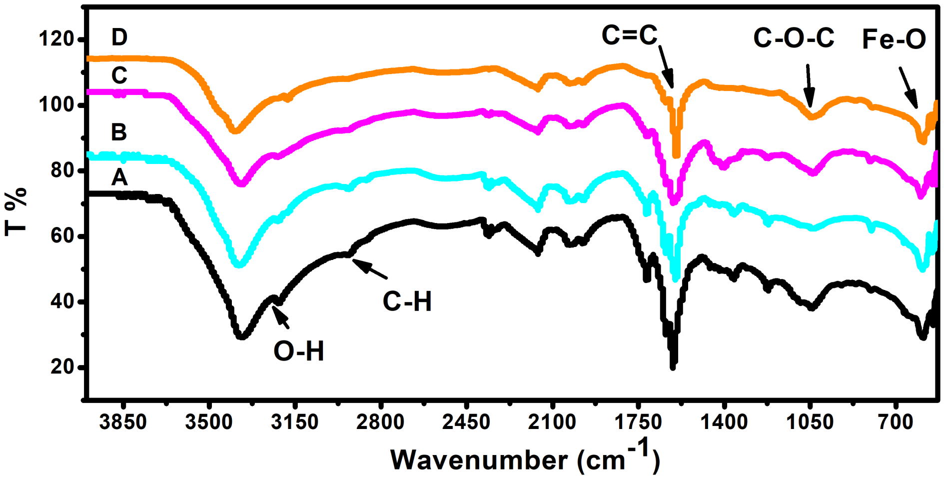

Figure 4.3: IR spectra of synthesized (A) $ARM{-}Fe_3O_4$, (B) $ROS{-}Fe_3O_4$, (C) $MAT{-}Fe_3O_4$, and (D) $JUN{-}Fe_3O_4$ NP powders

4.3.3 UV-Vis Spectroscopy Analysis

The optical absorbance spectra of all Fe_3O_4 samples are measured in the wavelength range of $200-900\ nm$. The band gap energies of Fe_3O_4 samples are then deduced from those spectra. The band gap E_g and the optical absorption coefficient (α) of a semiconductor are related through the known following equation [161]:

$$\alpha h\nu = A(h\nu - E_g)^n \tag{4.23}$$

where α is the linear absorption coefficient of the material, $h\nu$ is the photon energy, A is a proportionality constant, and the exponent n depends on the nature of electronic transition; it is equal to $1/2$ for direct allowed transition and 2 for indirect allowed transition. E_g of the direct transition of all samples were obtained from plotting $(\alpha h\nu)^2$ as a function of $\alpha h\nu$ by the extrapolation of the linear portion of the curve (Figure 4.4). However, E_g of the indirect transition of all samples were obtained from plotting $(\alpha h\nu)^{1/2}$ as a function of $\alpha h\nu$ by the extrapolation of the linear portion of the curve (4.5)

Estimated indirect band gap energies of $ARM{-}Fe_3O_4$, $ROS{-}Fe_3O_4$, $MAT{-}Fe_3O_4$ and $JUN{-}Fe_3O_4$ phases were found as 2.51, 2.55, 2.60 and $2.64\ eV$, respectively, which are higher than reported by reference value [175]. They found that indirect gap energy for Fe_3O_4 equals $E_g =$

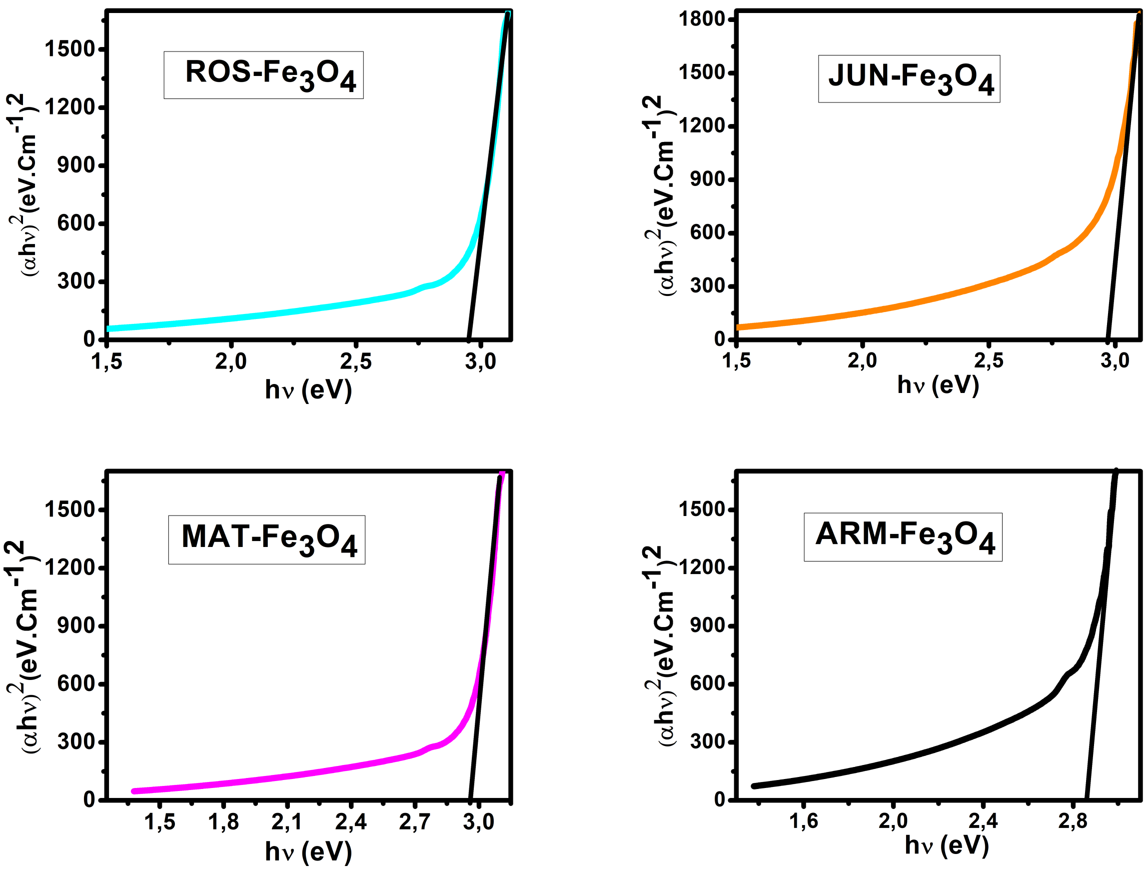

Figure 4.4: Plots of $(\alpha h\nu)^2$ versus $(\alpha h\nu)$ for direct transition of greenly synthesized Fe_3O_4 NP samples sonicated in acetone during 15 minutes

$1.92\,eV$. Estimated direct band gap energies of $JUN\!-\!Fe_3O_4$, $MAT\!-\!Fe_3O_4$, $ROS\!-\!Fe_3O_4$, and $ARM\!-\!Fe_3O_4$ samples were found as 2.97, 2.95, 2.94 and 2.87 eV, respectively, which are close to that found by El Ghandoor et al. [175]. They found that direct gap energy for Fe_3O_4 equals $E_g = 2.87\ eV$. It is clear that the direct gap energy is closer to the theoretical value than the indirect gap energy. The values of all direct band gap energies of magnetite NP samples classify them as semiconductors. The energy band gap of the semiconductors is between 0 and 3 eV [162].

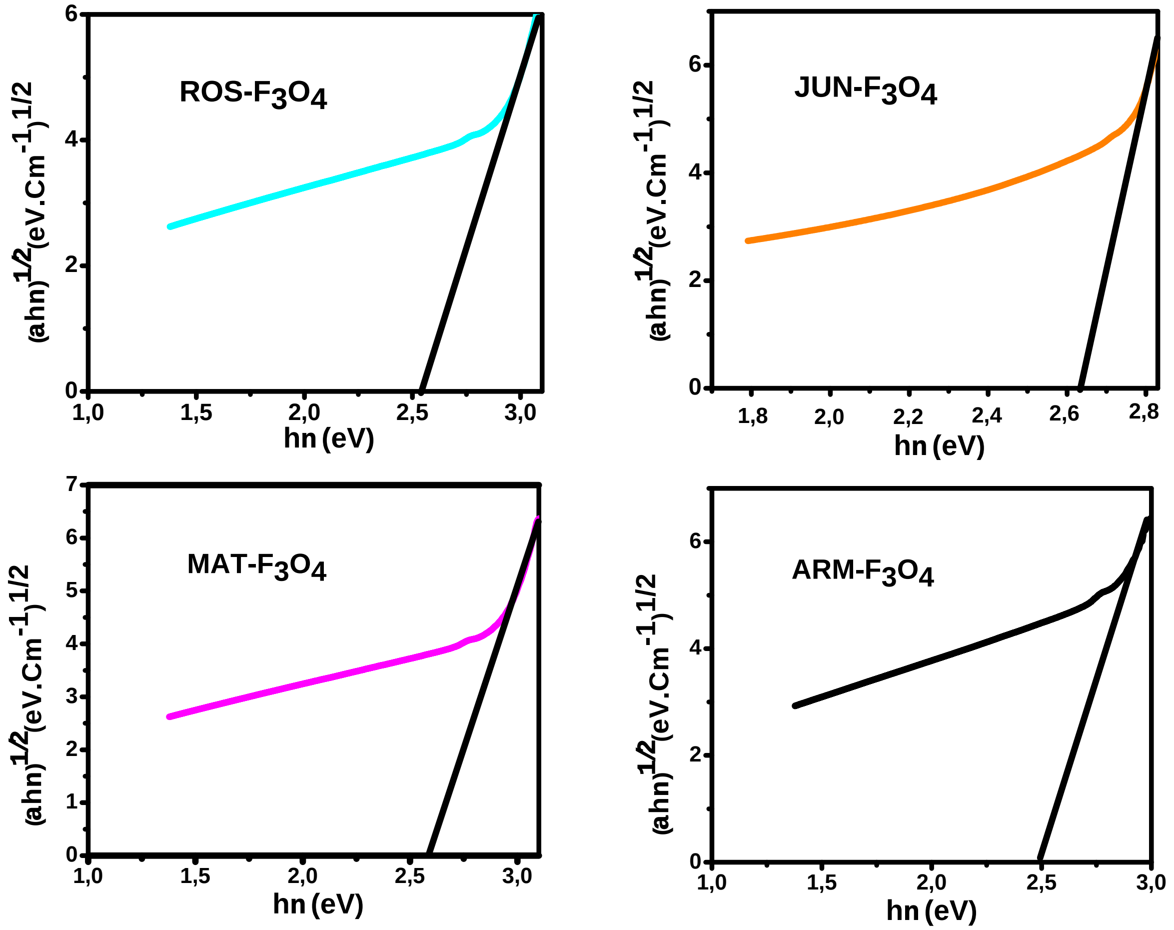

Figure 4.5: Plots of $(\alpha h\nu)^{1/2}$ versus $(\alpha h\nu)$ for indirect transition of greenly synthesized Fe_3O_4 NP samples sonicated in acetone during 15 minutes

4.3.4 SEM Images of Greenly Synthesised Fe_3O_4 NP Samples

SEM images of synthesized iron oxide NP samples are presented in Figure 4.6. It is clearly shown that all four magnetite NPs are depending on the plant extract. Different irregular shapes are observed in all samples as rocks shape. For $ROS{-}Fe_3O_4$ NPs, it is clear that a few agglomerations like rocks are presented in Figure 4.6a. Whereas for $JUN{-}Fe_3O_4$ NPs, like mountains with bigger rocks are presented, as shown in Figure 4.6b. However, for $MAT{-}Fe_3O_4$ a decrease in the dimension of the like mountains with more adherence to its structure is observed (Figure 4.6c). Finally, for $ARM{-}Fe_3O_4$, a big bipyramids crystals are appeared as mentioned in Figure 4.6d.

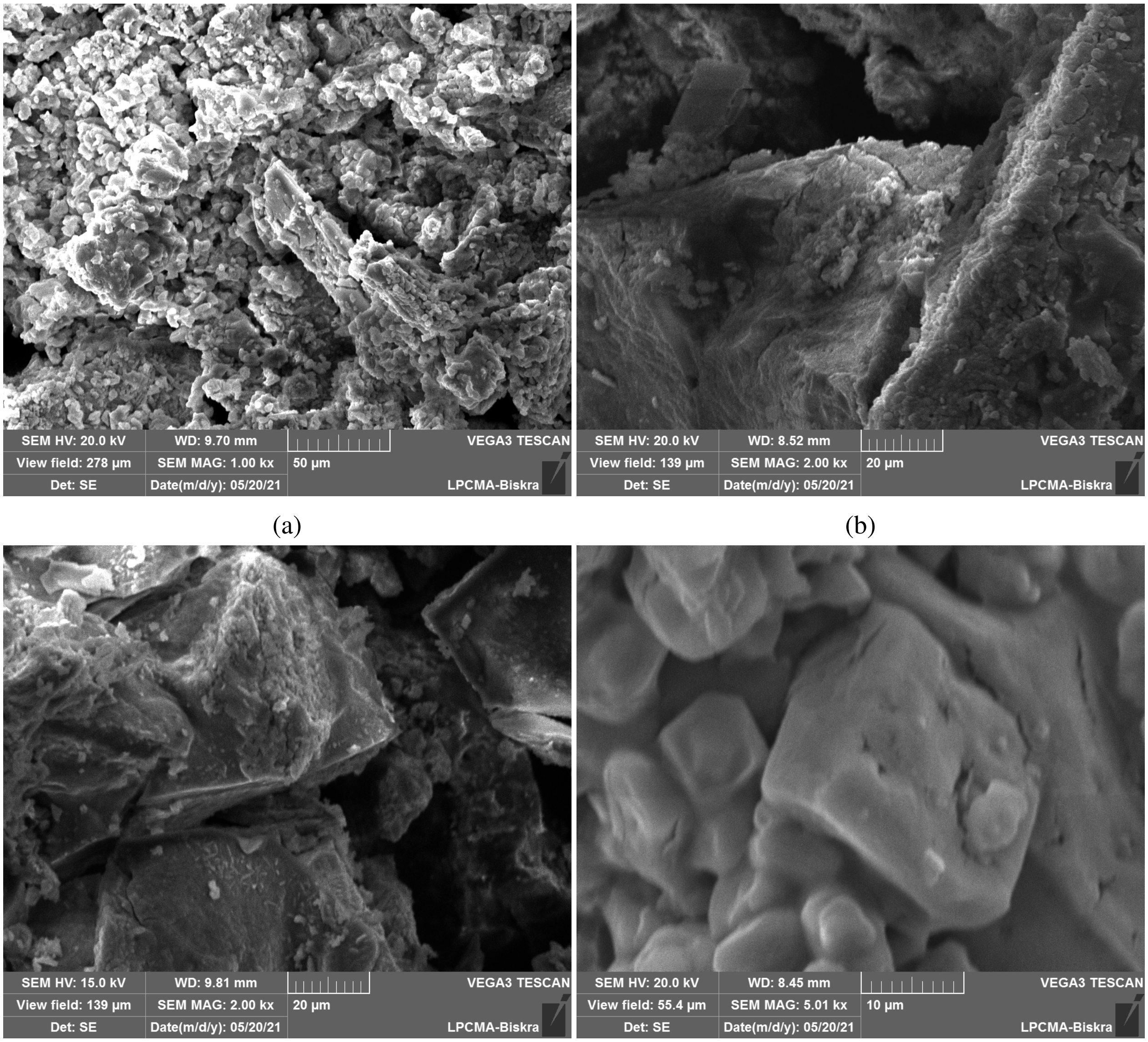

(a) (b)

(c) (d)

Figure 4.6: SEM images of greenly synthesized $JUN-Fe_3O_4$, $MAT-Fe_3O_4$, $ROS-Fe_3O_4$ and $ARM-Fe_3O_4$ NPs

4.3.5 The Analysis of MG Adsorption Kinetics and Thermodynamics

4.3.5.1 Adsorption Equilibrium in Preferential MG Adsorption

In all adsorption experiments, the steady-state is reached within 30 minutes, as depicted in Figure 4.7. This denotes very fast adsorption kinetics of MG on all four magnetite NP surfaces.

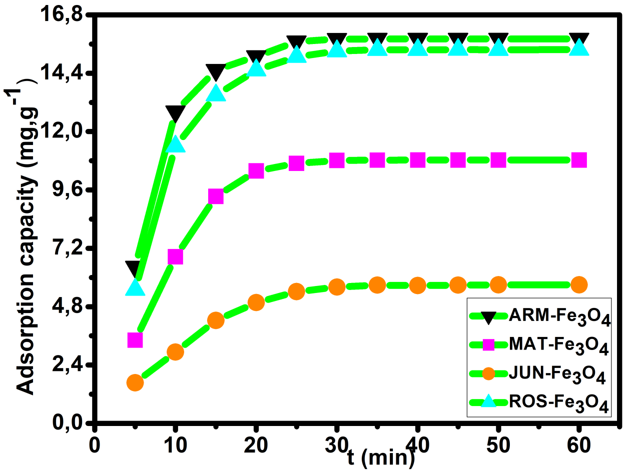

Figure 4.7: Adsorption Capacity of MG on the four magnetite samples in the first process of MG adsorption in ambient dark conditions

4.3.5.2 Pseudo-First-Order and Pseudo-Second-Order Kinetics of preferential MG Adsorption

The results of pseudo-first-order kinetics analysis for adsorption of MG molecules on all four magnetites NP surfaces (Table 4.3 and Figure 4.8a) indicate good linearity and a good fit of the experimental data to this model compared to the pseudo-second-order model which indicated poor linearity and poor fit of the experimental data (Table 4.3 and Figure 4.8b). The q_e^1 (equilibrium adsorption capacity) computed from pseudo-first-order kinetics plots are also in very close agreement with the empirical q_e contrary to the q_e^1 calculated from pseudo-second-order plots (see Table 4.3). This indicates the best compliance of MG adsorption on all four magnetite NP surfaces with pseudo-first-order kinetic.

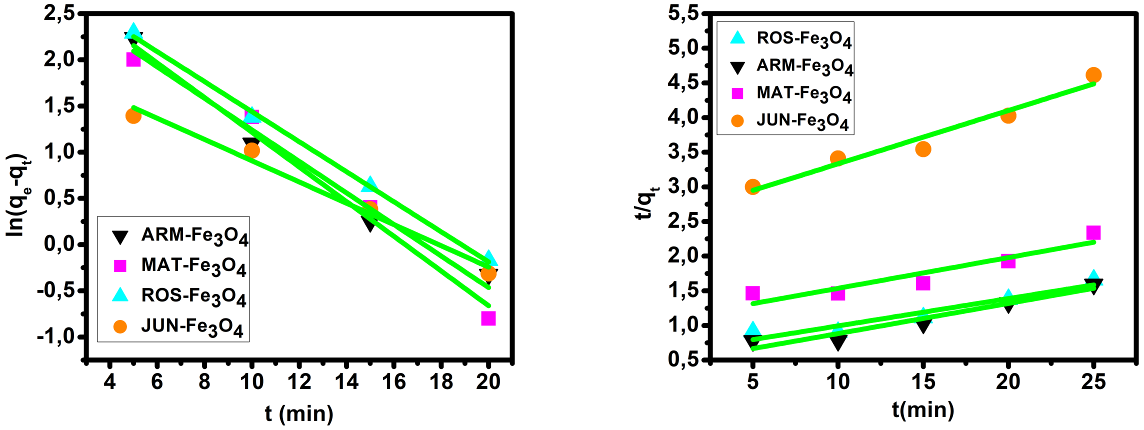

(a) (b)

Figure 4.8: (a) Plots of $ln(q_e^1 - q_t^1)$ versus time and (b) plots of t/q_t^1 versus time of MG adsorption on Fe_3O_4 NP samples in the first process of adsorption

Table 4.3: Adsorption Kinetics Parameters for MG adsorption on Fe_3O_4 NP samples in dark ambient conditions

Sample	$q^1_{e,exp}$ (mg/g)	$q^1_{e,cal}$ (mg/g)	$K_1.10^{-3}$ (mn^{-1})	R^2	$q^1_{e,cal}$ (mg/g)	$K_2.10^{-3}$ $(g.mg^{-1}.mn^{-1})$	R^2
$ARM{-}Fe_3O_4$	15.81	18.92	5.76	0.9783	22.99	3.78	0.9387
$ROS{-}Fe_3O_4$	15.37	21.33	9.39	0.9984	25.32	2.60	0.9220
$MAT{-}Fe_3O_4$	10.83	19.88	8.86	0.9902	22.32	1.85	0.9028
$JUN{-}Fe_3O_4$	05.69	07.84	8.53	0.9839	13.00	2.31	0.9607

4.3.5.3 Intra-particles Diffusion Kinetics of preferential MG Adsorption

The linearity tests of Boyd plots $-\ln(1 - F)$ and $-\ln(1 - F^2)$ versus time are presented in Figures 4.9a and 4.9b. They show that kinetic data correlate well with the homogeneous particle diffusion model as confirmed with the high R^2 values. The results of linear regression analysis for equations 4.9 and 4.11are presented in Table 4.4. Found film diffusion coefficients D_f were in the order of 10^{-11} m^2/s, while intra-particle diffusion coefficients D_p were found in the order of 10^{-19} m^2/s. As it is known the adsorption mechanism is controlled by film diffusion at D_f ranging from $10^{-10} - 10^{-12}$ m^2/s, while intra-particle diffusion is the rate-limiting step at D_p in the range of $10^{-15} - 10^{-18}$ m^2/s [176]. Found results indeed indicate that film diffusion is the step

Table 4.4: Calculated Homogeneous particle diffusion parameters in the first Process of MG Adsorption on the four magnetite samples

Sample	$r_0.10^{-9}$ (m)	$k_p.10^{-3}$ (1/s)	R^2	$D_p.10^{-19}$ (m^2/s)	$k_f.10^{-3}$ (1/s)	R^2	$C_r^1.10^{-3}$ (mg/g)	$C_a^1.10^{-3}$ (mg/g)	$D_f.10^{-11}$ (m^2/s)
ARM-Fe_3O_4	41.94	2.68	0.9411	4.77	5.61	0.9594	5.17	5.93	06.84
ROS-Fe_3O_4	39.89	2.00	0.9736	3.22	4.29	0.9826	5.34	5.76	05.28
MAT-Fe_3O_4	33.13	2.67	0.9645	2.97	5.32	0.9599	7.11	3.99	10.49
JUN-Fe_3O_4	29.27	1.50	0.9544	1.30	3.38	0.9701	8.96	2.14	13.81

that controls the adsorption mechanism of MG on Fe_3O_4 surfaces, which is in agreement with the pseudo-first-order kinetic model.

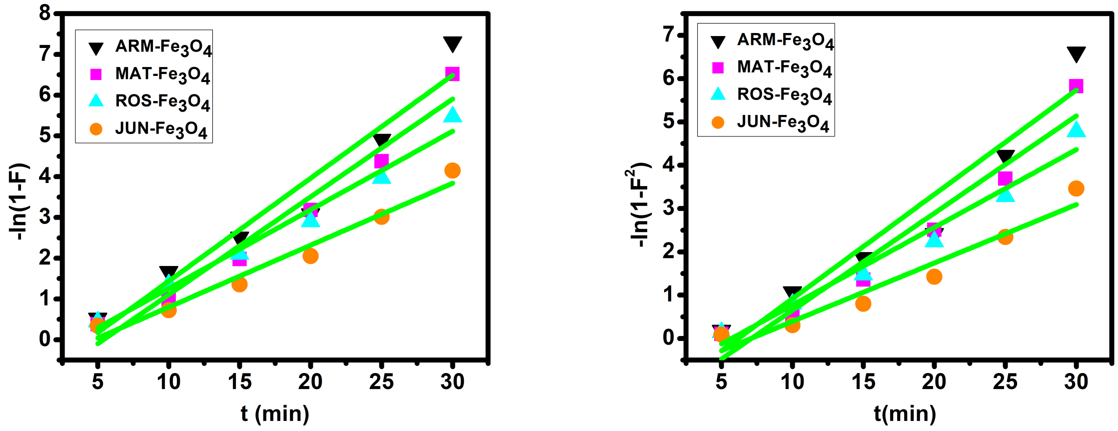

(a) (b)

Figure 4.9: Boyd plots of MG Adsorption on Fe_3O_4 surfaces in the first process of adsorption: (a) plots of $-ln(1-F)$ versus time and (b) plots of $-ln(1-F^2)$ versus time

4.3.5.4 Activation Thermodynamic Parameters of MG Adsorption under Thermocatalysis Process

The calculated activated enthalpy (ΔH^0), entropy (ΔS^0), and free energy (ΔG^0) are listed in Table 4.5. ΔH^0 and ΔS^0 are respectively calculated from the slopes and intercepts of the Arrhenius linear plots of lnk_D versus $1/T$ (**??**). Activated enthalpy in all four MG/Fe_3O_4 systems is positive, which indicates the endothermic nature of the adsorption processes and possible strong bonding between MG molecules and functional hydroxyl groups on Fe_3O_4 surfaces. The found

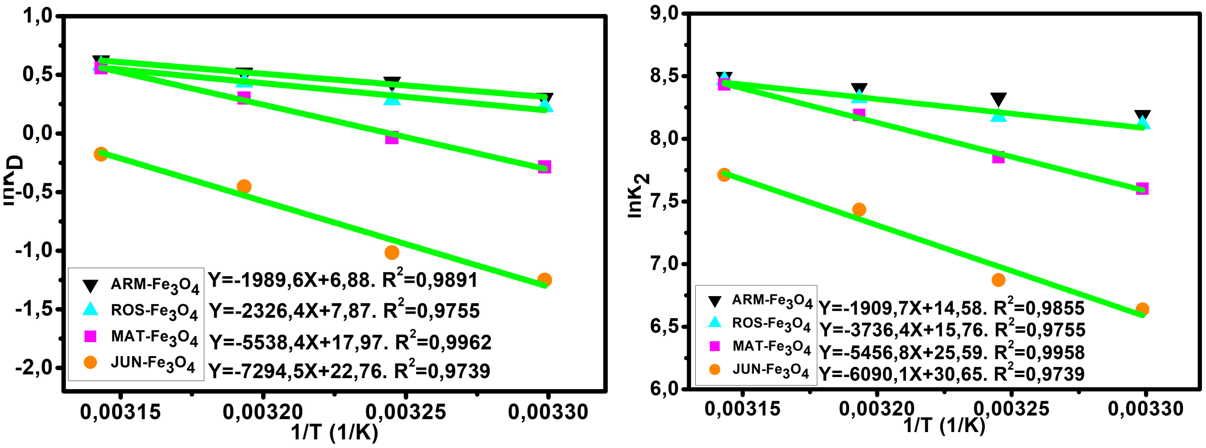

(a) (b)

Figure 4.10: (a) Plots of lnK_D versus $1/T$ of MG adsorption on Fe_3O_4 samples, (b) Plots of lnK_2 versus $1/T$ of MG adsorption on Fe_3O_4 NP surfaces

activated enthalpy of $MG/JUN\!-\!Fe_3O_4$ system is the highest one (14.49 $kcal/mol$), and that of $MG/ARM\!-\!Fe_3O_4$ system is the lowest one (4.59 $kcal/mol$). This indicates that the bonding between MG molecules and hydroxyl groups on $JUN\!-\!Fe_3O_4$ NPs are the strongest ones, then on $MAT\!-\!Fe_3O_4$, next on $ROS\!-\!Fe_3O_4$, and finally on $ARM\!-\!Fe_3O_4$ NP surfaces.

The activated entropy in all four MG/Fe_3O_4 systems are positive, which reveals the affinity of Fe_3O_4 surfaces for MG molecules. The increasing randomness at the MG/Fe_3O_4 solution interface indicates that a height significant changes in surfaces active hydroxyl groups number occurred in the internal structure of Fe_3O_4 surfaces. However, activated entropy of $MG/JUN\!-\!Fe_3O_4$ system is the highest one (45.23 $cal/mol.K$), and that of $MG/ARM\!-\!Fe_3O_4$ (15.58 $cal/mol.K$) is the lowest one. This indicates that the changes occurred in the structure of $JUN\!-\!Fe_3O_4$ NP surface are the highest ones, then of $MAT\!-\!Fe_3O_4$, next of $ROS\!-\!Fe_3O_4$, and finally of $ARM\!-\!Fe_3O_4$ NP surfaces [177], [178].

The activated free energies of both $MG/ARM\!-\!Fe_3O_4$ (-0.18, -0.24, -0.32, and -0.39) and $MG/ROS\!-\!Fe_3O_4$ (-0.14, -0.17, -0.27, and -0.37 $kcal/mol$) systems are negative. However, activated energies of $MG/ARM\!-\!Fe_3O_4$ system are more negative than those of $MG/ROS\!-\!Fe_3O_4$ system, which indicates the feasibility of MG adsorption process and its spontaneous nature with more MG adsorption on $ARM\!-\!Fe_3O_4$, then on $ROS\!-\!Fe_3O_4$ surfaces. In $MG/MAT\!-\!Fe_3O_4$ system, the values of activated free energies are negative only at 313.15 K and 318.15 K (-0.19 and

-0.35 $kcal/mol$, respectively), while a positive values are found at 303.15 K and 308.15 K (0.17 and 0.022 $kcal/mol$, respectively). This leads to proclaim the spontaneity of MG adsorption at 313.15 K and 318.15 K. Activated free energies of $MG/JUN{-}Fe_3O_4$ system (0.75, 0.62, 0.28, and 0.11 $kcal/mol$) are positive revealing that activated $MG{-}Fe_3O_4$ complexes are in an excited form in the transition state [177].

Table 4.5: Calculated thermodynamic Parameters for MG adsorption on Fe_3O_4 NP surfaces in the second process of adsorption

System	T K	$\ln K_D$	$\ln K_2$	E_a $kcal/mol$	ΔH^0 $kcal/mol$	ΔS^0 $cal/mol.K$	ΔG^0 $kcal/mol$
$MG/ARM{-}Fe_3O_4$	303.15	0.30	8.19	3.79	3.95	13.48	-0.18
	308.15	0.44	8.33				-0.27
	313.15	0.52	8.41				-0.32
	318.15	0.62	8.49				-0.39
$MG/ROS{-}Fe_3O_4$	303.15	0.23	8.17	7.42	4.62	15.64	-0.14
	308.15	0.29	8.31				-0.17
	313.15	0.44	8.61				-0.27
	318.15	0.58	8.72				-0.37
$MG/MAT{-}Fe_3O_4$	303.15	-0.28	7.60	10.84	11.00	35.70	+0.17
	308.15	-0.04	7.85				+0.02
	313.15	+0.30	8.19				-0.19
	318.15	+0.56	8.43				-0.35
$MG/JUN{-}Fe_3O_4$	303.15	-1.25	6.64	12.10	14.49	45.23	+0.75
	308.15	-1.01	6.87				+0.62
	313.15	-0.45	7.44				+0.28
	318.15	-0.18	7.71				+0.11

As presented in Table 4.5, the found activation energies (E_a) for MG adsorption on $ARM{-}Fe_3O_4$, $ROS{-}Fe_3O_4$, $MAT{-}Fe_3O_4$, and $JUN{-}Fe_3O_4$ surfaces are respectively: 4.43, 7.42, 10.84, and 12.10 $kcal/mol$. E_a is calculated from the slopes of Arrhenius linear plots of lnk_2 versus $1/T$ (**??**). The found low E_a suggests that MG adsorption on Fe_3O_4 proceeded with low energy barriers and can be achieved at relatively low temperatures. As it is known that the activation energy E_a of physical adsorption is ranges from 1.2 to $12 kcal/mol$, and from 14.3 to $191 kcal/mol$ for chemical adsorption [179], the adsorption processes of MG on all the four Fe_3O_4 are therefore physical in nature.

4.3.5.5 Pseudo-First-Order Kinetic Analysis of MG Adsorption Under Photocatalysis Process

The results of pseudo-first-order kinetic analysis of MG adsorption on the four magnetite NP surfaces (Figure 4.11) indicate good linearity of plots of $ln(C_0/C_t^3)$ versus time of UV irradiation as judged from high correlation coefficients ($R^2 > 0.98$), which indicates that the rate of MG degradation catalyzed by Fe_3O_4 NP samples is assumed to be fitted by a pseudo-first-order model. The corresponding photodegradation rates (k_{pd}) of MG by $JUN{-}Fe_3O_4$, $MAT{-}Fe_3O_4$, $ROS{-}Fe_3O_4$, and $ARM{-}Fe_3O_4$ are 0.00132 min^{-1}, 0.00125 min^{-1}, 0.00123 min^{-1}, and 0.00120 min^{-1}, respectively.

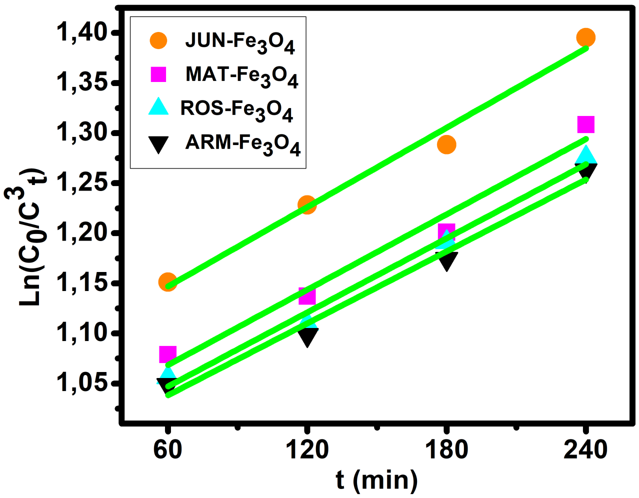

Figure 4.11: Kinetic plots of lnC_0/C_t^3 versus time of MG photodegradation on Fe_3O_4 NP samples

4.3.6 Preferential and Enhanced MG Adsorption on Magnetite Surfaces

4.3.6.1 Preferential Adsorption of MG Adsorption

Table 4.6 shows that, in the first process of MG adsorption in ambient dark conditions, the adsorption capacity and yield of MG differ depending on Fe_3O_4 NP sample. MG adsorption capacity (adsorption capacity is denoted q_e^1) and yield (denoted $R_1\%$) achieved 15.81 mg/g and 53.42% on $ARM{-}Fe_3O_4$ and 15.37 mg/g and 51.90% on $ROS{-}Fe_3O_4$. Whereas they achieved only

Table 4.6: Reached MG adsorption capacity and yield on $ARM{-}Fe_3O_4$, $ROS{-}Fe_3O_4$, $MAT{-}Fe_3O_4$ and $JUN{-}Fe_3O_4$ NPs in first process of MG adsorption in ambient dark conditions

Adsorbent	q_e^1 (mg/g)	MG $R_1\%$
$ARM{-}Fe_3O_4$	15.81	53,42
$ROS{-}Fe_3O_4$	15.37	51.90
$MAT{-}Fe_3O_4$	10.83	35.91
$JUN{-}Fe_3O_4$	05.70	19.25

10.83 mg/g and 35.91% on $MAT{-}Fe_3O_4$ and 19.25% and 5.70 mg/g on $JUN{-}Fe_3O_4$ surfaces. So, MG molecules are highly adsorbed on $ARM{-}Fe_3O_4$, next on $ROS{-}Fe_3O_4$, then on $MAT{-}Fe_3O_4$, and finally on $JUN{-}Fe_3O_4$ NPs. As all experiment conditions are maintained the same for all adsorption experiments on all four magnetite samples, so, only magnetite surface functionality is responsible for the preferential adsorption of MG on magnetite NP surfaces.

It is known that complexation and electrostatic interactions play important roles in determining the efficiency of adsorption [23]. When Fe_3O_4 is immersed in the aqueous acidic solution, it develops its surface charge via the protonation and deprotonation of $\equiv Fe - OH$ active sites on its surface according to the following equations [180]:

$$\equiv Fe - OH_2^+ \longleftrightarrow \equiv Fe - OH^0 + H_{sol}{}^+ (pk_{a1} = 5.1) \tag{4.24}$$

where, $\equiv Fe - OH_2^+$ and $\equiv Fe - OH^0$ are respectively the protonated positively charged acid site of the surface with two dissociable H^+, and the neutral acid site of the surface with one dissociable H^+. $pK_{a1} = 5.1$ is the intrinsic acidity constant determined by Davis et al. [180] for Fe_3O_4. The binding of MG cations with functional groups such as OH from magnetite surface can be expressed as follows:

$$2 \equiv Fe - OH + Dye^{2+} \longleftrightarrow \equiv (Fe - OH)_2 - Dye^{2+} \tag{4.25}$$

where $\equiv (Fe - OH)_2 - Dye^{2+}$ is a binuclear bonding complex due to hydrogen bonding between MG cations and the surface hydroxyl groups on magnetite NP surfaces.

For the four magnetite NPs, the data provided by FTIR analysis (see the section 4.3.2, Figure 4.3) show that the density of OH groups of $ARM{-}Fe_3O_4$ surface is the highest one, next of $ROS{-}Fe_3O_4$, then of $MAT{-}Fe_3O_4$, and finally of $JUN{-}Fe_3O_4$. As these hydroxyl groups behave as active sites on Fe_3O_4 surfaces, found results showed that MG adsorption yield is more increased on magnetite NP samples that have more OH groups, i.e. more $\equiv FeOH$ active sites.

4.3.6.2 Enhancement of MG Adsorption by Thermocatalysis Process

To assess MG Adsorption enhancement on Magnetite Samples by thermocatalysis, the thermocatalytic experiments were conducted on the residual solutions of MG/Fe_3O_4 after MG adsorption in the first process of MG adsorption in ambient dark conditions, so that to give the overall adsorption yield and capacity after the enhancement, and it also allows the comparison between thermocatalytic activities of the four magnetite samples with the comparison between adsorption yields and capacities before and after applying thermocatalysis.

The thermocatalysis effect on MG adsorption on all four magnetite samples is evaluated by assessing the efficiency of degradation of MG by thermocatalysis in dark conditions in the temperature range from 303.15 K to 318.15 during 20 minutes. Figure 4.12a and Table 4.7 present the comparison of MG adsorption yield and capacity on the four Fe_3O_4 surfaces in the first process of MG adsorption and in the second process in dark conditions under thermocatalysis. The data show that MG adsorption yield and capacity increase with the increase of temperature in all adsorption experiments which confirm the endothermic nature of the adsorption processes as discussed in section 4.3.5.4.

Yields and adsorption capacities are increased as follow (the yield after thermocatalysis is denoted $R_2\%$ and the adsorption capacity q_e^2):

- on $ARM{-}Fe_3O_4$, the yield increased from $R_1\% = 53.42\%$ to $R_2\% = 65.01\%$, and the adsorption capacity increased from $q_e^1 = 15.81$ to $q_e^2 = 18.98\ mg/g$.
- on $ROS{-}Fe_3O_4$, the yield increased from $R_1\% = 51.90\%$ to $R_2\% = 64.09\%$, and the adsorption capacity increased from $q_e^1 = 15.37$ to $q_e^2 = 18.80\ mg/g$.
- on $MAT{-}Fe_3O_4$, the yield increased from $R_1\% = 35.91\%$ to $R_2\% = 63.60\%$, and the adsorption capacity increased from $q_e^1\% = 10.83$ to $q_e^2\% = 18.56\ mg/g$.
- on $JUN{-}Fe_3O_4$, the yield increased from $R_1\% = 19.25\%$ to $R_2\% = 45.59\%$, and the adsorption capacity increased from $q_e^1 = 5.70$ to $q_e^2 = 13.49 mg/g$.

As all experiment conditions are maintained the same for all adsorption experiments, thus, only surface properties are responsible for the adsorption enhancement.

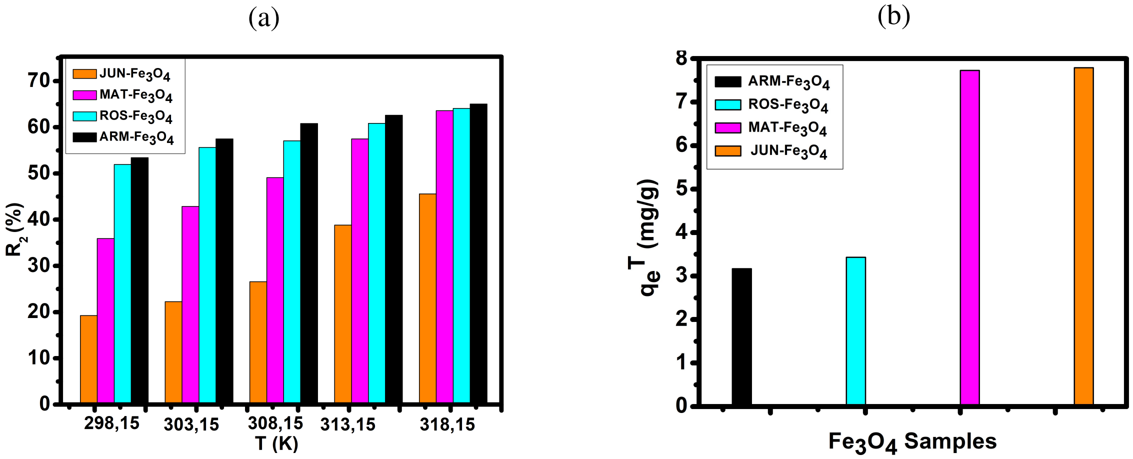

Figure 4.12: (a) MG adsorption yield on Fe_3O_4 surfaces under thermocatalysis in the temperature range from 303.15 K to 318.15 K during 20 minutes in dark conditions, (b) The enhancement in adsorption capacity q_e^T by thermocatalysis in dark conditions at 318.15 k during 20 minutes of MG adsorption on the four Fe_3O_4 surfaces

Table 4.7: The enhancement of MG adsorption yield and capacity on Fe_3O_4 NP surfaces by thermocatalysis in the second process of the adsorption in dark conditions

Sample	298.15K		303.15K		308.15K		313.15K		318.15K	
	q_e^1 (mg/g)	$R_1\%$	q_e^2 (mg/g)	$R_2\%$	q_e^2 (mg/g)	$R_2\%$	q_e^2 (mg/g)	$R_2\%$	q_e^2 (mg/g)	$R_2\%$
$ARM-Fe_3O_4$	15.81	53.42	17.01	57.48	18.00	60.81	18.53	62.61	18.98	65.01
$ROS-Fe_3O_4$	15.37	51.90	16.32	55.64	16.75	57.09	17.81	60.83	18.80	64.09
$MAT-Fe_3O_4$	10.83	35.91	12.69	42.88	14.53	49.10	17.01	57.48	18.56	63.60
$JUN-Fe_3O_4$	05.70	19.25	06.59	22.25	07.87	26.58	11.49	38.83	13.49	45.59

The tendency of adsorption capacities and yields on the four magnetite NP samples is the same in the first process of MG adsorption and in the second process of MG adsorption under thermocatalysis. In first process of MG adsorption, the highest adsorption capacity was on $ARM-Fe_3O_4$, then on $ROS-Fe_3O_4$, next on $MAT-Fe_3O_4$, and finally on $JUN-Fe_3O_4$ NPs. After the exposition of MG/Fe_3O_4 systems to heat in 303.15 k during 20 minutes, the order of adsorption capacities was the same, where the highest adsorption capacity was on $ARM-Fe_3O_4$, then on $ROS-Fe_3O_4$, next on $MAT-Fe_3O_4$, and finally on $JUN-Fe_3O_4$ NP surfaces. When further exposing MG/Fe_3O_4 systems to heat in different temperatures 308.15, 313.15, and 318.15 K during 20 minutes, the adsorption capacities of all four magnetite samples still increased in the same order.

As it is shown in Figure 4.12b, it is clear that there is a difference in adsorption capacities after thermocatalysis uniquely, denoted q_e^T ($q_e^T = q_e^2 - q_e^1$ represents the enhancement in adsorption capacity by thermocatalysis calculated by the difference between q_e^1; adsorption capacity in the first process of MG adsorption and q_e^2; the overall adsorption capacity after applying thermocatalysis at 318.15 k during 20 minutes). Figure 4.12b presents q_e^T for the four MG/Fe_3O_4 systems. These adsorption capacities are useful to elucidate the enhancement in MG adsorption by thermocatalysis. It shows that q_e^T is the highest one on $JUN{-}Fe_3O_4$ (7.79 mg/g) and the lowest one on $ARM{-}Fe_3O_4$ (3.17 mg/g). This indicates that thermocatalytic activity of $JUN{-}Fe_3O_4$ is the highest one and that of $ARM{-}Fe_3O_4$ is the lowest one. As all experiment conditions are maintained the same for all adsorption experiments on all four magnetite samples, so, only magnetite surface properties are responsible for the adsorption enhancement by the thermocatalysis process.

From Figure 4.12b and Table 4.7, it is remarked that the increase in q_e^T is accompanied by the increase in ΔS^0 in all $MG{-}Fe_3O_4$ systems (detailed in Section 4.3.5.4). This confirms that the increase in q_e^T has resulted from the change in surface structure [178]. Thus, the maximum changes occurred in structural surface of $JUN{-}Fe_3O_4$ NP, and the minimum changes occurred in structural surface of $ARM{-}Fe_3O_4$ NP.

4.3.6.3 Enhancement of MG Adsorption by Photocatalysis Process

To assess MG Adsorption enhancement by photocatalysis, the photocatalytic experiments were conducted on MG/Fe_3O_4 residual solutions after thermocatalytic experiments, so that to give the overall adsorption yields and capacities after the enhancement by photocatalysis and allow the comparison between photocatalytic activities of the four magnetite samples with the comparison between adsorption yields and capacities before and after applying photocatalysis. The impact of the photocatalysis process on MG adsorption on all four magnetite samples is evaluated by assessing the efficiency of photodegradation of MG under UV irradiation (365 nm) in the time range from 60 to 240 minutes in ambient conditions.

The variation of MG adsorption yield, as well as adsorption capacity by photocatalysis, is illustrated in Table 4.8 and Figure 4.13a. They show that MG adsorption capacities and yields on the four magnetite surfaces are enhanced by photocatalysis however with different remarkable differences. Table 4.8 and Figure 4.13a show a remarkable difference when comparing adsorption results on the four magnetite samples before applying photocatalysis and after 240 minutes of exposure to UV irradiation in ambient conditions, whereas, MG adsorption yield and adsorption capacity are varied as follow (the yield after applying photocatalysis is denoted $R_3\%$ and the adsorption capacity q_e^3):

- on $ARM{-}Fe_3O_4$ the yield increased from $R_2\% = 65.01\%$ to $R_3\% = 71.71\%$, and the adsorption capacity increased from $q_e^2 = 18.98$ to $q_e^3 = 21.23\ mg/g$.
- on $ROS{-}Fe_3O_4$ the yield increased from $R_2\% = 64.09\%$ to $R_3\% = 72.07\%$, and the adsorption capacity increased from $q_e^2 = 18.80$ to $q_e^3 = 21.33\ mg/g$.
- on $MAT{-}Fe_3O_4$ the yield increased from $R_2\% = 63.60\%$ to $R_3\% = 72.97\%$, and the adsorption capacity increased from $q_e^2 = 18.56$ to $q_e^3 = 21.60\ mg/g$.
- on $JUN{-}Fe_3O_4$ the yield increased from $R_2\% = 45.59\%$ to $R_3\% = 75.23\%$,and the adsorption capacity increased from $q_e^2 = 13.49$ to $q_e^3 = 22.27\ mg/g$.

In first process of MG adsorption, the highest adsorption capacity was on $ARM{-}Fe_3O_4$, then on $ROS{-}Fe_3O_4$, next on $MAT{-}Fe_3O_4$, and finally on $JUN{-}Fe_3O_4$ NPs. Whereas, after exposition of MG/Fe_3O_4 systems to UV irradiation during 60 minutes, the order of adsorption capacities was inverted, where the highest adsorption capacity was on $JUN{-}Fe_3O_4$, then on $MAT{-}Fe_3O_4$, next on $ROS{-}Fe_3O_4$, and finally on $ARM{-}Fe_3O_4$ NPs. When further exposing MG/Fe_3O_4 systems to UV irradiation during 120, 180, and 240 minutes, the adsorption capacities of all four magnetite samples still increased with the same order.

As shown in Figure 4.13b, it is remarked that there is a clear difference between adsorption capacities under photocatalysis uniquely denoted q_e^P ($q_e^P = q_e^3 - q_e^2$ represents the enhancement in adsorption by photocatalysis, it is calculated from the differences between the overall adsorption capacity q_e^3 in the third process of the adsorption after applying the photocatalysis during 240 minutes, and adsorption capacity q_e^2 in the second process of MG adsorption after applying the thermocatalysis at 318.15 k during 20 minutes), for the four MG/Fe_3O_4 systems. These q_e^P are useful to elucidate MG adsorption enhancement by photocatalysis. It shows that the highest one is that of $JUN{-}Fe_3O_4$ (9.48 mg/g) and the lowest one is that of $ARM{-}Fe_3O_4$ (2.27 mg/g). This indicates that photocatalytic activity of $JUN{-}Fe_3O_4$ is the highest one and that of $ARM{-}Fe_3O_4$ is the lowest one. As all experiment conditions are maintained the same for all adsorption experiments on all four magnetite samples, so, only magnetite surface properties are responsible for adsorption enhancement by the photocatalysis process.

Table 4.8: Enhancement of adsorption yield and capacity of MG on Fe_3O_4 surfaces by photocatalysis in ambient conditions

Sample	0 min		60 min		120 min		180 min		240 min	
	q_e^2 (mg/g)	$R_2\%$	q_e^3 (mg/g)	$R_3\%$	q_e^3 (mg/g)	$R_3\%$	q_e^3 (mg/g)	$R_3\%$	q_e^3 (mg/g)	$R_3\%$
$ARM-Fe_3O_4$	18.98	65.01	19.31	65.23	19.44	65.68	20.45	69.10	21.23	71.71
$ROS-Fe_3O_4$	18.80	64.09	19.33	65.32	19.68	66.49	20.64	69.73	21.33	72.07
$MAT-Fe_3O_4$	18.56	63.60	19.34	65.32	19.97	67.48	20.69	69.91	21.60	72.98
$JUN-Fe_3O_4$	13.49	45.52	20.24	68.38	20.93	70.72	21.44	72.44	22.97	75.23

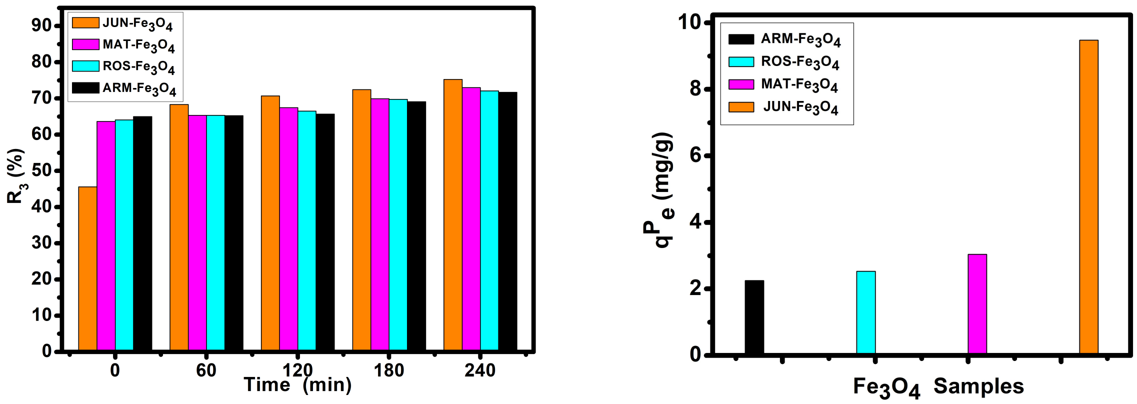
(a)

(b)

Figure 4.13: (a) The enhanced MG adsorption yields on Fe_3O_4 samples by photocatalysis in ambient conditions, (b) The enhancement in MG adsorption q_e^P by photocatalysis in ambient conditions during 240 minutes of MG adsorption on the four Fe_3O_4 surfaces

4.3.7 Influence of Mediating Plant Extract on Preferential and Enhanced MG Adsorption on Magnetite Surfaces

The analysis of MG adsorption in dark ambient conditions results showed that MG was differently adsorbed on the four magnetite surfaces (see Table 4.6). When comparing OH groups density on magnetite surfaces (according to FTIR spectra analyzed in Section 4.3.2), it is found that MG adsorption is more preferred on magnetite surfaces that have more OH groups. The adsorption yield was the highest one on $ARM-Fe_3O_4$ surface, next on $ROS-Fe_3O_4$, then on $MAT-Fe_3O_4$, and finally on $JUN-Fe_3O_4$ and their mediating plant extract have respectively an acidic pH of: 5.25, 5.05, 4.63, and 3.69. Therefore, one can conclude that plant extract pH has a clear effect on OH groups density on magnetite surfaces and consequently on preferential adsorption of MG. Thus, the decrease in mediating plant extract's acidity led to the increase in MG adsorption on greenly synthesised magnetite NPs.

Furthermore, found results showed that the particle sizes of magnetite samples vary with the variation of plant extract mediated in their green synthesis. It is found that particle sizes of $JUN-Fe_3O_4$, $MAT-Fe_3O_4$, $ROS-Fe_3O_4$, and $ARM-Fe_3O_4$ NPs were respectively 29.27, 33.13, 39.89 and 41.49 nm, and their mediating extracts acidic pH were respectively 3.69, 4.63, 5.05, and 5.25. Therefore the particle size decreases with the increase of plant extract's acidity. This result is in agreement with that found by Makarov et al. [43]. Moreover, direct band gap energies of $JUN{-}Fe_3O_4$, $MAT{-}Fe_3O_4$, $ROS{-}Fe_3O_4$, and $ARM{-}Fe_3O_4$ NPs are respectively 2.97, 2.95, 2.94, and 2.87. The smaller crystallite size of Fe_3O_4 respects the higher band gap energy value as proof of the quantum size effect. So, The decrease of particle size leads to an increase in band gap energy. This result is in agreement with that reported by Singh et al. [181]. Therefore, one can conclude that band gap energy increases with the increase of plant extract's acidity.

The photo- and thermocatalysis in the adsorption process are controlled by the photo- and thermogenerated electron/hole pairs which exhibit a strong tendency to recombine. Electron/hole pairs recombination lifetime influences the photo- and thermocatalytic activities efficiency of the catalyst [148], [150], [151]. Found results showed that thermo- and photocatalytic activities of magnetite samples differ according to mediating plant extract's acidity. q_e^P and q_e^T are the highest on $JUN{-}Fe_3O_4$, next on $MAT{-}Fe_3O_4$, then on $ROS{-}Fe_3O_4$, and finally on $ARM{-}Fe_3O_4$ NPs (graphically presented in Figure 4.14). This indicates that the recombination lifetime of electron/hole pairs more decreased on $JUN{-}Fe_3O_4$ surface, next on $MAT{-}Fe_3O_4$, then on $ROS{-}Fe_3O_4$, and finally on $ARM{-}Fe_3O_4$ NPs. Seeing that the increase in band gap energy further slows electron/hole pairs recombination [165], and band gap energy increases with the increase of plant extract's acidity, thus one can announce that the plant extract has an effect on the recombination lifetime of electron/hole pairs where the recombination of electron/hole pairs is further slowed by the increase of plant extract's acidity. Thus, the thermo- and photocatalysis enhance more MG adsorption yields and capacities on magnetite surfaces that are greenly synthesised from more acidic mediating plant extract. Magnetite NPs greenly synthesised from more acidic mediating plant extract showed more thermo- and photocatalytic activities in MG adsorption.

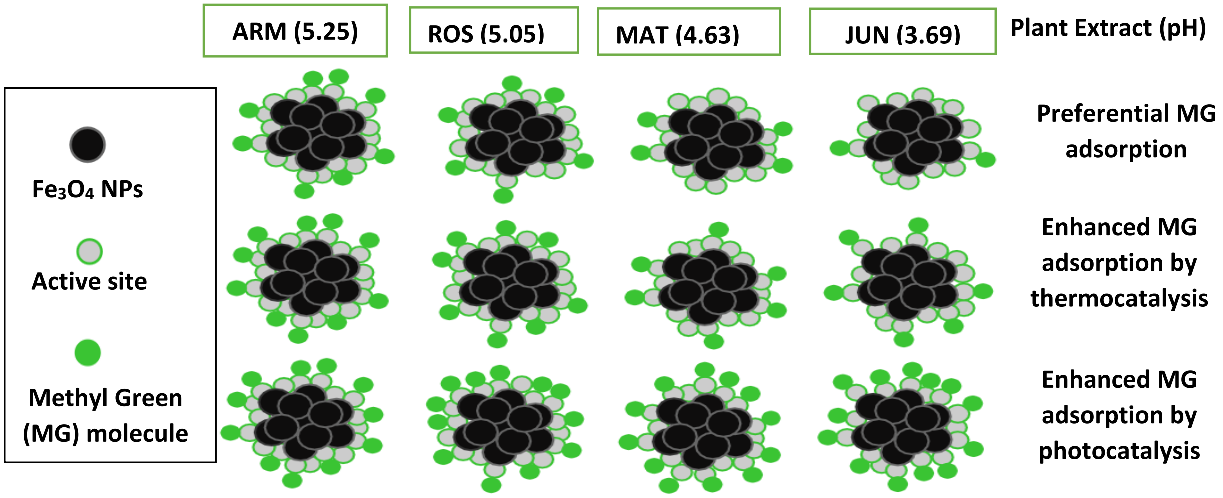

Figure 4.14: Graphical representation of the effect of mediating plant extract's acidity on the thermo- and photocatalysis of magnetite samples. Magnetite NP samples synthesized from less acidic plant extracts have more dense active sites and prefer adsorbing more MG,the increase of plant extract acidity leads to the increase of the thermo- and photocatalytic activities of Fe3O4 NPs.

4.4 Conclusion

The preferential and enhanced MG adsorption by thermo- and photocatalysis on four greenly synthesised magnetite surfaces have been studied by coupling three processes. In the first process, MG adsorption on magnetite surfaces was conducted in dark ambient conditions, whereas in the second and third processes the enhancement by thermo- and photocatalysis were conducted in dark conditions and under UV irradiation (365 nm) in ambient conditions, respectively. All four greenly synthesized magnetite samples are characterized by XRD, SEM, ATR-FTIR, and UV-Vis.

Found results showed that mediating Plant extract's acidity has a clear effect on MG preferential adsorption through its effect on active sites (OH) density on magnetite surface. The decrease in plant extract's acidity leads to the increase of active sites density and hence an increase in MG adsorption yield and capacity. Furthermore, the results showed that mediating plant extract's acidity affects clearly the adsorption enhancement by thermo- and photocatalysis through its effect on band gap energy of synthesized magnetite and consequently on the recombination lifetime of electron/hole pairs after electron excitation. Thus, the band gap energy increases with the increase of plant extract's acidity, and the recombination lifetime of electron/hole pairs is further slowed by the increase of plant extract's acidity. Therefore, the thermo- and photocatalysis enhance more MG adsorption yield and capacity on magnetite surface greenly synthesised from more acidic mediating plant extract. So, magnetite NPs greenly synthesised from more acidic mediating plant extract showed more thermo- and photocatalytic activities in MG adsorption.

In the first process of MG adsorption, the pseudo-first-order and pseudo-second-order kinetics of the adsorption as well as the intra-particles diffusion mechanism have been analyzed. Found results indicate that in all adsorption processes: the adsorption kinetic followed pseudo-first-order kinetic model, and film diffusion is the step that controlled the adsorption mechanism. In the second process of MG adsorption under thermocatalysis, the adsorption was endothermic and physical in nature. In the third process of MG adsorption under photocatalysis, kinetic was well agreed with the pseudo-first-order model.

General Conclusion

In this thesis, two novel studies have been conducted. The first one investigated how the Ferrous Reducing Antioxidant Potential (FRAP) of aqueous plant extracts FRAP affects Fe^{2+} vacancies formation in greenly synthesized wüstite (Fe_xO) NPs. In the second study, the preferential and enhanced MG adsorption by thermo- and photocatalysis on four greenly synthesised magnetite surfaces have been studied by coupling three processes. In the first process, MG adsorption on magnetite surfaces was conducted in dark ambient conditions, whereas in the second and third processes the enhancement by thermo- and photocatalysis were conducted in dark conditions and under UV irradiation (365 nm) in ambient conditions, respectively. All four greenly synthesized magnetite samples are characterized by XRD, SEM, ATR-FTIR, and UV-vis. After the complete oxidation of the four Fe_xO into Fe_3O_4 NPs under ambient conditions for four months, the four Fe_3O_4 NPs have been used in the second study.

Mediating Plant Extract FRAP Effect on Iron Vacancies Within Greenly Synthesised Wüstite NPs

Wüstite Fe_xO NPs have been greenly synthesized using four different mediating aqueous plant extracts as reducing agents and $FeCl_3$ as a precursor. This study used four aqueous plant extracts as reducing agents with $FeCl_3$ as a precursor to synthesize Fe_xO NPs. The plants dealt with in this study are Rosemarinus officinalis.(L), Juniperus Phoenicia.(L), Matricaria Pubescens.(L), and Artemisia herba-alba.(L), and their extracts acidic pH were respectively; 5.25, 5.05, 4.63, and 3.69. All synthesized iron oxide samples are characterized by XRD, SEM, ATR-FTIR, and UV-Vis. Characterization of synthesized samples shows that wüstite is formed with different iron cation vacancies and grain sizes. For this reason, the effect of FRAP power of aqueous plant extracts on Fe^{2+} vacancies formation within synthesised wüstite NPs has been considered. It is found that iron cation vacancies formation within wüstite NPs are clearly impacted by the FRAP power of mediating plant aqueous extract. Indeed, the increase in the FRAP leads to a decrease in Fe^{2+} defects and consequently an increase in the grain size. This leads to proclaim that FRAP of plant extract provides a preconceived idea about cation vacancies within wüstite NPs structure. From thermodynamic study, FRAP power also impacts $\Delta G^0_{fF_eO}(x)$ of Fe_xO formation, where the decrease in FRAP makes $\Delta G^0_{fF_eO}(x)$ more negative.

Mediating Plant Extract's Acidity Effect on The Preferential and Enhanced MG Adsorption by Thermo- and Photocatalysis

Found results showed that the mediating Plant extract's acidity has a clear effect on MG preferential adsorption through its effect on active sites density on magnetite surface. The decrease in plant extract acidity leads to the increase of active sites density and hence an increase in MG adsorption yield and capacity.

Furthermore, the results showed that the mediating plant extract's acidity affects clearly the adsorption enhancement by thermo- and photocatalysis through its effect on band gap energy of synthesized magnetite and consequently on the recombination lifetime of electron/hole pairs after electron excitation. Thus, the band gap energy increases with the increase of the mediating plant extract's acidity, and the recombination lifetime of electron/hole pairs is further slowed by the increase of plant extract acidity. Therefore, the thermo- and photocatalysis enhance more MG adsorption yield and capacity on magnetite surface that greenly synthesised from more acidic mediating plant extract. So, magnetite NPs greenly synthesised from more acidic mediating plant extract showed more thermo- and photocatalytic activities in MG adsorption.

In the first process of MG adsorption, the pseudo-first-order and pseudo-second-order kinetics of the adsorption as well as the intra-particles diffusion mechanism have been analyzed. Found results indicate that in all adsorption processes: the adsorption kinetic followed pseudo-first-order kinetic model, and film diffusion is the step that controlled the adsorption mechanism. In the second process of MG adsorption under thermocatalysis, the adsorption was endothermic and physical in nature. In the third process of MG adsorption under photocatalysis, kinetic was well agreed with the pseudo-first-order model.

References

[1] R. M. Cornell and U. Schwertmann, *The iron oxides: structure, properties, reactions, occurrences and uses*. John Wiley & Sons, 2003.

[2] A. I. Martinez, M. Garcia-Lobato, and D. L. Perry, "Study of the properties of iron oxide nanostructures," *Research in Nanotechnology Developments*, vol. 19, pp. 184–193, 2009.

[3] L. Néel, "Essai d'interprétation des propriétés magnétiques du sesquioxyde de fer rhomboédrique," in *Annales de Physique*, vol. 12, 1949, pp. 249–268.

[4] L.-G. Liu, "The high-pressure phases of fesio3 with implications for fe2sio4 and feo," *Earth and Planetary Science Letters*, vol. 33, no. 1, pp. 101–106, 1976.

[5] M. S. Al-Ruqeishi, T. Mohiuddin, and L. K. Al-Saadi, "Green synthesis of iron oxide nanorods from deciduous omani mango tree leaves for heavy oil viscosity treatment," *Arabian Journal of Chemistry*, vol. 12, no. 8, pp. 4084–4090, 2019.

[6] A. M. El-Nahas, T. A. Salaheldin, T. Zaki, H. H. El-Maghrabi, A. M. Marie, S. M. Morsy, and N. K. Allam, "Functionalized cellulose-magnetite nanocomposite catalysts for efficient biodiesel production," *Chemical Engineering Journal*, vol. 322, pp. 167–180, 2017.

[7] L. Yu, S. Xi, C. Wei, W. Zhang, Y. Du, Q. Yan, and Z. Xu, "Superior lithium storage properties of β-feooh," *Advanced Energy Materials*, vol. 5, no. 6, p. 1 401 517, 2015.

[8] M. Mohapatra and S. Anand, "Synthesis and applications of nano-structured iron oxides/hydroxides–a review," *International Journal of Engineering, Science and Technology*, vol. 2, no. 8, 2010.

[9] O. P. Bolade, A. B. Williams, and N. U. Benson, "Green synthesis of iron-based nanomaterials for environmental remediation: A review," *Environmental Nanotechnology, Monitoring & Management*, vol. 13, p. 100 279, 2020.

[10] P. N. Dave and L. V. Chopda, "Application of iron oxide nanomaterials for the removal of heavy metals," *Journal of Nanotechnology*, vol. 2014, 2014.

[11] D. Rawtani, N. Khatri, S. Tyagi, and G. Pandey, "Nanotechnology-based recent approaches for sensing and remediation of pesticides," *Journal of Environmental Management*, vol. 206, pp. 749–762, 2018.

[12] A. Mohseni-Bandpi, T. J. Al-Musawi, E. Ghahramani, M. Zarrabi, S. Mohebi, and S. A. Vahed, "Improvement of zeolite adsorption capacity for cephalexin by coating with magnetic fe3o4 nanoparticles," *Journal of Molecular Liquids*, vol. 218, pp. 615–624, 2016.

[13] E. Tanis, K. Hanna, and E. Emmanuel, "Experimental and modeling studies of sorption of tetracycline onto iron oxides-coated quartz," *Colloids and Surfaces A: Physicochemical and Engineering Aspects*, vol. 327, no. 1-3, pp. 57–63, 2008.

[14] S. Tyagi, D. Rawtani, N. Khatri, and M. Tharmavaram, "Strategies for nitrate removal from aqueous environment using nanotechnology: A review," *Journal of Water Process Engineering*, vol. 21, pp. 84–95, 2018.

[15] A. Khodabakhshi, M. M. Amin, and M. Mozaffari, "Synthesis of magnetite nanoparticles and evaluation of its efficiency for arsenic removal from simulated industrial wastewater," *Iranian Journal of Environmental Health Science & Engineering*, vol. 8, no. 3, pp. 189–200, 2011.

[16] B. Saha, S. Das, J. Saikia, and G. Das, "Preferential and enhanced adsorption of different dyes on iron oxide nanoparticles: A comparative study," *The Journal of Physical Chemistry C*, vol. 115, no. 16, pp. 8024–8033, 2011.

[17] R. Kant, "Textile dyeing industry an environmental hazard," 2011.

[18] H. Ali, "Biodegradation of synthetic dyes—a review," *Water, Air, & Soil Pollution*, vol. 213, no. 1, pp. 251–273, 2010.

[19] M. Amin, A. Alazba, and U. Manzoor, "A review of removal of pollutants from water/wastewater using different types of nanomaterials," *Advances in Materials Science and Engineering*, vol. 2014, 2014.

[20] M. M. Khin, A. S. Nair, V. J. Babu, R. Murugan, and S. Ramakrishna, "A review on nanomaterials for environmental remediation," *Energy & Environmental Science*, vol. 5, no. 8, pp. 8075–8109, 2012.

[21] A. M. Elgarahy, K. Z. Elwakeel, A. Akhdhar, and M. F. Hamza, “Recent advances in greenly synthesized nanoengineered materials for water/wastewater remediation: An overview,” *Nanotechnology for Environmental Engineering*, vol. 6, no. 1, pp. 1–24, 2021.

[22] A. A. Yaqoob, T. Parveen, K. Umar, and M. N. Mohamad Ibrahim, “Role of nanomaterials in the treatment of wastewater: A review,” *Water*, vol. 12, no. 2, p. 495, 2020.

[23] S. Pirillo, M. L. Ferreira, and E. H. Rueda, “Adsorption of alizarin, eriochrome blue black r, and fluorescein using different iron oxides as adsorbents,” *Industrial & engineering chemistry research*, vol. 46, no. 24, pp. 8255–8263, 2007.

[24] S. Pirillo, L. Cornaglia, M. L. Ferreira, and E. H. Rueda, “Removal of fluorescein using different iron oxides as adsorbents: Effect of ph,” *Spectrochimica Acta Part A: Molecular and Biomolecular Spectroscopy*, vol. 71, no. 2, pp. 636–643, 2008.

[25] B. Hentschel, “Stoichiometric feo as metastable intermediate of the decomposition of wustite at 225 c,” *Zeitschrift für Naturforschung A*, vol. 25, no. 12, pp. 1996–1997, 1970.

[26] C.-J. Chen, R.-K. Chiang, H.-Y. Lai, and C.-R. Lin, “Characterization of monodisperse wustite nanoparticles following partial oxidation,” *The Journal of Physical Chemistry C*, vol. 114, no. 10, pp. 4258–4263, 2010.

[27] H. Wriedt, “The fe-o (iron-oxygen) system,” *Journal of phase equilibria*, vol. 12, no. 2, pp. 170–200, 1991.

[28] C. Catlow and B. Fender, “Calculations of defect clustering in fe1-xo,” *Journal of Physics C: Solid State Physics*, vol. 8, no. 20, p. 3267, 1975.

[29] R. M. Hazen and R. Jeanloz, “Wüstite (fe1-x o): A review of its defect structure and physical properties,” *Reviews of Geophysics*, vol. 22, no. 1, pp. 37–46, 1984.

[30] A. Cheetham, V. Fender, and R. Taylor, “High temperature neutron diffraction study of fe1-xo,” *Journal of Physics C: Solid State Physics*, vol. 4, no. 14, p. 2160, 1971.

[31] C. McCammon and L.-g. Liu, “The effects of pressure and temperature on nonstoichiometric wüstite, fe x o: The iron-rich phase boundary,” *Physics and Chemistry of Minerals*, vol. 10, no. 3, pp. 106–113, 1984.

[32] R. A. Giddings and R. S. Gordon, “Review of oxygen activities and phase boundaries in wustite as determined by electromotive-force and gravimetric methods,” *Journal of the American Ceramic Society*, vol. 56, no. 3, pp. 111–116, 1973.

[33] F. Koch and J. Cohen, “The defect structure of fe1- xo,” *Acta Crystallographica Section B: Structural Crystallography and Crystal Chemistry*, vol. 25, no. 2, pp. 275–287, 1969.

[34] L. Minervini and R. W. Grimes, “Defect clustering in wüstite,” *Journal of Physics and Chemistry of Solids*, vol. 60, no. 2, pp. 235–245, 1999.

[35] F. X. Redl, C. T. Black, G. C. Papaefthymiou, R. L. Sandstrom, M. Yin, H. Zeng, C. B. Murray, and S. P. O’Brien, “Magnetic, electronic, and structural characterization of non-stoichiometric iron oxides at the nanoscale,” *Journal of the American Chemical Society*, vol. 126, no. 44, pp. 14 583–14 599, 2004.

[36] H. Bowen, D. Adler, and B. Auker, “Electrical and optical properties of feo,” *Journal of Solid State Chemistry*, vol. 12, no. 3-4, pp. 355–359, 1975.

[37] P. Liu, W. Cai, and H. Zeng, “Fabrication and size-dependent optical properties of feo nanoparticles induced by laser ablation in a liquid medium,” *The Journal of Physical Chemistry C*, vol. 112, no. 9, pp. 3261–3266, 2008.

[38] F. Schrettle, C. Kant, P. Lunkenheimer, F. Mayr, J. Deisenhofer, and A. Loidl, “Wüstite: Electric, thermodynamic and optical properties of feo,” *The European Physical Journal B*, vol. 85, no. 5, p. 164, 2012.

[39] U. D. Wdowik, P. Piekarz, K. Parlinski, A. M. Oleś, and J. Korecki, “Strong effects of cation vacancies on the electronic and dynamical properties of feo,” *Physical Review B*, vol. 87, no. 12, p. 121 106, 2013.

[40] J. Zhang, “Effect of defects on the elastic properties of wüstite,” *Physical review letters*, vol. 84, no. 3, p. 507, 2000.

[41] U. D. Wdowik, P. Piekarz, P. T. Jochym, K. Parlinski, and A. M. Oleś, “Influence of isolated and clustered defects on electronic and dielectric properties of wüstite,” *Physical Review B*, vol. 91, no. 19, p. 195 111, 2015.

[42] N. A. N. Mohamad, N. A. Arham, J. Jai, and A. Hadi, “Plant extract as reducing agent in synthesis of metallic nanoparticles: A review,” in *Advanced Materials Research*, Trans Tech Publ, vol. 832, 2014, pp. 350–355.

[43] V. V. Makarov, S. S. Makarova, A. J. Love, O. V. Sinitsyna, A. O. Dudnik, I. V. Yaminsky, M. E. Taliansky, and N. O. Kalinina, "Biosynthesis of stable iron oxide nanoparticles in aqueous extracts of hordeum vulgare and rumex acetosa plants," *Langmuir*, vol. 30, no. 20, pp. 5982–5988, 2014.

[44] A. Ebrahiminezhad, A. Zare-Hoseinabadi, A. K. Sarmah, S. Taghizadeh, Y. Ghasemi, and A. Berenjian, "Plant-mediated synthesis and applications of iron nanoparticles," *Molecular biotechnology*, vol. 60, no. 2, pp. 154–168, 2018.

[45] M. Herlekar, S. Barve, and R. Kumar, "Plant-mediated green synthesis of iron nanoparticles," *Journal of Nanoparticles*, vol. 2014, 2014.

[46] R. Herrera-Becerra, C. Zorrilla, and J. A. Ascencio, "Production of iron oxide nanoparticles by a biosynthesis method: An environmentally friendly route," *The Journal of Physical Chemistry C*, vol. 111, no. 44, pp. 16 147–16 153, 2007.

[47] K. M. Kumar, B. K. Mandal, K. S. Kumar, P. S. Reddy, and B. Sreedhar, "Biobased green method to synthesise palladium and iron nanoparticles using terminalia chebula aqueous extract," *Spectrochimica Acta Part A: Molecular and Biomolecular Spectroscopy*, vol. 102, pp. 128–133, 2013.

[48] T. Wang, X. Jin, Z. Chen, M. Megharaj, and R. Naidu, "Green synthesis of fe nanoparticles using eucalyptus leaf extracts for treatment of eutrophic wastewater," *Science of the total environment*, vol. 466, pp. 210–213, 2014.

[49] D. Patiño-Ruiz, L. Sánchez-Botero, L. Tejeda-Benitez, J. Hinestroza, and A. Herrera, "Green synthesis of iron oxide nanoparticles using cymbopogon citratus extract and sodium carbonate salt: Nanotoxicological considerations for potential environmental applications," *Environmental Nanotechnology, Monitoring & Management*, vol. 14, p. 100 377, 2020.

[50] P. Karpagavinayagam and C. Vedhi, "Green synthesis of iron oxide nanoparticles using avicennia marina flower extract," *Vacuum*, vol. 160, pp. 286–292, 2019.

[51] I. Anastopoulos, A. Hosseini-Bandegharaei, J. Fu, A. C. Mitropoulos, and G. Z. Kyzas, "Use of nanoparticles for dye adsorption," *Journal of Dispersion Science and Technology*, vol. 39, no. 6, pp. 836–847, 2018.

[52] R. M. Ali, H. A. Hamad, M. M. Hussein, and G. F. Malash, "Potential of using green adsorbent of heavy metal removal from aqueous solutions: Adsorption kinetics, isotherm,

thermodynamic, mechanism and economic analysis," *Ecological Engineering*, vol. 91, pp. 317–332, 2016.

[53] R. Cornell and U. Schwertmann, "The iron oxides: Structures, properties, reactions, occurrences and uses," *VCH Verlagsgesellshaft GMBH, Weinheim, Germany*, pp. 533–559, 1996.

[54] S. Pirillo, M. L. Ferreira, and E. H. Rueda, "The effect of ph in the adsorption of alizarin and eriochrome blue black r onto iron oxides," *Journal of hazardous materials*, vol. 168, no. 1, pp. 168–178, 2009.

[55] C. Xiao, H. Li, Y. Zhao, X. Zhang, and X. Wang, "Green synthesis of iron nanoparticle by tea extract (polyphenols) and its selective removal of cationic dyes," *Journal of Environmental Management*, vol. 275, p. 111 262, 2020.

[56] T. Madrakian, A. Afkhami, and M. Ahmadi, "Adsorption and kinetic studies of seven different organic dyes onto magnetite nanoparticles loaded tea waste and removal of them from wastewater samples," *Spectrochimica Acta Part A: Molecular and Biomolecular Spectroscopy*, vol. 99, pp. 102–109, 2012.

[57] C.-H. Weng, Y.-T. Lin, C.-L. Yeh, and Y. Sharma, "Magnetic fe3o4 nanoparticles for adsorptive removal of acid dye (new coccine) from aqueous solutions," *Water Science and Technology*, vol. 62, no. 4, pp. 844–851, 2010.

[58] K. W. Borth, C. W. Galdino, V. de Carvalho Teixeira, and F. J. Anaissi, "Iron oxide nanoparticles obtained from steel waste recycling as a green alternative for congo red dye fast adsorption," *Applied Surface Science*, vol. 546, p. 149 126, 2021.

[59] H. Hongping, Y. Zhong, X. Liang, T. Wei, Z. Jianxi, and C. Y. Wang, "Natural magnetite: An efficient catalyst for the degradation of organic contaminant," *Scientific reports*, vol. 5, no. 1, pp. 1–10, 2015.

[60] L. Huang, X. Weng, Z. Chen, M. Megharaj, and R. Naidu, "Green synthesis of iron nanoparticles by various tea extracts: Comparative study of the reactivity," *Spectrochimica Acta Part A: Molecular and Biomolecular Spectroscopy*, vol. 130, pp. 295–301, 2014.

[61] D. T. C. Nguyen, H. H. Dang, D.-V. N. Vo, L. G. Bach, T. D. Nguyen, and T. Van Tran, "Biogenic synthesis of mgo nanoparticles from different extracts (flower, bark, leaf) of tecoma stans (l.) and their utilization in selected organic dyes treatment," *Journal of Hazardous Materials*, vol. 404, p. 124 146, 2021.

[62] T. Islam, C. Peng, I. Ali, and I. A. Abbasi, "Comparative study on anionic and cationic dyes removal from aqueous solutions using different plant mediated magnetic nano particles," 2018.

[63] R. Gusain, K. Gupta, P. Joshi, and O. P. Khatri, "Adsorptive removal and photocatalytic degradation of organic pollutants using metal oxides and their composites: A comprehensive review," *Advances in colloid and interface science*, vol. 272, p. 102 009, 2019.

[64] H. Chen, J. Ku, and L. Wang, "Thermal catalysis under dark ambient conditions in environmental remediation: Fundamental principles, development, and challenges," *Chinese Journal of Catalysis*, vol. 40, no. 8, pp. 1117–1134, 2019.

[65] R. Wu, J.-H. Liu, L. Zhao, X. Zhang, J. Xie, B. Yu, X. Ma, S.-T. Yang, H. Wang, and Y. Liu, "Hydrothermal preparation of magnetic fe3o4@ c nanoparticles for dye adsorption," *Journal of Environmental Chemical Engineering*, vol. 2, no. 2, pp. 907–913, 2014.

[66] J. Fan, W. Cai, and J. Yu, "Adsorption of n719 dye on anatase tio2 nanoparticles and nanosheets with exposed (001) facets: Equilibrium, kinetic, and thermodynamic studies," *Chemistry–An Asian Journal*, vol. 6, no. 9, pp. 2481–2490, 2011.

[67] A. Farghali, M. Bahgat, W. El Rouby, and M. Khedr, "Decoration of mwcnts with cofe2o4 nanoparticles for methylene blue dye adsorption," *Journal of solution chemistry*, vol. 41, no. 12, pp. 2209–2225, 2012.

[68] Y.-L. Ge, Y.-F. Zhang, Y. Yang, S. Xie, Y. Liu, T. Maruyama, Z.-Y. Deng, and X. Zhao, "Enhanced adsorption and catalytic degradation of organic dyes by nanometer iron oxide anchored to single-wall carbon nanotubes," *Applied Surface Science*, vol. 488, pp. 813–826, 2019.

[69] M. Elhadj, A. Samira, T. Mohamed, F. Djawad, A. Asma, and N. Djamel, "Removal of basic red 46 dye from aqueous solution by adsorption and photocatalysis: Equilibrium, isotherms, kinetics, and thermodynamic studies," *Separation Science and Technology*, vol. 55, no. 5, pp. 867–885, 2020.

[70] B. Kumar, K. Smita, L. Cumbal, A. Debut, S. Galeas, and V. H. Guerrero, "Phytosynthesis and photocatalytic activity of magnetite (fe3o4) nanoparticles using the andean blackberry leaf," *Materials Chemistry and Physics*, vol. 179, pp. 310–315, 2016.

[71] K. D. Sirdeshpande, A. Sridhar, K. M. Cholkar, and R. Selvaraj, "Structural characterization of mesoporous magnetite nanoparticles synthesized using the leaf extract of callian-

dra haematocephala and their photocatalytic degradation of malachite green dye," *Applied Nanoscience*, vol. 8, no. 4, pp. 675–683, 2018.

[72] T. Kusova, I. Yamanovskaya, N. Kopeikina, A. Kraev, and A. Agafonov, "Production of mesoporous materials based on titanium dioxide modified with magnetite particles with high adsorption capacity and photocatalytic activity," *Inorganic Materials: Applied Research*, vol. 12, no. 2, pp. 570–575, 2021.

[73] V. Jassal, U. Shanker, and S. Gahlot, "Green synthesis of some iron oxide nanoparticles and their interaction with 2-amino, 3-amino and 4-aminopyridines," *Materials Today: Proceedings*, vol. 3, no. 6, pp. 1874–1882, 2016.

[74] F. Mai, C. Chen, J. Chen, and S. Liu, "Photodegradation of methyl green using visible irradiation in zno suspensions: Determination of the reaction pathway and identification of intermediates by a high-performance liquid chromatography–photodiode array-electrospray ionization-mass spectrometry method," *Journal of Chromatography A*, vol. 1189, no. 1-2, pp. 355–365, 2008.

[75] A. Kumar and G. Pandey, "A review on the factors affecting the photocatalytic degradation of hazardous materials," *Mater. Sci. Eng. Int. J*, vol. 1, no. 3, pp. 1–10, 2017.

[76] A. Masudi, G. E. Harimisa, N. A. Ghafar, and N. W. C. Jusoh, "Magnetite-based catalysts for wastewater treatment," *Environmental Science and Pollution Research*, vol. 27, no. 5, pp. 4664–4682, 2020.

[77] A. Khataee and M. B. Kasiri, "Photocatalytic degradation of organic dyes in the presence of nanostructured titanium dioxide: Influence of the chemical structure of dyes," *Journal of Molecular Catalysis A: Chemical*, vol. 328, no. 1-2, pp. 8–26, 2010.

[78] M. Fathinia, A. Khataee, M. Zarei, and S. Aber, "Comparative photocatalytic degradation of two dyes on immobilized tio2 nanoparticles: Effect of dye molecular structure and response surface approach," *Journal of Molecular Catalysis A: Chemical*, vol. 333, no. 1-2, pp. 73–84, 2010.

[79] N. Xu, Z. Shi, Y. Fan, J. Dong, J. Shi, and M. Z.-C. Hu, "Effects of particle size of tio2 on photocatalytic degradation of methylene blue in aqueous suspensions," *Industrial & Engineering Chemistry Research*, vol. 38, no. 2, pp. 373–379, 1999.

[80] R. Ullah and J. Dutta, "Photocatalytic degradation of organic dyes with manganese-doped zno nanoparticles," *Journal of Hazardous materials*, vol. 156, no. 1-3, pp. 194–200, 2008.

[81] H. Rafaie, R. Nor, M. Azmina, N. Ramli, and R. Mohamed, “Decoration of zno microstructures with ag nanoparticles enhanced the catalytic photodegradation of methylene blue dye,” *Journal of environmental chemical engineering*, vol. 5, no. 4, pp. 3963–3972, 2017.

[82] B. Mounir, M.-N. Pons, O. Zahraa, A. Yaacoubi, and A. Benhammou, “Discoloration of a red cationic dye by supported tio2 photocatalysis,” *Journal of Hazardous materials*, vol. 148, no. 3, pp. 513–520, 2007.

[83] X. Cai, B. Han, S. Deng, Y. Wang, C. Dong, Y. Wang, and I. Djerdj, “Hydrothermal growth of zno nanorods on zn substrates and their application in degradation of azo dyes under ambient conditions,” *CrystEngComm*, vol. 16, no. 33, pp. 7761–7770, 2014.

[84] C. Noubactep, “The suitability of metallic iron for environmental remediation,” *Environmental Progress & Sustainable Energy*, vol. 29, no. 3, pp. 286–291, 2010.

[85] P. R. Chang, J. Yu, X. Ma, and D. P. Anderson, “Polysaccharides as stabilizers for the synthesis of magnetic nanoparticles,” *Carbohydrate polymers*, vol. 83, no. 2, pp. 640–644, 2011.

[86] B. Kumar, K. Smita, L. Cumbal, and A. Debut, “Biogenic synthesis of iron oxide nanoparticles for 2-arylbenzimidazole fabrication,” *Journal of Saudi Chemical Society*, vol. 18, no. 4, pp. 364–369, 2014.

[87] M. Latorre-Sanchez, A. Primo, and H. Garcia, “Green synthesis of fe 3 o 4 nanoparticles embedded in a porous carbon matrix and its use as anode material in li-ion batteries,” *Journal of Materials Chemistry*, vol. 22, no. 40, pp. 21 373–21 375, 2012.

[88] D. Weller and A. Moser, “Thermal effect limits in ultrahigh-density magnetic recording,” *IEEE Transactions on magnetics*, vol. 35, no. 6, pp. 4423–4439, 1999.

[89] S. K. Panda, I. Aggarwal, H. Kumar, L. Prasad, A. Kumar, A. Sharma, D.-V. N. Vo, D. Van Thuan, and V. Mishra, “Magnetite nanoparticles as sorbents for dye removal: A review,” *Environmental Chemistry Letters*, pp. 1–39, 2021.

[90] A. Jawed, S. Sharma, A. K. Golder, and L. M. Pandey, “Plant-polyphenol-mediated synthesis of iron oxide nanomaterials for heavy metal removal: A review,” *New Trends in Removal of Heavy Metals from Industrial Wastewater*, pp. 115–129, 2021.

[91] C. Catlow, “Nonstoichiometric oxides, edited by ot sorenson academic,” *New York*, pp. 61–98, 1981.

[92] S. Mrowec and A. Podgorecka, "Defect structure and transport properties of non-stoichiometric ferrous oxide," *Journal of materials science*, vol. 22, no. 12, pp. 4181–4189, 1987.

[93] C. Peters and M. Dekkers, "Selected room temperature magnetic parameters as a function of mineralogy, concentration and grain size," *Physics and Chemistry of the Earth, Parts A/B/C*, vol. 28, no. 16-19, pp. 659–667, 2003.

[94] A. S. Teja and P.-Y. Koh, "Synthesis, properties, and applications of magnetic iron oxide nanoparticles," *Progress in crystal growth and characterization of materials*, vol. 55, no. 1-2, pp. 22–45, 2009.

[95] R. A. Eggleton and R. W. Fitzpatrick, "New data and a revised structural model for ferrihydrite," *Clays and Clay minerals*, vol. 36, no. 2, pp. 111–124, 1988.

[96] H. Stanjek, "Aluminium-und hydroxylsubstitution in synthetischen und natfirlichen hĩmatiten," *Buch am Erlbach, Germany: Verlag Marie L. Leidorf*, 1991.

[97] G. A. Waychunas, "Crystal chemistry of oxides and oxyhydroxides," *Oxide Minerals*, pp. 11–68, 2018.

[98] S. Kianpour, A. Ebrahiminezhad, M. Mohkam, A. M. Tamaddon, A. Dehshahri, R. Heidari, and Y. Ghasemi, "Physicochemical and biological characteristics of the nanostructured polysaccharide-iron hydrogel produced by microorganism klebsiella oxytoca," *Journal of basic microbiology*, vol. 57, no. 2, pp. 132–140, 2017.

[99] M. Mahdavi, F. Namvar, M. Ahmad, and R. Mohamad, "Green biosynthesis and characterization of magnetic iron oxide (fe3o4) nanoparticles using seaweed (sargassum muticum) aqueous extract," *Molecules*, vol. 18, no. 5, pp. 5954–5964, 2013.

[100] M. Martınez-Cabanas, M. López-Garcıa, J. L. Barriada, R. Herrero, and M. E. S. de Vicente, "Green synthesis of iron oxide nanoparticles. development of magnetic hybrid materials for efficient as (v) removal," *Chemical Engineering Journal*, vol. 301, pp. 83–91, 2016.

[101] M. Jamzad and M. Kamari Bidkorpeh, "Green synthesis of iron oxide nanoparticles by the aqueous extract of laurus nobilis l. leaves and evaluation of the antimicrobial activity," *Journal of Nanostructure in Chemistry*, vol. 10, no. 3, pp. 193–201, 2020.

[102] M. H. Ehrampoush, M. Miria, M. H. Salmani, and A. H. Mahvi, “Cadmium removal from aqueous solution by green synthesis iron oxide nanoparticles with tangerine peel extract,” *Journal of Environmental Health Science and Engineering*, vol. 13, no. 1, pp. 1–7, 2015.

[103] Z. Xiao, M. Yuan, B. Yang, Z. Liu, J. Huang, and D. Sun, “Plant-mediated synthesis of highly active iron nanoparticles for cr (vi) removal: Investigation of the leading biomolecules,” *Chemosphere*, vol. 150, pp. 357–364, 2016.

[104] I. Ali, Z. A. AL-Othman, and A. Alwarthan, “Green synthesis of functionalized iron nano particles and molecular liquid phase adsorption of ametryn from water,” *Journal of Molecular Liquids*, vol. 221, pp. 1168–1174, 2016.

[105] L. Huang, X. Weng, Z. Chen, M. Megharaj, and R. Naidu, “Synthesis of iron-based nanoparticles using oolong tea extract for the degradation of malachite green,” *Spectrochimica Acta Part A: Molecular and Biomolecular Spectroscopy*, vol. 117, pp. 801–804, 2014.

[106] E. C. Njagi, H. Huang, L. Stafford, H. Genuino, H. M. Galindo, J. B. Collins, G. E. Hoag, and S. L. Suib, “Biosynthesis of iron and silver nanoparticles at room temperature using aqueous sorghum bran extracts,” *Langmuir*, vol. 27, no. 1, pp. 264–271, 2011.

[107] D. A. Demirezen, Y. Ş. Yıldız, Ş. Yılmaz, and D. D. Yılmaz, “Green synthesis and characterization of iron oxide nanoparticles using ficus carica (common fig) dried fruit extract,” *Journal of bioscience and bioengineering*, vol. 127, no. 2, pp. 241–245, 2019.

[108] S. Machado, S. Pinto, J. Grosso, H. Nouws, J. T. Albergaria, and C. Delerue-Matos, “Green production of zero-valent iron nanoparticles using tree leaf extracts,” *Science of the Total Environment*, vol. 445, pp. 1–8, 2013.

[109] H. Bhat, *Introduction to crystal growth: principles and practice*. CRC Press, 2014.

[110] W. Bollmann, *Crystal defects and crystalline interfaces*. Springer Science & Business Media, 2012.

[111] W. Roth, “Defects in the crystal and magnetic structures of ferrous oxide,” *Acta Crystallographica*, vol. 13, no. 2, pp. 140–149, 1960.

[112] E. Wetterskog, C.-W. Tai, J. Grins, L. Bergstrom, and G. Salazar-Alvarez, “Anomalous magnetic properties of nanoparticles arising from defect structures: Topotaxial oxidation of fe1–x o— fe3- δo4 core— shell nanocubes to single-phase particles,” *ACS nano*, vol. 7, no. 8, pp. 7132–7144, 2013.

[113] R. Strobel and S. E. Pratsinis, “Direct synthesis of maghemite, magnetite and wustite nanoparticles by flame spray pyrolysis,” *Advanced Powder Technology*, vol. 20, no. 2, pp. 190–194, 2009.

[114] M. Gheisari, M. Mozafari, M. Niyaifar, J. Amighian, and R. Soleimani, “Observation of small exchange bias in defect wüstite (fe 0.93 o) nanoparticles,” *Journal of superconductivity and novel magnetism*, vol. 26, no. 2, pp. 237–242, 2013.

[115] M. Hiramoto, N. Okinaka, and T. Akiyama, “Self-propagating high-temperature synthesis of nonstoichiometric wüstite,” *Journal of alloys and compounds*, vol. 520, pp. 59–64, 2012.

[116] J.-C. Park, D. Kim, C.-S. Lee, and D.-K. Kim, “A new synthetic route to wüstite,” *BULLETIN-KOREAN CHEMICAL SOCIETY*, vol. 20, pp. 1005–1009, 1999.

[117] M. Yin, Z. Chen, B. Deegan, and S. O’Brien, “Wüstite nanocrystals: Synthesis, structure and superlattice formation,” *Journal of materials research*, vol. 22, no. 7, pp. 1987–1995, 2007.

[118] A. A. Spivakov, C.-R. Lin, C.-J. Jhang, Y.-J. Tsai, and Y.-T. Tseng, “Synthesis and characterization of carbon-coated wustite nanoparticles,” *Materials Letters*, vol. 249, pp. 147–150, 2019.

[119] H. A. Salam, P. Rajiv, M. Kamaraj, P. Jagadeeswaran, S. Gunalan, and R. Sivaraj, “Plants: Green route for nanoparticle synthesis,” *Int Res J Biol Sci*, vol. 1, no. 5, pp. 85–90, 2012.

[120] S. Iravani, “Green synthesis of metal nanoparticles using plants,” *Green Chemistry*, vol. 13, no. 10, pp. 2638–2650, 2011.

[121] O. V. Kharissova, H. R. Dias, B. I. Kharisov, B. O. Pérez, and V. M. J. Pérez, “The greener synthesis of nanoparticles,” *Trends in biotechnology*, vol. 31, no. 4, pp. 240–248, 2013.

[122] H. Muthukumar and M. Matheswaran, “Amaranthus spinosus leaf extract mediated feo nanoparticles: Physicochemical traits, photocatalytic and antioxidant activity,” *ACS Sustainable Chemistry & Engineering*, vol. 3, no. 12, pp. 3149–3156, 2015.

[123] K. Ahmouda, B. Benhaoua, S. E. Laouini, and A. Labbi, “Plant extract frap effect on cation vacancies formation in greenly synthesized wüstite (fexo) nanoparticles: A new contribution,” *Sustainable Chemistry and Pharmacy*, vol. 25, p. 100 563, 2022.

[124] S. F. Situ and A. C. S. Samia, “Highly efficient antibacterial iron oxide@ carbon nanochains from wustite precursor nanoparticles,” *ACS applied materials & interfaces*, vol. 6, no. 22, pp. 20 154–20 163, 2014.

[125] N. Pernicone, F. Ferrero, I. Rossetti, L. Forni, P. Canton, P. Riello, G. Fagherazzi, M. Signoretto, and F. Pinna, “Wustite as a new precursor of industrial ammonia synthesis catalysts,” *Applied Catalysis A: General*, vol. 251, no. 1, pp. 121–129, 2003.

[126] J. Chavez-Galan and R. Almanza, “Solar filters based on iron oxides used as efficient windows for energy savings,” *Solar Energy*, vol. 81, no. 1, pp. 13–19, 2007.

[127] J. Zhang and Y. Zhao, “Effects of defect and pressure on the thermal expansivity of fe x o,” *Physics and chemistry of minerals*, vol. 32, no. 4, pp. 241–247, 2005.

[128] L. Pereira and M. Alves, “Dyes—environmental impact and remediation,” in *Environmental protection strategies for sustainable development*, Springer, 2012, pp. 111–162.

[129] N. Alizadeh, S. Shariati, and N. Besharati, “Adsorption of crystal violet and methylene blue on azolla and fig leaves modified with magnetite iron oxide nanoparticles,” *International Journal of Environmental Research*, vol. 11, no. 2, pp. 197–206, 2017.

[130] H. Lu, J. Wang, M. Stoller, T. Wang, Y. Bao, and H. Hao, “An overview of nanomaterials for water and wastewater treatment,” *Advances in Materials Science and Engineering*, vol. 2016, 2016.

[131] P. Xu, G. M. Zeng, D. L. Huang, C. L. Feng, S. Hu, M. H. Zhao, C. Lai, Z. Wei, C. Huang, G. X. Xie, *et al.*, “Use of iron oxide nanomaterials in wastewater treatment: A review,” *Science of the Total Environment*, vol. 424, pp. 1–10, 2012.

[132] S. M. Ponder, J. G. Darab, and T. E. Mallouk, “Remediation of cr (vi) and pb (ii) aqueous solutions using supported, nanoscale zero-valent iron,” *Environmental Science & Technology*, vol. 34, no. 12, pp. 2564–2569, 2000.

[133] H. Ohshima and K. Furusawa, *Electrical phenomena at interfaces: fundamentals: measurements, and applications*. CRC Press, 1998, vol. 76.

[134] S. M. Vidojkovic and M. P. Rakin, “Surface properties of magnetite in high temperature aqueous electrolyte solutions: A review,” *Advances in colloid and interface science*, vol. 245, pp. 108–129, 2017.

[135] G. A. Parks, “The isoelectric points of solid oxides, solid hydroxides, and aqueous hydroxo complex systems,” *Chemical Reviews*, vol. 65, no. 2, pp. 177–198, 1965.

[136] C. Moreno-Castilla, “Adsorption of organic molecules from aqueous solutions on carbon materials,” *Carbon*, vol. 42, no. 1, pp. 83–94, 2004.

[137] L. Bruch, “Theory of physisorption interactions,” *Surface Science*, vol. 125, no. 1, pp. 194–217, 1983.

[138] K. K. Karukstis, J. P. Litz, M. B. Garber, L. M. Angell, and G. K. Korir, “A spectral approach to determine location and orientation of azo dyes within surfactant aggregates,” *Spectrochimica Acta Part A: Molecular and Biomolecular Spectroscopy*, vol. 75, no. 4, pp. 1354–1361, 2010.

[139] S. Khurshid, Z. Gul, J. Khatoon, M. R. Shah, I. Hamid, I. A. T. Khan, F. Aslam, *et al.*, “Anionic azo dyes removal from water using amine-functionalized cobalt–iron oxide nanoparticles: A comparative time-dependent study and structural optimization towards the removal mechanism,” *RSC Advances*, vol. 10, no. 2, pp. 1021–1041, 2020.

[140] H.-P. Li, Z. Dou, S.-Q. Chen, M. Hu, S. Li, H.-M. Sun, Y. Jiang, and Q.-G. Zhai, “Design of a multifunctional indium–organic framework: Fluorescent sensing of nitro compounds, physical adsorption, and photocatalytic degradation of organic dyes,” *Inorganic chemistry*, vol. 58, no. 16, pp. 11 220–11 230, 2019.

[141] Z. Zhang and J. Kong, “Novel magnetic fe3o4@ c nanoparticles as adsorbents for removal of organic dyes from aqueous solution,” *Journal of hazardous materials*, vol. 193, pp. 325–329, 2011.

[142] S. Agarwal, I. Tyagi, V. K. Gupta, S. Mashhadi, and M. Ghasemi, “Kinetics and thermodynamics of malachite green dye removal from aqueous phase using iron nanoparticles loaded on ash,” *Journal of Molecular Liquids*, vol. 223, pp. 1340–1347, 2016.

[143] F. M. Valadi, A. Ekramipooya, and M. R. Gholami, “Selective separation of congo red from a mixture of anionic and cationic dyes using magnetic-mof: Experimental and dft study,” *Journal of Molecular Liquids*, vol. 318, p. 114 051, 2020.

[144] T. Madrakian, A. Afkhami, H. Mahmood-Kashani, and M. Ahmadi, “Adsorption of some cationic and anionic dyes on magnetite nanoparticles-modified activated carbon from aqueous solutions: Equilibrium and kinetics study,” *Journal of the Iranian Chemical Society*, vol. 10, no. 3, pp. 481–489, 2013.

[145] K. Chamchoy, T. Inprasit, C. Vanichvattanadecha, A. Thiangtrong, P. Anukunwithaya, and P. Pisitsak, “The magnetic properties and dye adsorption of sericin-modified magnetite nanoparticles,” *Journal of Polymers and the Environment*, vol. 29, no. 2, pp. 484–491, 2021.

[146] A. Gogoi, M. Navgire, K. C. Sarma, and P. Gogoi, “Fe3o4-ceo2 metal oxide nanocomposite as a fenton-like heterogeneous catalyst for degradation of catechol,” *Chemical Engineering Journal*, vol. 311, pp. 153–162, 2017.

[147] H. Valdés, V. A. Solar, E. H. Cabrera, A. F. Veloso, and C. A. Zaror, “Control of released volatile organic compounds from industrial facilities using natural and acid-treated mordenites: The role of acidic surface sites on the adsorption mechanism,” *Chemical Engineering Journal*, vol. 244, pp. 117–127, 2014.

[148] S. Ahmed, M. Rasul, R. Brown, and M. Hashib, “Influence of parameters on the heterogeneous photocatalytic degradation of pesticides and phenolic contaminants in wastewater: A short review,” *Journal of environmental management*, vol. 92, no. 3, pp. 311–330, 2011.

[149] U. G. Akpan and B. H. Hameed, “Parameters affecting the photocatalytic degradation of dyes using tio2-based photocatalysts: A review,” *Journal of hazardous materials*, vol. 170, no. 2-3, pp. 520–529, 2009.

[150] I. K. Konstantinou and T. A. Albanis, “Tio2-assisted photocatalytic degradation of azo dyes in aqueous solution: Kinetic and mechanistic investigations: A review,” *Applied Catalysis B: Environmental*, vol. 49, no. 1, pp. 1–14, 2004.

[151] M. Rauf, M. Meetani, and S. Hisaindee, “An overview on the photocatalytic degradation of azo dyes in the presence of tio2 doped with selective transition metals,” *Desalination*, vol. 276, no. 1-3, pp. 13–27, 2011.

[152] X. Luo, S. Zhang, and X. Lin, “New insights on degradation of methylene blue using thermocatalytic reactions catalyzed by low-temperature excitation,” *Journal of hazardous materials*, vol. 260, pp. 112–121, 2013.

[153] I. F. Benzie and J. J. Strain, “The ferric reducing ability of plasma (frap) as a measure of ”antioxidant power”: The frap assay,” *Analytical biochemistry*, vol. 239, no. 1, pp. 70–76, 1996.

[154] C. Kittel, P. McEuen, and P. McEuen, *Introduction to solid state physics*. Wiley New York, 1996, vol. 8.

[155] U. Holzwarth and N. Gibson, “The scherrer equation versus the’debye-scherrer equation’,” *Nature nanotechnology*, vol. 6, no. 9, pp. 534–534, 2011.

[156] G. Williamson and R. Smallman, “Iii. dislocation densities in some annealed and cold-worked metals from measurements on the x-ray debye-scherrer spectrum,” *Philosophical Magazine*, vol. 1, no. 1, pp. 34–46, 1956.

[157] C. Koike, J. Matsuno, and H. Chihara, “Variations in the infrared spectra of wüstite with defects and disorder,” *The Astrophysical Journal*, vol. 845, no. 2, p. 115, 2017.

[158] S. A. Kahani and Z. Yagini, “A comparison between chemical synthesis magnetite nanoparticles and biosynthesis magnetite,” *Bioinorganic Chemistry and Applications*, vol. 2014, 2014.

[159] A. Bouafia and S. E. Laouini, “Green synthesis of iron oxide nanoparticles by aqueous leaves extract of mentha pulegium l.: Effect of ferric chloride concentration on the type of product,” *Materials Letters*, vol. 265, p. 127 364, 2020.

[160] J. Garcıa-Sánchez, M. Solache-Rıos, J. Martınez-Gutiérrez, N. Arteaga-Larios, M. Ojeda-Escamilla, and I. Rodrıguez-Torres, “Modified natural magnetite with al and la ions for the adsorption of fluoride ions from aqueous solutions,” *Journal of Fluorine Chemistry*, vol. 186, pp. 115–124, 2016.

[161] R. A. Smith, “Semiconductors,” *Semiconductors*, 1978.

[162] W. Strehlow and E. L. Cook, “Compilation of energy band gaps in elemental and binary compound semiconductors and insulators,” *Journal of Physical and Chemical Reference Data*, vol. 2, no. 1, pp. 163–200, 1973.

[163] J. Nowotny and W. Weppner, *Non-Stoichiometric Compounds: Surfaces, Grain Boundaries and Structural Defects*. Springer Science & Business Media, 2012, vol. 276.

[164] N. Tara, S. I. Siddiqui, G. Rathi, S. A. Chaudhry, A. M. Asiri, *et al.*, “Nano-engineered adsorbent for the removal of dyes from water: A review,” *Current Analytical Chemistry*, vol. 16, no. 1, pp. 14–40, 2020.

[165] J. He, M. Guo, and R. Long, “Photoinduced localized hole delays nonradiative electron–hole recombination in cesium–lead halide perovskites: A time-domain ab initio analysis,” *The journal of physical chemistry letters*, vol. 9, no. 11, pp. 3021–3028, 2018.

[166] S. K. Lagergren, “About the theory of so-called adsorption of soluble substances,” *Sven. Vetenskapsakad. Handingarl*, vol. 24, pp. 1–39, 1898.

[167] Y.-S. Ho and G. McKay, “Pseudo-second order model for sorption processes,” *Process biochemistry*, vol. 34, no. 5, pp. 451–465, 1999.

[168] H. Yuh-Shan, “Citation review of lagergren kinetic rate equation on adsorption reactions,” *Scientometrics*, vol. 59, no. 1, pp. 171–177, 2004.

[169] Y.-S. Ho, “Review of second-order models for adsorption systems,” *Journal of hazardous materials*, vol. 136, no. 3, pp. 681–689, 2006.

[170] M. A. Salam, “Removal of heavy metal ions from aqueous solutions with multi-walled carbon nanotubes: Kinetic and thermodynamic studies,” *International Journal of Environmental Science and Technology*, vol. 10, no. 4, pp. 677–688, 2013.

[171] G. Boyd, A. Adamson, and L. Myers Jr, “The exchange adsorption of ions from aqueous solutions by organic zeolites. ii. kinetics1,” *Journal of the American Chemical Society*, vol. 69, no. 11, pp. 2836–2848, 1947.

[172] C. Valderrama, X. Gamisans, X. De las Heras, A. Farran, and J. Cortina, “Sorption kinetics of polycyclic aromatic hydrocarbons removal using granular activated carbon: Intraparticle diffusion coefficients,” *Journal of hazardous materials*, vol. 157, no. 2-3, pp. 386–396, 2008.

[173] L. Yu and Y.-M. Luo, “The adsorption mechanism of anionic and cationic dyes by jerusalem artichoke stalk-based mesoporous activated carbon,” *Journal of Environmental Chemical Engineering*, vol. 2, no. 1, pp. 220–229, 2014.

[174] P. K. Dhar, P. Saha, M. K. Hasan, M. K. Amin, and M. R. Haque, “Green synthesis of magnetite nanoparticles using lathyrus sativus peel extract and evaluation of their catalytic activity,” *Cleaner Engineering and Technology*, vol. 3, p. 100 117, 2021.

[175] H. El Ghandoor, H. Zidan, M. M. Khalil, and M. Ismail, “Synthesis and some physical properties of magnetite (fe3o4) nanoparticles,” *Int. J. Electrochem. Sci*, vol. 7, no. 6, pp. 5734–5745, 2012.

[176] D. L. Michelsen, J. A. Gideon, G. P. Griffith, J. E. Pace, and H. L. Kutat, “Removal of soluble mercury from waste water by complexing techniques,” 1975.

[177] M. Alkan, Ö. Demirbaş, and M. Doğan, "Adsorption kinetics and thermodynamics of an anionic dye onto sepiolite," *Microporous and mesoporous materials*, vol. 101, no. 3, pp. 388–396, 2007.

[178] Z. Aksu, A. İ. Tatlı, and Ö. Tunç, "A comparative adsorption/biosorption study of acid blue 161: Effect of temperature on equilibrium and kinetic parameters," *Chemical Engineering Journal*, vol. 142, no. 1, pp. 23–39, 2008.

[179] M. Doğan, H. Abak, and M. Alkan, "Adsorption of methylene blue onto hazelnut shell: Kinetics, mechanism and activation parameters," *Journal of hazardous materials*, vol. 164, no. 1, pp. 172–181, 2009.

[180] J. A. Davis and J. O. Leckie, "Surface ionization and complexation at the oxide/water interface. 3. adsorption of anions," *Journal of Colloid and Interface Science*, vol. 74, no. 1, pp. 32–43, 1980.

[181] M. Singh, M. Goyal, and K. Devlal, "Size and shape effects on the band gap of semiconductor compound nanomaterials," *Journal of Taibah University for Science*, vol. 12, no. 4, pp. 470–475, 2018.

Appendices

Appendix A: code reference 01-074-1880 of wustite

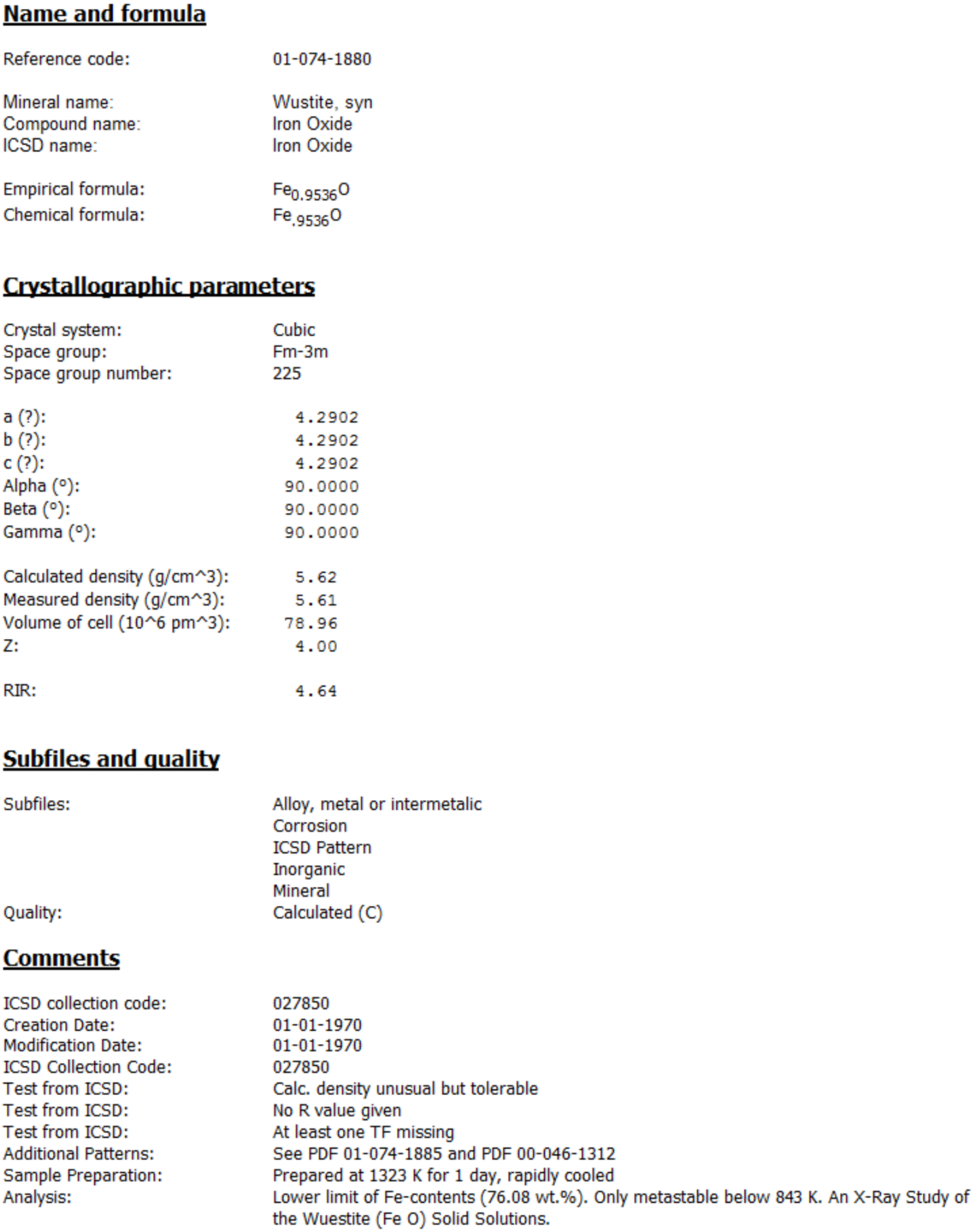

Name and formula

Reference code:	01-074-1880
Mineral name:	Wustite, syn
Compound name:	Iron Oxide
ICSD name:	Iron Oxide
Empirical formula:	$Fe_{0.9536}O$
Chemical formula:	$Fe_{.9536}O$

Crystallographic parameters

Crystal system:	Cubic
Space group:	Fm-3m
Space group number:	225
a (?):	4.2902
b (?):	4.2902
c (?):	4.2902
Alpha (°):	90.0000
Beta (°):	90.0000
Gamma (°):	90.0000
Calculated density (g/cm^3):	5.62
Measured density (g/cm^3):	5.61
Volume of cell (10^6 pm^3):	78.96
Z:	4.00
RIR:	4.64

Subfiles and quality

Subfiles:	Alloy, metal or intermetalic Corrosion ICSD Pattern Inorganic Mineral
Quality:	Calculated (C)

Comments

ICSD collection code:	027850
Creation Date:	01-01-1970
Modification Date:	01-01-1970
ICSD Collection Code:	027850
Test from ICSD:	Calc. density unusual but tolerable
Test from ICSD:	No R value given
Test from ICSD:	At least one TF missing
Additional Patterns:	See PDF 01-074-1885 and PDF 00-046-1312
Sample Preparation:	Prepared at 1323 K for 1 day, rapidly cooled
Analysis:	Lower limit of Fe-contents (76.08 wt.%). Only metastable below 843 K. An X-Ray Study of the Wuestite (Fe O) Solid Solutions.

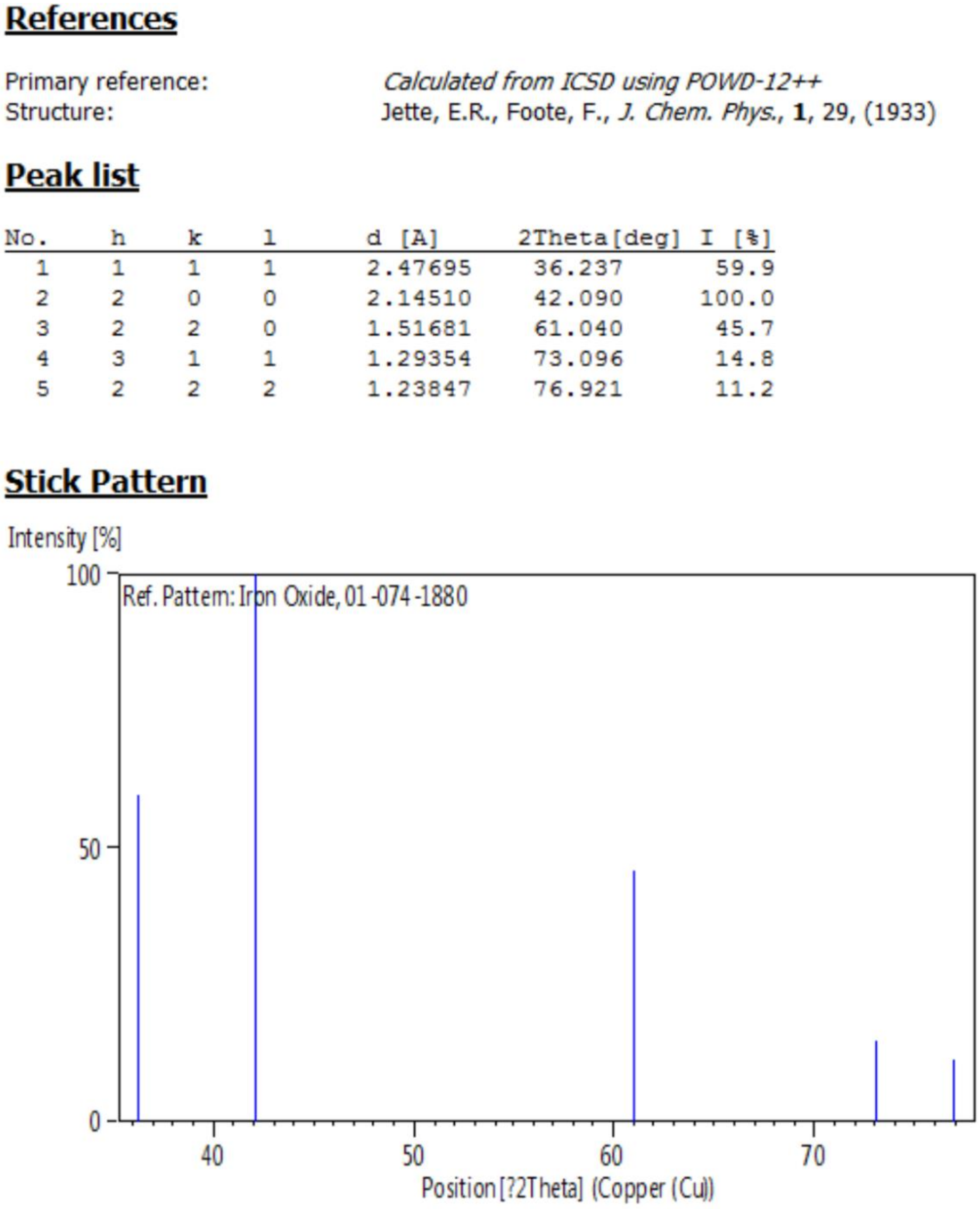

References

Primary reference:	*Calculated from ICSD using POWD-12++*
Structure:	Jette, E.R., Foote, F., *J. Chem. Phys.*, **1**, 29, (1933)

Peak list

No.	h	k	l	d [A]	2Theta[deg]	I [%]
1	1	1	1	2.47695	36.237	59.9
2	2	0	0	2.14510	42.090	100.0
3	2	2	0	1.51681	61.040	45.7
4	3	1	1	1.29354	73.096	14.8
5	2	2	2	1.23847	76.921	11.2

Stick Pattern

Appendix B: code reference 01-076-0956 of magnetite

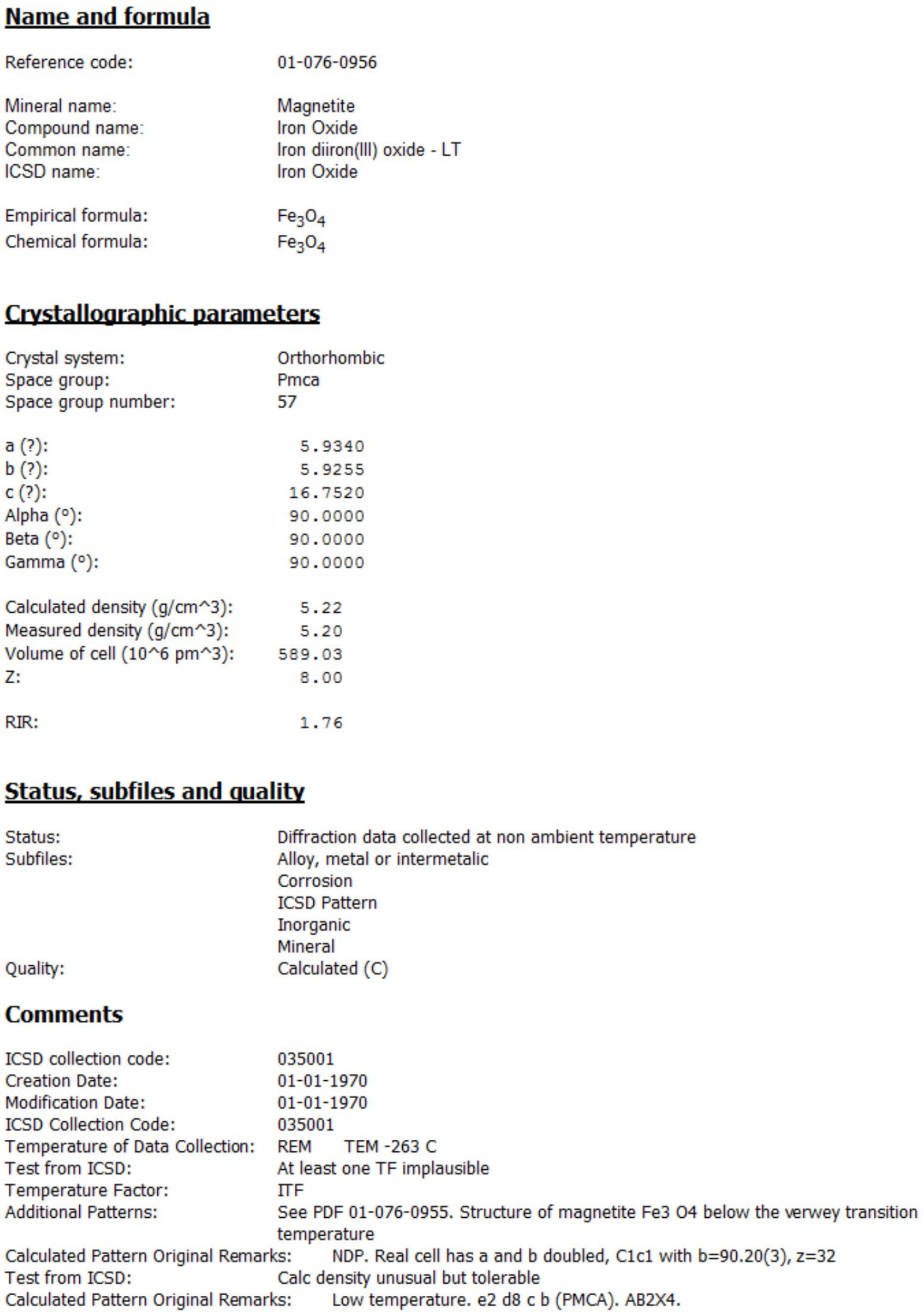

Name and formula

Reference code:	01-076-0956
Mineral name:	Magnetite
Compound name:	Iron Oxide
Common name:	Iron diiron(III) oxide - LT
ICSD name:	Iron Oxide
Empirical formula:	Fe_3O_4
Chemical formula:	Fe_3O_4

Crystallographic parameters

Crystal system:	Orthorhombic
Space group:	Pmca
Space group number:	57
a (?):	5.9340
b (?):	5.9255
c (?):	16.7520
Alpha (°):	90.0000
Beta (°):	90.0000
Gamma (°):	90.0000
Calculated density (g/cm^3):	5.22
Measured density (g/cm^3):	5.20
Volume of cell (10^6 pm^3):	589.03
Z:	8.00
RIR:	1.76

Status, subfiles and quality

Status:	Diffraction data collected at non ambient temperature
Subfiles:	Alloy, metal or intermetalic Corrosion ICSD Pattern Inorganic Mineral
Quality:	Calculated (C)

Comments

ICSD collection code:	035001
Creation Date:	01-01-1970
Modification Date:	01-01-1970
ICSD Collection Code:	035001
Temperature of Data Collection:	REM TEM -263 C
Test from ICSD:	At least one TF implausible
Temperature Factor:	ITF
Additional Patterns:	See PDF 01-076-0955. Structure of magnetite Fe3 O4 below the verwey transition temperature
Calculated Pattern Original Remarks:	NDP. Real cell has a and b doubled, C1c1 with b=90.20(3), z=32
Test from ICSD:	Calc density unusual but tolerable
Calculated Pattern Original Remarks:	Low temperature. e2 d8 c b (PMCA). AB2X4.

References

Primary reference:	*Calculated from ICSD using POWD-12++*, (1997)
Structure:	Iizumi, M., Koetzle, T.F., Shirane, G., Chikazumi, S., Matsui, M., Todo, S., *Acta Crystallogr., Sec. B*, **38**, 2121, (1982)

Peak list

No.	h	k	l	d [A]	2Theta[deg]	I [%]
1	0	0	2	8.37600	10.553	0.1
2	0	1	0	5.92550	14.939	0.1
3	0	1	1	5.58632	15.852	0.1
4	1	0	2	4.83740	18.325	10.9
5	0	0	4	4.18800	21.198	0.1
6	1	1	1	4.06385	21.853	0.1
7	1	1	2	3.74941	23.711	0.1
8	1	0	4	3.42165	26.020	0.1
9	1	1	3	3.35294	26.563	0.1
10	1	1	4	2.96312	30.136	32.4
11	0	2	1	2.91648	30.629	0.3
12	0	2	2	2.79316	32.017	0.1
13	1	2	1	2.61815	34.221	0.4
14	2	1	2	2.52917	35.464	100.0
15	2	0	4	2.42101	37.105	7.7
16	2	1	3	2.39462	37.529	0.4
17	1	1	6	2.32393	38.715	0.1
18	2	1	4	2.23979	40.231	0.1
19	0	2	5	2.21900	40.625	0.1
20	2	2	0	2.09648	43.114	19.1
21	2	0	6	2.03330	44.524	0.1
22	1	0	8	1.97466	45.921	0.1
23	2	2	3	1.96158	46.244	0.1
24	2	1	6	1.92322	47.222	0.6
25	2	2	4	1.87337	48.558	0.1
26	1	3	1	1.86168	48.883	0.1
27	3	1	2	1.82886	49.820	0.1
28	3	0	4	1.78645	51.086	0.1
29	1	3	3	1.77668	51.388	0.1
30	3	1	4	1.71225	53.471	7.8
31	2	2	6	1.67520	54.752	0.1
32	2	1	8	1.64315	55.912	0.1
33	2	3	1	1.63630	56.167	0.2
34	2	3	2	1.61337	57.038	23.3
35	2	3	3	1.57695	58.481	0.3
36	3	1	6	1.55727	59.293	0.1
37	3	2	4	1.53045	60.439	0.1
38	2	1	9	1.52372	60.734	0.1
39	2	2	8	1.48156	62.654	38.5
40	3	2	5	1.47667	62.886	20.4
41	2	0	10	1.45875	63.748	0.1
42	4	1	0	1.43909	64.724	0.1
43	3	0	8	1.43792	64.783	0.1
44	4	1	1	1.43380	64.992	0.1
45	0	4	3	1.43142	65.114	0.1
46	4	1	2	1.41830	65.792	0.7
47	2	2	9	1.39190	67.203	0.1

48	3	3	2	1.37859	67.940	0.1
49	1	0	12	1.35880	69.068	0.1
50	0	3	9	1.35462	69.312	0.1
51	2	4	0	1.32452	71.122	2.2
52	3	1	9	1.32123	71.326	1.2
53	4	2	2	1.31017	72.022	0.1
54	3	2	8	1.29361	73.092	0.1
55	3	3	5	1.28954	73.360	0.1
56	4	1	6	1.27916	74.054	5.7
57	4	2	4	1.26458	75.054	2.3
58	0	4	7	1.25958	75.404	1.2
59	3	1	10	1.24896	76.159	0.1
60	2	1	12	1.23518	77.164	0.1
61	1	4	7	1.23213	77.390	0.1
62	4	0	8	1.21050	79.040	1.7
63	0	4	8	1.20935	79.130	1.6
64	3	3	7	1.20690	79.322	1.0
65	0	3	11	1.20605	79.389	0.9
66	2	4	6	1.19731	80.085	0.1
67	0	5	0	1.18510	81.081	0.1
68	3	1	11	1.18242	81.304	0.1
69	2	3	10	1.17342	82.060	0.4
70	0	4	9	1.15909	83.299	0.1
71	1	5	2	1.15112	84.007	0.1
72	4	3	4	1.14129	84.899	0.1
73	1	5	3	1.13759	85.240	0.1
74	1	5	4	1.11953	86.953	2.6
75	3	4	5	1.11778	87.123	1.4
76	0	4	10	1.10950	87.939	0.1
77	2	5	1	1.09819	89.083	0.1
78	4	1	10	1.09160	89.766	7.5

Stick Pattern

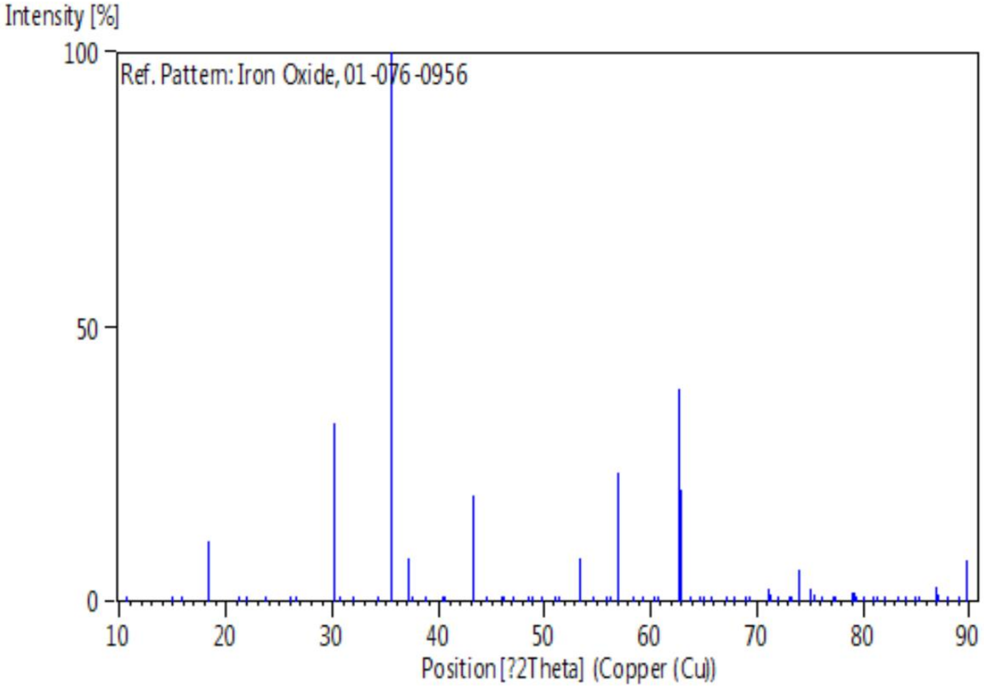

Appendix C: Code reference 01-076-0958 of magnetite

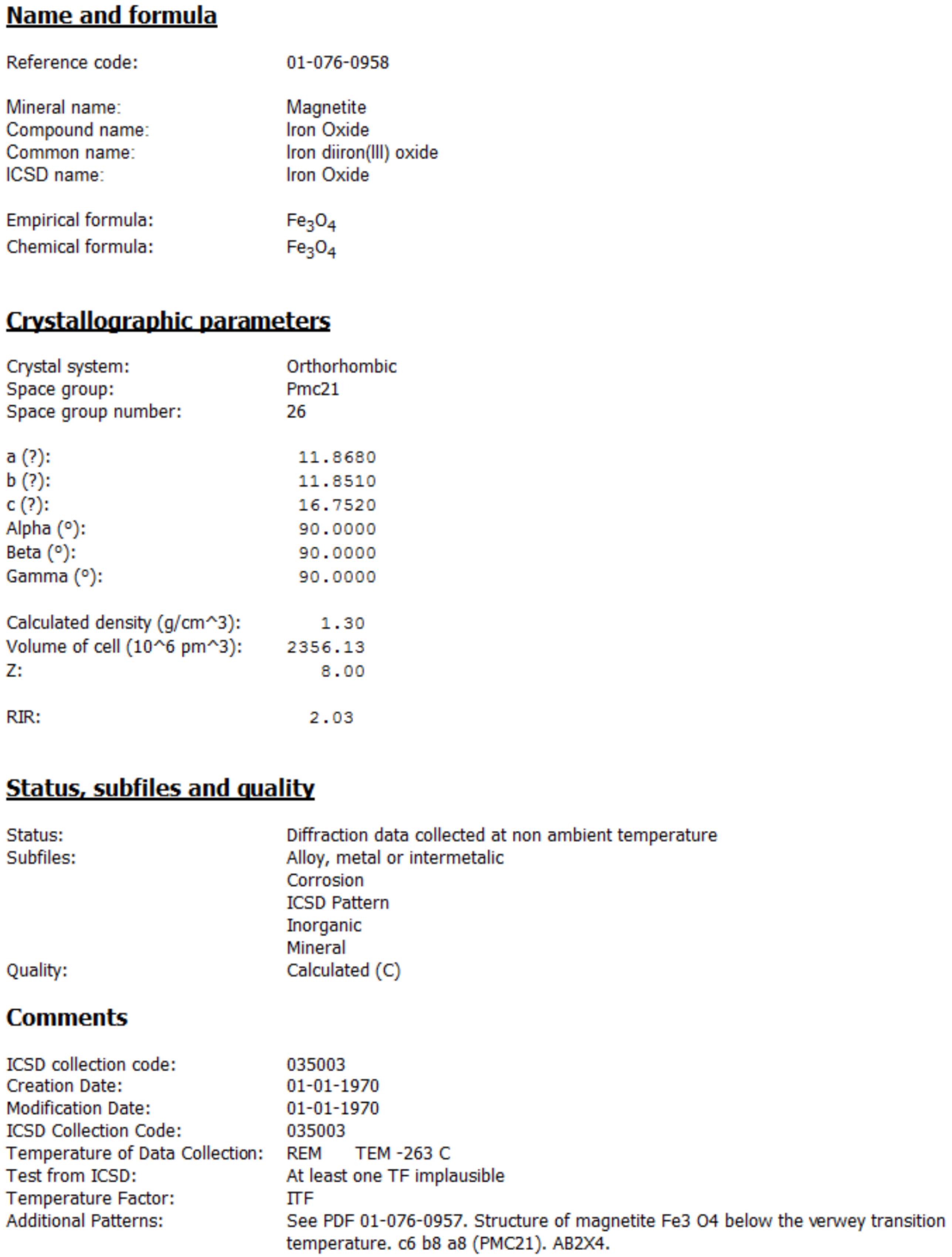

Name and formula

Reference code:	01-076-0958
Mineral name:	Magnetite
Compound name:	Iron Oxide
Common name:	Iron diiron(III) oxide
ICSD name:	Iron Oxide
Empirical formula:	Fe_3O_4
Chemical formula:	Fe_3O_4

Crystallographic parameters

Crystal system:	Orthorhombic
Space group:	Pmc21
Space group number:	26
a (?):	11.8680
b (?):	11.8510
c (?):	16.7520
Alpha (°):	90.0000
Beta (°):	90.0000
Gamma (°):	90.0000
Calculated density (g/cm^3):	1.30
Volume of cell (10^6 pm^3):	2356.13
Z:	8.00
RIR:	2.03

Status, subfiles and quality

Status:	Diffraction data collected at non ambient temperature
Subfiles:	Alloy, metal or intermetalic Corrosion ICSD Pattern Inorganic Mineral
Quality:	Calculated (C)

Comments

ICSD collection code:	035003
Creation Date:	01-01-1970
Modification Date:	01-01-1970
ICSD Collection Code:	035003
Temperature of Data Collection:	REM TEM -263 C
Test from ICSD:	At least one TF implausible
Temperature Factor:	ITF
Additional Patterns:	See PDF 01-076-0957. Structure of magnetite Fe3 O4 below the verwey transition temperature. c6 b8 a8 (PMC21). AB2X4.

References

Primary reference:	*Calculated from ICSD using POWD-12++*, (1997)
Structure:	Iizumi, M., Koetzle, T.F., Shirane, G., Chikazumi, S., Matsui, M., Todo, S., *Acta Crystallogr., Sec. B*, **38**, 2121, (1982)

Peak list

No.	h	k	l	d [A]	2Theta[deg]	I [%]
1	1	0	0	11.85100	7.454	0.1
2	0	1	1	9.67479	9.133	0.1
3	1	1	0	8.38593	10.541	0.3
4	1	1	1	7.49882	11.792	0.1
5	1	0	2	6.84004	12.932	6.8
6	1	1	2	5.92550	14.939	18.5
7	0	2	1	5.58632	15.852	0.1
8	2	1	0	5.30601	16.695	0.1
9	1	2	1	5.05438	17.532	0.4
10	2	0	2	4.83740	18.325	0.1
11	2	1	2	4.48232	19.791	100.0
12	2	2	0	4.19296	21.172	37.3
13	2	2	1	4.06749	21.833	0.5
14	0	3	0	3.95033	22.489	0.1
15	0	3	1	3.84470	23.115	0.3
16	1	3	0	3.74675	23.728	11.2
17	3	0	2	3.57710	24.871	0.4
18	2	0	4	3.42165	26.020	5.2
19	2	2	3	3.35294	26.563	0.1
20	2	3	0	3.28832	27.095	0.1
21	2	3	1	3.22675	27.622	0.3
22	3	2	2	3.06089	29.151	39.0
23	4	0	0	2.96700	30.095	38.7
24	0	4	1	2.91747	30.619	1.1
25	3	0	4	2.87366	31.097	0.2
26	3	2	3	2.83352	31.549	0.4
27	3	1	4	2.79473	31.999	8.6
28	1	0	6	2.71780	32.930	12.4
29	4	2	0	2.65300	33.758	3.3
30	2	4	1	2.61815	34.221	0.1
31	3	2	4	2.58634	34.655	0.1
32	1	4	3	2.55577	35.083	0.1
33	2	0	6	2.52633	35.505	0.1
34	3	3	3	2.49961	35.898	0.1
35	2	1	6	2.47081	36.331	0.3
36	4	0	4	2.42101	37.105	0.1
37	4	2	3	2.39462	37.529	0.1
38	4	1	4	2.37020	37.930	0.1
39	3	2	5	2.34749	38.312	0.1
40	3	3	4	2.32499	38.697	2.5
41	1	5	1	2.30127	39.112	0.1
42	3	0	6	2.28110	39.472	6.1
43	4	2	4	2.24116	40.206	3.3
44	2	5	0	2.20111	40.970	0.1
45	2	5	1	2.18235	41.338	0.4
46	5	2	2	2.13090	42.384	7.5
47	4	4	0	2.09648	43.114	14.7
48	4	4	1	2.08025	43.467	0.9
49	4	3	4	2.06419	43.823	0.2
50	2	5	3	2.04776	44.193	0.2
51	5	1	4	2.03435	44.500	2.7

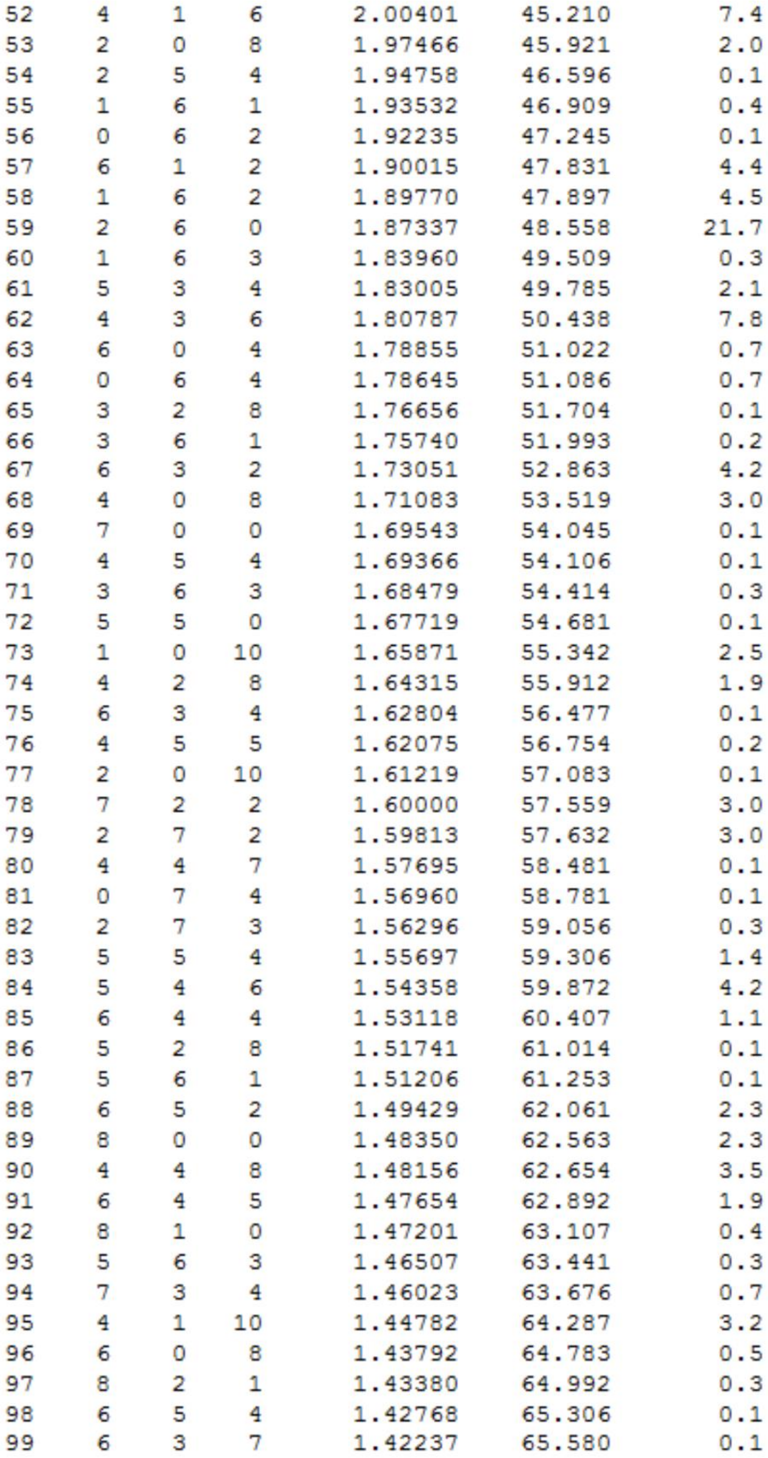

```
52     4     1     6      2.00401     45.210       7.4
53     2     0     8      1.97466     45.921       2.0
54     2     5     4      1.94758     46.596       0.1
55     1     6     1      1.93532     46.909       0.4
56     0     6     2      1.92235     47.245       0.1
57     6     1     2      1.90015     47.831       4.4
58     1     6     2      1.89770     47.897       4.5
59     2     6     0      1.87337     48.558      21.7
60     1     6     3      1.83960     49.509       0.3
61     5     3     4      1.83005     49.785       2.1
62     4     3     6      1.80787     50.438       7.8
63     6     0     4      1.78855     51.022       0.7
64     0     6     4      1.78645     51.086       0.7
65     3     2     8      1.76656     51.704       0.1
66     3     6     1      1.75740     51.993       0.2
67     6     3     2      1.73051     52.863       4.2
68     4     0     8      1.71083     53.519       3.0
69     7     0     0      1.69543     54.045       0.1
70     4     5     4      1.69366     54.106       0.1
71     3     6     3      1.68479     54.414       0.3
72     5     5     0      1.67719     54.681       0.1
73     1     0    10      1.65871     55.342       2.5
74     4     2     8      1.64315     55.912       1.9
75     6     3     4      1.62804     56.477       0.1
76     4     5     5      1.62075     56.754       0.2
77     2     0    10      1.61219     57.083       0.1
78     7     2     2      1.60000     57.559       3.0
79     2     7     2      1.59813     57.632       3.0
80     4     4     7      1.57695     58.481       0.1
81     0     7     4      1.56960     58.781       0.1
82     2     7     3      1.56296     59.056       0.3
83     5     5     4      1.55697     59.306       1.4
84     5     4     6      1.54358     59.872       4.2
85     6     4     4      1.53118     60.407       1.1
86     5     2     8      1.51741     61.014       0.1
87     5     6     1      1.51206     61.253       0.1
88     6     5     2      1.49429     62.061       2.3
89     8     0     0      1.48350     62.563       2.3
90     4     4     8      1.48156     62.654       3.5
91     6     4     5      1.47654     62.892       1.9
92     8     1     0      1.47201     63.107       0.4
93     5     6     3      1.46507     63.441       0.3
94     7     3     4      1.46023     63.676       0.7
95     4     1    10      1.44782     64.287       3.2
96     6     0     8      1.43792     64.783       0.5
97     8     2     1      1.43380     64.992       0.3
98     6     5     4      1.42768     65.306       0.1
99     6     3     7      1.42237     65.580       0.1
```

Stick Pattern

2